

Adherens junctions organize size-selective proteolytic hotspots critical for Notch signalling

Received: 5 October 2021

Accepted: 19 October 2022

Published online: 1 December 2022

 Check for updates

Minsuk Kwak^{1,2,3,4,5,6,18}, Kaden M. Southard^{1,2,18}, Woon Ryoung Kim^{1,2,3,18}, Annie Lin^{1,2,3}, Nam Hyeong Kim^{1,2,3,6,7,8}, Ramu Gopalappa^{4,9}, Hyun Jung Lee^{1,2,3}, Minji An^{4,5}, Seo Hyun Choi^{4,5}, Yunmin Jung^{4,5}, Kunwoo Noh^{4,5}, Justin Farlow², Anastasios Georgakopoulos¹⁰, Nikolaos K. Robakis¹⁰, Min K. Kang¹¹, Matthew L. Kutys¹², Daeha Seo¹³, Hyongbum Henry Kim^{4,5,9,14,15}, Yong Ho Kim^{6,7,8}, Jinwoo Cheon^{4,5,16}, Zev J. Gartner^{2,17} ✉ & Young-wook Jun^{1,2,3,4,5} ✉

Adherens junctions (AJs) create spatially, chemically and mechanically discrete microdomains at cellular interfaces. Here, using a mechanogenetic platform that generates artificial AJs with controlled protein localization, clustering and mechanical loading, we find that AJs also organize proteolytic hotspots for γ -secretase with a spatially regulated substrate selectivity that is critical in the processing of Notch and other transmembrane proteins. Membrane microdomains outside of AJs exclusively organize Notch ligand–receptor engagement (LRE microdomains) to initiate receptor activation. Conversely, membrane microdomains within AJs exclusively serve to coordinate regulated intramembrane proteolysis (RIP microdomains). They do so by concentrating γ -secretase and primed receptors while excluding full-length Notch. AJs induce these functionally distinct microdomains by means of lipid-dependent γ -secretase recruitment and size-dependent protein segregation. By excluding full-length Notch from RIP microdomains, AJs prevent inappropriate enzyme–substrate interactions and suppress spurious Notch activation. Ligand-induced ectodomain shedding eliminates size-dependent segregation, releasing Notch to translocate into AJs for processing by γ -secretase. This mechanism directs radial differentiation of ventricular zone-neural progenitor cells in vivo and more broadly regulates the proteolysis of other large cell-surface receptors such as amyloid precursor protein. These findings suggest an unprecedented role of AJs in creating size-selective spatial switches that choreograph γ -secretase processing of multiple transmembrane proteins regulating development, homeostasis and disease.

Juxtacrine signalling occurs between cells that are in direct physical contact and orchestrates a wide range of cellular processes involved in development, physiology and disease across multicellular organisms^{1,2}. For example, Notch amplifies cellular differences during cell

fate determination and pattern formation by a juxtacrine mechanism. Similarly, neural adhesion and immune receptors are critical in juxtacrine signalling events at neurological^{3–6} and immunological synapses^{7,8}. Unlike diffusible ligands that interact with their receptors

A full list of affiliations appears at the end of the paper. ✉ e-mail: zev.gartner@ucsf.edu; young-wook.jun@ucsf.edu

more uniformly across the cell surface, juxtacrine ligand–receptor pairs localize cell signalling activities to a signal-exchange interface. As two juxtaposed membranes are coupled chemically, spatially and mechanically, the signal-exchange interface undergoes drastic re-organization that constrains the arrangement and activity of both protein and lipid components at the interface^{7–9}. Cells can exploit these interfacial constraints to form specialized membrane compartments that regulate receptor activation, as exemplified by the kinetic segregation and liquid–liquid phase separation of immune receptor signalling^{10–16}. However, many juxtacrine signalling interfaces beyond the immunological synapse can also create these constraints when coupled mechanically through the action of adhesion molecules. The structural and functional consequence of such constraints on signalling pathways outside those regulating immune cell function have not been explored extensively.

In this Article, we investigate specialized interfacial membrane compartments organized by adherens junctions (AJs) that create two physically and biochemically distinct microenvironments for the sequential molecular processing of Notch: one serves as a microdomain for ligand–receptor engagement (LRE microdomain), and the other localizes the proteolytic activity of γ -secretase while effectively selecting only primed receptors for cleavage by size-dependent exclusion (RIP microdomain). By employing mechanogenetics, spatial mutation and clustered regularly interspaced short palindromic repeats (CRISPR)–Cas9 knockout approaches, we examine how this membrane microcompartmentalization choreographs the sequential activation of Notch both in vitro and in vivo. We further test whether these microdomains contribute to proteolytic processing of other large cell surface proteins such as amyloid precursor protein (APP) producing pathogenic amyloid beta (A β).

Notch activation steps occur in distinct membrane microdomains

Notch is a highly conserved mediator of contact-dependent cell–cell communication in metazoans^{17–19}. Tight control of Notch activation is essential for many developmental processes^{20,21}, while dysregulation of Notch activation can cause developmental, neurological and immunological disorders and cancer^{19,22–25}. Accordingly, to enable precise signal regulation, Notch activation occurs through multiple steps that are independently gated by sequential events including (1) ligand–receptor engagement, (2) mechanical unfolding of the negative regulatory region (NRR) and proteolytic ECD shedding (S2 cleavage), and (3) regulated intramembrane proteolysis (S3 cleavage) finally releasing Notch intercellular domain (NICD) (Fig. 1a)^{17,19,26–30}. Several macromolecular interactions are involved in this process, which include Notch ligands, metalloproteases (for example, ADAM 10/17) and γ -secretase.

To interrogate the spatial organization of these molecules, we formed Notch signalling interfaces by culturing cells co-expressing both SNAP–Notch and Halo–DIII. We prevented Notch proteolysis and activation by treating cells with TAPI2 or short hairpin RNA (shRNA) cocktails against ADAM 10/17 (Extended Data Fig. 1b) to explicitly visualize full-length Notch. Enriched fluorescence signals for SNAP–Notch and Halo–DIII were seen at the cellular interface, indicating accumulation of the engaged ligand–receptor pairs at the interface (that is, LRE microdomain) (Fig. 1a,b and Extended Data Fig. 1a). Conversely, we also observed regions within the interfacial membrane depleted of both fluorescence signals, suggesting that certain interfacial microdomains exclude Notch ligands and receptors (Fig. 1a,b). Curiously, the punctuated exclusion patterns matched cell-surface γ -secretase distribution visualized with an anti-presenilin1 (anti-PS1) antibody (Fig. 1a–c and Extended Data Fig. 1a)^{31,32}. This result indicates that Notch ligands/receptors and γ -secretase were compartmentalized into two different membrane microdomains at the signalling interface, potentially preventing their direct interactions.

Considering the requirement of Notch proteolysis by γ -secretase for its activation, we reasoned that cell-surface molecular processing steps for Notch activation (ligand–receptor engagement followed by S2 and then S3 proteolysis) may occur within distinct membrane regions. To test this notion, we investigated how each cleavage step during activation alters the spatial distribution of Notch. To promote accumulation of specific Notch activation intermediates following ADAM 10/17 and γ -secretase cleavage, we induced Notch activation by culturing cells on a Dll4-coated substrate while selectively inhibiting protease activities with TAPI2 (S2 cleavage) or DAPT (S3 cleavage), respectively (Fig. 1d and Extended Data Fig. 1). With S2 inhibition (+TAPI2), we observed Notch exclusion from microdomains enriched with γ -secretase (Extended Data Fig. 1a,b). In contrast, with S2 activation (–TAPI2) and S3 inhibition (+DAPT), we observed strong enrichment of mCherry signal within the γ -secretase-containing microdomain (Fig. 1e). The change in spatial organization indicates that Notch with ECD truncation (NEXT), the product of S2 cleavage, translocated to and was then concentrated within the microdomains. Finally, when γ -secretase activity was rescued by washing out DAPT, the mCherry signal previously enriched at the γ -secretase-containing microdomain disappeared (Extended Data Fig. 1c), presumably corresponding to release of NICD resulting from S3 proteolysis of accumulated Notch within the microdomain (that is, RIP microdomain). Mander's overlap coefficients of mCherry over PS1 also confirmed translocation of Notch from LRE to RIP microdomains, and then NICD release intracellularly (Fig. 1f). These results support the notion that these two membrane microdomains serve distinct and necessary functions in Notch activation. They also raise the possibility that movement of Notch between these domains serves as a

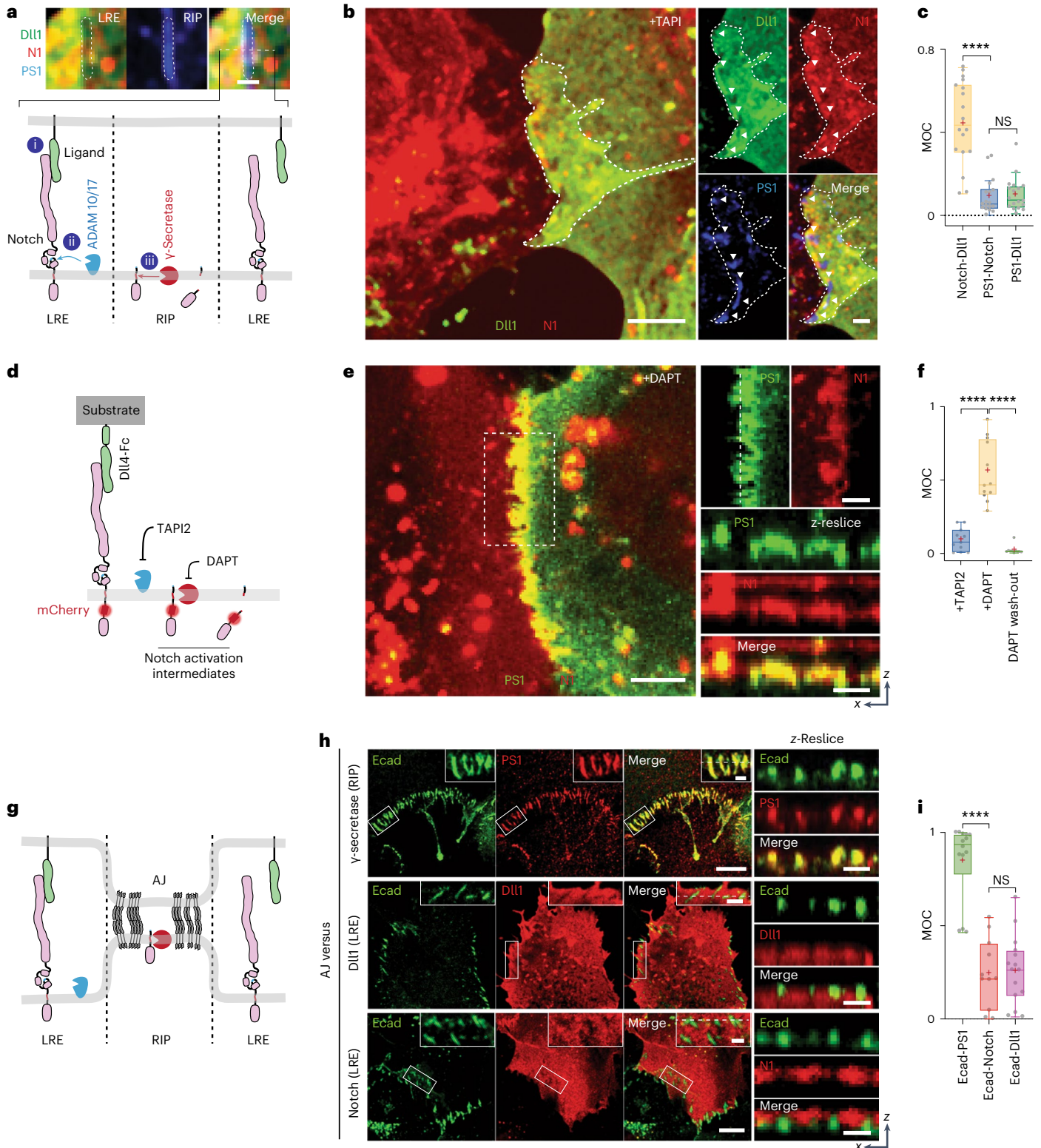
Fig. 1 | Interfacial membrane compartmentalization organized by cadherin-based AJs creates two discrete microenvironments for the sequential molecular processing of Notch. **a**, A schematic showing membrane compartmentalization choreographing the sequential steps in cell-surface activation of Notch. LRE and RIP represent distinct membrane microdomains for Notch receptor–ligand engagement and regulated intramembrane proteolysis, respectively. Top: a representative image showing LRE and RIP microdomains. Scale bar, 2 μ m. **b**, Representative confocal fluorescence images showing DIII, Notch1 (N1) and presenilin1 (PS1) distributions at the interfacial membrane formed between cells co-expressing Notch1 and DIII in the presence of TAPI2. The area with a white dashed line indicates the cellular interface. Left: a maximum intensity projection image of DIII and Notch1 constituting a LRE microdomain. Right: individual fluorescent channel and merged images for DIII, N1 and PS1. **c**, Manders' overlap coefficients (MOCs) of Notch with DIII, PS1 with N1, and PS1 with DIII, respectively. $n = 18$ cells examined for each condition, pooled over three independent experiments. **d**, A schematic of spatial distribution of Notch intermediates during the cell-surface activation pathway. **e**, Representative confocal images of N1 and PS1 within the RIP microdomains from the cells activated by culturing them on a Dll4-Fc immobilized substrate with DAPT.

Left: a maximum intensity projection image of enriched Notch–mCherry signal at RIP microdomains. Top right: magnified individual fluorescence channel images of the boxed region. Right: z-resliced images showing the sections of the cellular interfaces. Scale bar, 4 μ m. **f**, MOCs of Notch1 with PS1 during sequential molecular processing of Notch1. Left to right: $n = 11, 12$ and 10 cells examined over two independent experiments. **g**, A schematic showing AJ-mediated membrane compartmentalization that creates LRE and RIP microdomains. **h**, Representative confocal fluorescence images of RIP (PS1) and LRE (DIII and N1) microdomains relative to AJs. Left: a maximum intensity projection image. Inset shows a magnified image of the boxed area highlighting the membrane microdomains at cellular interfaces. Right: z-resliced images. **i**, MOCs of PS1, DIII and Notch1 localization with E-cadherin. Left to right: $n = 15, 11$ and 14 cells examined over two independent experiments. In **c**, **f** and **i**, for box-and-whisker plots, coloured centre lines and '+' marks indicate median and mean, respectively. The boxes show the 25th to 75th percentiles, and the whiskers extend to the minima and the maxima. **** $P < 0.0001$; NS, non-significant; one-way ordinary ANOVA followed by Tukey's multiple comparison. Scale bars, 2 μ m (**a**), 5 μ m (**b**, left), 2 μ m (**b**, right), 10 μ m (**e**, left), 4 μ m (**e**, right and top right) and 2 μ m (**h**).

spatial switch regulating the interaction between Notch intermediates and γ -secretase, thereby choreographing sequential steps in Notch proteolysis. According to this model, γ -secretase cannot process the full-length Notch before S2 cleavage because enzyme and substrate are concentrated in distinct regions of the cell surface. Following S2 cleavage, translocation of NEXT into the RIP microdomain facilitates a productive Notch- γ -secretase interaction, S3 cleavage predominantly within AJs (but also in endosomes resulting from RIP-microdomain internalization), and then downstream signalling (Extended Data Fig. 1e,f).

AJs organize Notch signalling molecules at cellular interface

To gain insight into molecular features responsible for organizing these distinct membrane microdomains, we imaged γ -secretase distribution across cell membranes. Interestingly, we observed many microdomains with strong γ -secretase signals at cell-cell interface³³, but detected negligible γ -secretase signals at cell membranes distal from cell-cell contact, suggesting that the RIP microdomains were formed at cellular interface exclusively (Extended Data Fig. 2a). As the cell-cell interface



is established and maintained by AJs in many tissues^{34–37}, we reasoned that AJs may organize LRE and RIP microdomains (Fig. 1g). To test this notion, we visualized these microdomains and AJs in cells recombinantly expressing DIII, Notch and E-cadherin. RIP microdomains containing γ -secretase showed nearly identical spatial distribution with AJs (Fig. 1h,i and Extended Data Fig. 2b,c)^{31,32} while LRE microdomains containing DIII and Notch exhibited inverse distribution (Fig. 1h and Extended Data Fig. 2d–g). ADAM10/17 exhibited no preferential distribution relative to AJs (Extended Data Fig. 2h–j). Notch exclusion from AJs was observed in multiple contexts, including endogenous versus recombinant Notch (Extended Data Fig. 2k), different cadherins, cell types and cell polarization (Extended Data Fig. 2l–n), supporting the generality of AJ-mediated microdomain formation. Moreover, we observed Notch translocation into AJs after S2 cleavage, consistent with Notch relocalization from LRE to RIP microdomains (Extended Data Fig. 3a–e). These observations suggest two mechanisms by which AJs might define the compartmentalized microdomains: first, AJs recruit γ -secretase to form RIP microdomains; second, AJs segregate Notch ligands and receptors away from RIP microdomains, limiting ligand–receptor engagement outside of AJs.

AJs recruit γ -secretase through ordered membrane phases

We then investigated how AJs form RIP microdomains. Several reports have suggested possible engagement of AJs with spatially discrete lipid membrane phases^{33,36,38,39}. Similarly, γ -secretase proteolytic activity is closely linked to detergent-resistant membranes^{40–47}. Both of these membrane features preferentially associate with Flotillin-1 (Flot1)^{36,45–48}. We therefore visualized Flot1 localization across the cell membrane. Strong Flot1 and γ -secretase signals were seen at AJs (Fig. 2a,b and Extended Data Fig. 4a,b). To validate the formation of discrete membrane microdomains at AJs, we mapped lipid order in membrane using di-4-ANEPPDHQ^{49,50}. AJs displayed significantly higher general polarization (GP) values than non-junctional membrane regions (Fig. 2c,d), supporting the notion that both AJs and γ -secretase are associated with common and long-lived ordered phases, otherwise known to be short-lived and transient when alone³⁶. Additionally, clustering of E-cadherin, as occurs at AJs, triggers F-actin polymerization at the cytoplasmic leaflet of the membrane³⁰. Given the established interaction between F-actin and membrane constituents like phosphatidylserine that stabilize Flot1-containing lipid microdomains, we reasoned that AJ components may anchor phosphatidylserine leading to formation of the membrane microdomains^{36,51,52}. To test this notion, we performed a coarse-grained molecular dynamics (MD) simulation of the lipid membrane composition of 1,2-dilinoleoyl-*sn*-glycero-3-phosphocholine (DIPC), 1,2-dipalmitoyl-*sn*-glycero-3-phosphocholine (DPPC), *N*-palmitoyl-*O*-phosphocholineserine (PPCS), 1,2-dipalmitoyl-*sn*-glycero-3-phosphoserine (DPPS) and cholesterol (a key component of the discrete lipid membrane phase). We immobilized a portion of DPPS in the inner leaflet to reflect its interaction with AJ components (for example, F-actin). DPPS immobilization resulted in a microdomain having increased transbilayer coupling (Fig. 2e) and decreased lipid diffusion, supporting microdomain stabilization (Fig. 2f,g)⁵¹.

To further confirm the role of discrete membrane phases in recruiting γ -secretase to AJs, we tested whether cholesterol depletion disrupts γ -secretase localization within AJs. As cholesterol depletion also destabilizes native AJs⁴⁷, we instead generated artificial AJs by clustering E-cadherin via mechanogenetics^{34,53,54}, while simultaneously depleting cholesterol with methyl- β -cyclodextrin (M β CD) (Fig. 2h,i). Similar to native AJs, vivid F-actin, Flot1 and PS1 signals were seen at the artificial AJ without M β CD treatment (Fig. 2j and Extended Data Fig. 4c–e), indicating that artificial AJs recapitulate the functional roles of native AJs including γ -secretase recruitment. In contrast, with M β CD, we observed no recruitments of F-actin, Flot1 or PS1 at the artificial AJ (Fig. 2j and Extended Data Fig. 4f,g). Further, artificial clusters of E-cadherin with intracellular domain truncation showed no recruitment of F-actin,

Flot1 or PS1 (Extended Data Fig. 4h–j), suggesting that γ -secretase recruitment into AJs requires ordered lipid assemblies stabilized by molecular interactions and/or activities of the intracellular domain of E-cadherin. From these observations, we concluded that AJs form RIP microdomains by recruiting and stabilizing γ -secretase through a common spatially discrete membrane assembly composed of multiple lipid and protein components (for example, Flot1 and actin). Nevertheless, these results do not preclude the possibility that more direct interactions between γ -secretase and other AJ-associated proteins also contribute to RIP-microdomain formation⁵⁵.

AJs exclude Notch from RIP microdomains due to their large size

We also visualized the spatial distribution of Notch signalling components relative to artificial AJs (Fig. 3a)^{30,56,57}. Artificial AJs are free of membrane juxtaposition. Therefore, the influence of membrane juxtaposition on protein localization can be investigated by comparing receptor distributions in native AJs to artificial AJs. We imaged full-length Notch explicitly by treating cells with TAPI2 and DAPT. Surprisingly, we observed intense Notch localization at artificial AJs (Fig. 3b and Extended Data Fig. 5a–c), which contrasted starkly with the exclusion of Notch from native AJs (Fig. 1g–i). We reasoned that Notch could be excluded from native AJs because the Notch extracellular domain (NECD, 136 nm) is much larger than the intermembrane cleft created by native AJs (20 nm) (refs. 34,58). In contrast, artificial AJs lack a narrow intermembrane cleft, which permits access of Notch to the concentrated γ -secretase within the AJs⁵⁹.

To test this size-dependent model for Notch exclusion from AJ-induced RIP microdomains, we generated a series of U2OS cell lines stably expressing Notch variants with different truncation lengths: a partial deletion of the EGF repeats (N Δ EGF_{1–25}, approximate height 48 nm), complete deletion of the EGF repeats but retention of NRR (N Δ EGF, approximate height 10 nm), and a complete removal of NECD (NEXT, approximate height: 4 nm) (Fig. 3c and Extended Data Fig. 5d,e). To quantify the spatial distribution of each Notch variant relative to the AJ, we measured the average mCherry fluorescence signal inside (I_{IN}) and outside (I_{OUT}) of the AJ and estimated an enrichment ratio (I_{IN}/I_{OUT}) where a value of 1 indicates homogeneous distribution (Extended Data Fig. 5f,g). Consistent with predictions based on size-dependent protein segregation, N Δ EGF_{1–25}, which is taller than the height of the intermembrane AJ cleft, was excluded from AJs ($I_{IN}/I_{OUT} = 0.57$) (Fig. 3d,e). NEXT with an extracellular domain (ECD) smaller than the junctional height was enriched at AJs ($I_{IN}/I_{OUT} = 2.39$) (Fig. 3d,e). N Δ EGF (intermediate height) exhibited a mixed binary localization pattern (exclusion or enrichment) relative to AJs ($I_{IN}/I_{OUT} = 1.32$) (Fig. 3d,e). These results suggest a role for the size-dependent protein segregation as a spatial switch that regulates the distribution of Notch intermediates relative to RIP microdomain.

Notch localization into RIP microdomains is sufficient for its activation regardless of S2 cleavage

We next interrogated the functional consequences of concentrating or excluding a series of Notch variants having different ECDs into AJs (that is, RIP microdomains). We began by culturing cells in the presence of TAPI2 to decouple γ -secretase processing from S2 cleavage, and measured cleaved NICD levels by immunoblotting. Cells expressing N^{FL} or N Δ EGF_{1–25} resulted in no or minimal NICD, respectively (Fig. 3f,g and Extended Data Fig. 5d), whereas cells expressing N Δ EGF produced a significant amount of NICD (Fig. 3f,g). We validated these findings by measuring the dye-labelled extracellular SNAP signal and the intracellular mCherry-tag signals within AJs and within nuclei, respectively, after removing DAPT (Extended Data Fig. 5h–m). Importantly, we observed a dramatic decrease in the mCherry signal within AJs but not outside AJs, confirming that γ -secretase activity was localized within the RIP

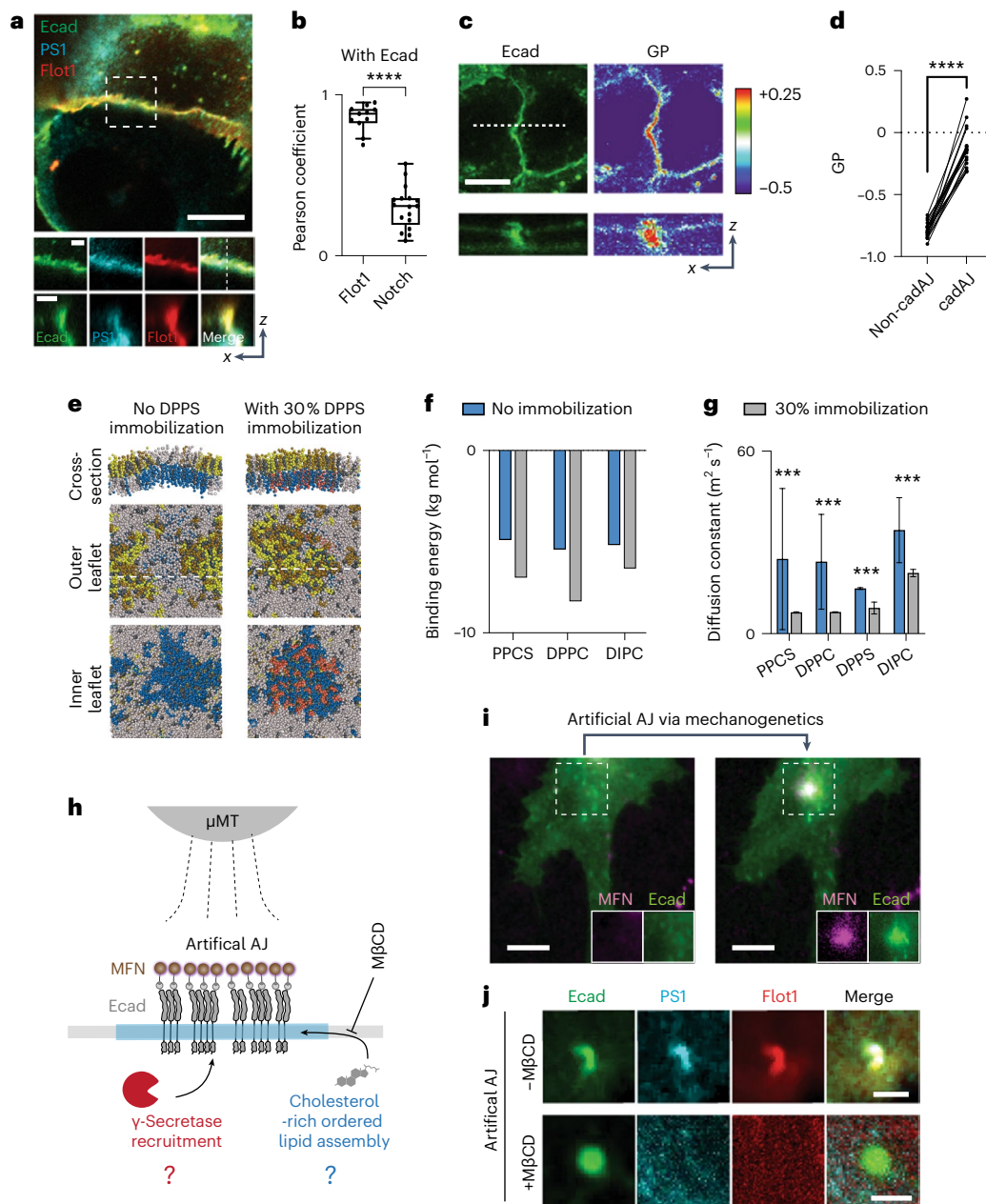


Fig. 2 | AJs form RIP microdomains by recruiting γ -secretase through ordered lipid assemblies. **a**, Representative confocal fluorescence images showing the PS1 and Flot1 distribution relative to native AJs. Left: a maximum intensity projection image of merged channels. Scale bar, 10 μ m. Centre: magnified images of the boxed region. Scale bar, 2 μ m. Right: z-resliced images showing the sections of the AJs. Scale bar, 2 μ m. **b**, MOCs of Flot1 and Notch co-localization with E-cadherin. For the box-and-whisker plot, coloured centre lines and '+' marks indicate median and mean, respectively. The boxes show the 25th to 75th percentiles, and the whiskers extend to the minima and the maxima. Left to right: $n = 11$ and 17 cells examined over two independent experiments. **c**, Di-4-ANEPPDHQ imaging of AJs. Top left: a confocal fluorescence image of Ecad-GFP. Top right: the rainbow RGB GP-value image. Bottom: z-resliced images showing a representative AJ (a white dashed line) of Ecad-GFP (left) and GP values (right). Scale bar, 4 μ m. **d**, A comparison of GP values from AJs and non-AJ regions. $n = 11$ cell-cell interfaces pooled from three independent experiments. **e**, Snapshot images of coarse-grained MD simulation of a lipid bilayer composed of DIPC (grey), DPPC (yellow), PPCS (green), DPPS (blue), immobilized DPPS (pink) and cholesterol (CHOL) (grey). Left and right panels represent the simulation results without and with partial (30%) DPPS

immobilization, respectively. **f,g**, Binding energy (**f**) and diffusion coefficients (**g**) of individual lipid components in a lipid bilayer with or without partial (30%) DPPS immobilization in MD simulation shown in **c**. For diffusion coefficients (**g**), data are the mean \pm s.d. of $n = 3,000$ particles analysed over the MD simulation. **h**, A schematic showing mechanogenetic interrogation of γ -secretase and ordered lipid microassemblies relative to the artificial AJs. Artificial AJs were formed by clustering Ecad-GFP labelled with MFNs by application of an external μ MT. M β CD was used for cholesterol depletion in the cell membrane before artificial AJ formation. **i**, Epifluorescence images showing the formation of an artificial AJ by mechanogenetics. After stimulation by μ MT, vivid MFN and E-cadherin signals at the magnetic focus were seen, indicating formation of AJs. Scale bar, 5 μ m. Images are representative of $n = 4$ independent experiments. **j**, Confocal fluorescence images of E-cadherin, PS1 and Flot1 at the artificial AJ with and without M β CD treatment. After cholesterol depletion, no PS1 recruitment was seen at the AJ, suggesting that γ -secretase recruitment to the AJ requires lipid microdomain formation at the AJ. Scale bar, 2 μ m. Shown are representative from $n = 3$ (-M β CD) and 5 (+M β CD) independent experiments. **** $P < 0.0001$, *** $P < 0.0001$. For **b** and **g**, two-tailed unpaired Student's t -test was performed, and for **d**, two-tailed paired Student's t -test.

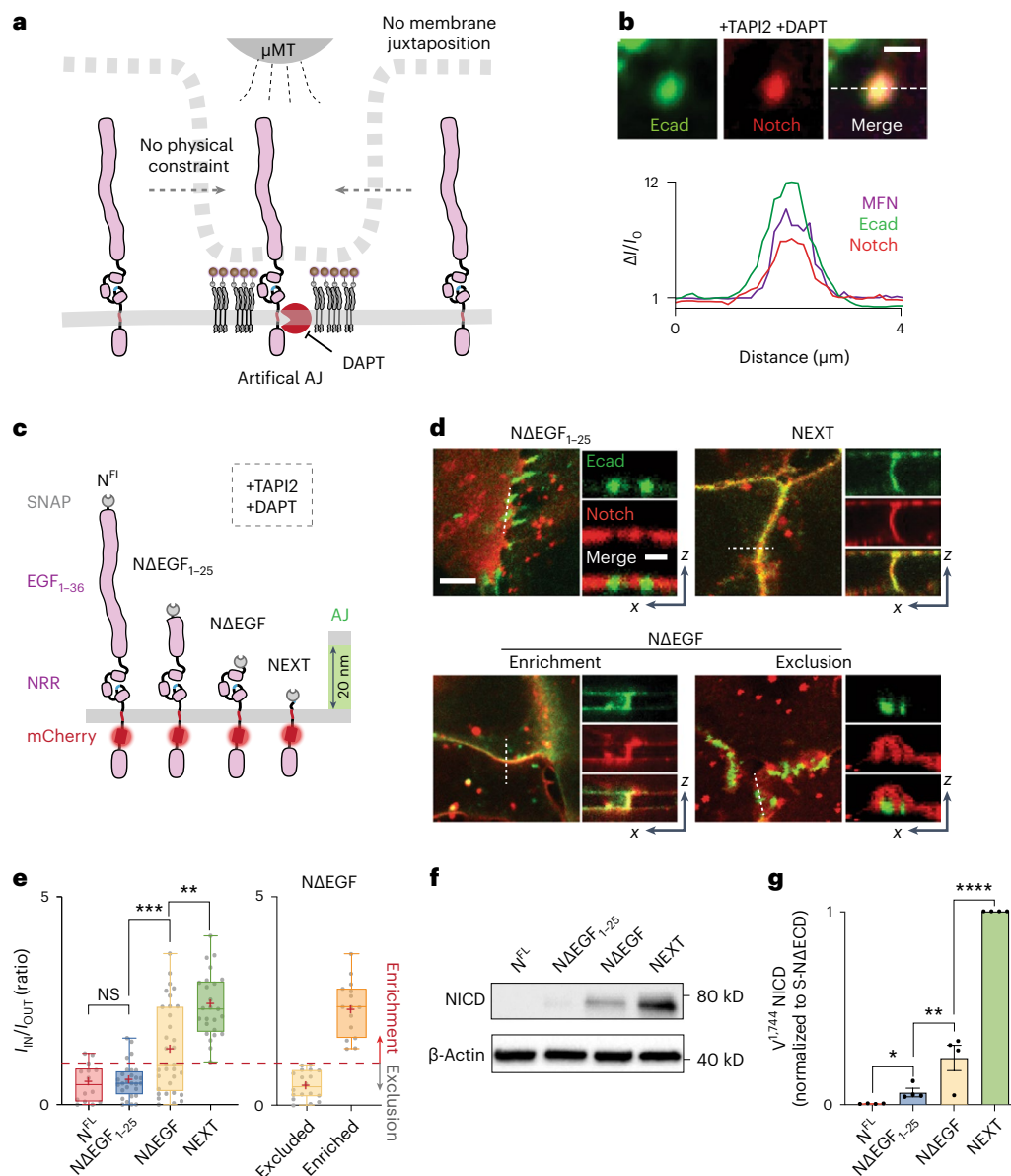


Fig. 3 | Size-dependent protein segregation from AJs exclude Notch receptors from RIP microdomains.

a, A schematic showing mechanogenetic interrogation of Notch distribution relative to the artificial AJ. Cells treated with DAPT to inhibit γ -secretase activity. **b**, Confocal fluorescence images showing E-cadherin and Notch distributions at the artificial AJs after μ MT application. Line profiles of MFN, E-cadherin and Notch signals along a white dashed line. $\Delta I/I_0$ represents a fold change relative to fluorescence intensity before stimulation. Scale bar, 2 μ m. Shown are the representative images from $n = 6$ independent mechanogenetic experiments. **c**, Schematics of Notch variants with different truncation lengths, in comparison with the AJ intermembrane cleft. All cells were treated with TAPI2 and DAPT to prevent any potential proteolysis. **d**, Confocal fluorescence images showing spatial distribution of the Notch variants (red) relative to the AJs (green). Left: maximum intensity projections of confocal z-stacks. Scale bar, 5 μ m. Right: confocal z-resliced images along the white dashed lines in the maximum intensity projection images. Scale bar, 2 μ m. **e**, Quantification of the enrichment

factor (I_{IN}/I_{OUT}) of Notch variants relative to the AJs. A box plot illustrating binary localization of Δ EGF that is defined as either excluded (yellow) or enriched (orange) is shown on the right. Coloured lines and '+' marks indicate median and mean, respectively. The box limits indicate the 25th and 75th percentiles, and the whiskers extend to the minima and the maxima. Left to right: $n = 14, 29, 33, 26, 18$ and 15 cells examined over three independent experiments. $^{**}P = 0.0002$, $^{***}P = 0.0006$. **f, g**, Western blot analyses of cleaved NICD levels in the cells stably expressing N^{FL} , Δ EGF₁₋₂₅, Δ EGF and NEXT. β -Actin levels represent the loading control. A representative image of immunoblotting (**f**), and quantification (**g**) of cleaved NICD levels. The average intensity of each NICD band relative to respective β -actin band was quantified and then normalized to that of NEXT. Data are the mean \pm s.d. of $n = 4$ biological replicates. $^{*}P = 0.011$, $^{**}P = 0.041$. In **e** and **g**, $^{****}P < 0.0001$; NS, non-significant; one-way ANOVA followed by Tukey's multiple comparison test.

microdomains (Extended Data Fig. 5j). Cells expressing NEXT exhibited the highest NICD production, an approximately four fold increase compared with that of Δ EGF (Fig. 3f,g and Extended Data Fig. 5e). NICD production was proportional to the enrichment ratio (I_{IN}/I_{OUT}), suggesting the essential role of size-dependent protein segregation as a spatial switch to direct Notch activation. The substantial NICD

production from the cells expressing Δ EGF indicates that, when localized together, γ -secretase can process Notch, bypassing S2 cleavage. Size-dependent but ligand-independent activation of Notch receptors with an intact S2 site was observed previously in Notch variants and synNotch constructs^{53,54,60–62}, but the mechanism of this activation has been unclear. Our observations support the notion that co-localization

of these Notch variants with γ -secretase is sufficient to trigger S3 proteolysis and signalling. According to this elaborated model, γ -secretase activity on full-length Notch is blocked by maintaining concentrations of Notch and its intermediates below the K_m for γ -secretase owing to their compartmentalization within LRE and RIP microdomains, respectively. Several hypotheses follow from this model that we evaluated experimentally.

First, the model suggests that forced concentration of a Notch variant with an intact S2 site (for example, Δ EGF) in AJs will enhance its processing by γ -secretase. To test this hypothesis, we employed a DNA-mediated crosslinking strategy to enhance Δ EGF enrichment of Δ EGF at the RIP microdomain (that is, AJ)⁶³ (Fig. 4a, Extended Data Fig. 6a–c and Methods). In the presence of TAPI2 and DAPT, we observed increased enrichment of Δ EGF at AJs ($I_{IN}/I_{OUT} = 1.89 \pm 0.91$) after DNA crosslinking (Fig. 4b). When DAPT was removed to rescue γ -secretase activity while maintaining TAPI2, we observed decreased mCherry signal at AJs, indicating efficient S3 cleavage without S2 cleavage (Extended Data Fig. 6d,e). Consistently, in western blots, we observed increased NICD levels from the cells treated with DNA crosslinkers, compared with the untreated control (Fig. 4c). Considering that DNA crosslinking increases the ECD size of Δ EGF, the observed increase in NICD production cannot be explained by the prevailing steric repulsion model of γ -secretase-substrate selectivity⁶².

Second, the model suggests that, for Notch variants bearing optimally positioned N-terminus for γ -secretase processing (for example, NEXT), blocking their access to AJ will inhibit S3 processing. To test this hypothesis, we induced spatial mutation of NEXT by chemically conjugating it with BG-functionalized macromolecules of increasing hydrodynamic size: low-molecular-weight polyethylene glycol (PEG3.4k, 2.5 nm), branched PEG20k (*b*PEG20k, 4.0 nm), linear PEG20k (*l*PEG20k, 8.0 nm), DNA–streptavidin conjugates (DNA-stv, 9.5 nm) and human IgG (hIgG, 12 nm) (Fig. 4d and Extended Data Fig. 6h). Grafting of these macromolecular pendants onto NEXT increases the size of the Notch construct but does not modify the N-terminal amine for hydrogen bonding with nicastrin proposed in the existing model⁶⁴. With DAPT, we observed a size-dependent distribution of NEXT at the AJ, where the larger pendants resulted in a greater decrease in mCherry signal at the AJ (Fig. 4d,e). We then examined the signalling consequences for each spatial mutation of NEXT by detecting nuclear mCherry signal resulting from NICD translocation after S3 cleavage. The PEG3.4k or *b*PEG20k addition did not significantly alter nuclear

mCherry signal of NEXT, compared with cells with no pendant addition (Fig. 4f,g and Extended Data Fig. 6g). Conjugation of *l*PEG20k, DNA-stv and hIgG resulted in a substantial decrease in nuclear mCherry signal to 0.39, 0.37 and 0.27 fractional intensity, respectively. Similarly, immunoblots consistently showed a gradual decrease in the NICD production as a function of macromolecular graft size (Extended Data Fig. 6i). We summarized the NICD production for all Notch variants as a function of the Notch enrichment factor in Fig. 4h, visualizing the spatial dependence of S3 cleavage.

Third, the model predicts that permitting access of full-length Notch, which lacks a suitable N-terminal substrate for γ -secretase, into artificial AJs using mechanogenetics (Fig. 3b) is sufficient to activate the receptor, independent of S2 cleavage. We previously observed pronounced enrichment of full-length Notch at artificial AJs in presence of TAPI2 and DAPT. We repeated identical experiments but removed DAPT to allow γ -secretase activity. We observed no enrichment of mCherry signal at the artificial AJ, presumably owing to S3 cleavage and NICD release (Fig. 4i,j and Extended Data Fig. 6j,k). To confirm that the loss of mCherry signal corresponded to bona fide signalling from Notch, we employed a UAS-Gal4 reporter system that detects Notch activation through expression of a nuclear-localized mCherry^{29,30,65,66}. To a cell recombinantly expressing SNAP-N^{FL}-Gal4 and Halo-Ecad-GFP, we again generated artificial AJs and measured the nuclear mCherry fluorescence every two hours. Note that no source of S2 cleavage (for example, no ligand-immobilized substrate) was added. We observed strong nuclear mCherry signal from the cells with artificial AJs, but no signal from neighbouring cells (Fig. 4k,l and Extended Data Fig. 6l). Together, these three experiments suggest that the new molecular interfaces produced by S2 cleavage are not necessary for S3 cleavage so long as γ -secretase is concentrated sufficiently with its substrate.

AJ-mediated RIP microdomain is indispensable for Notch signalling

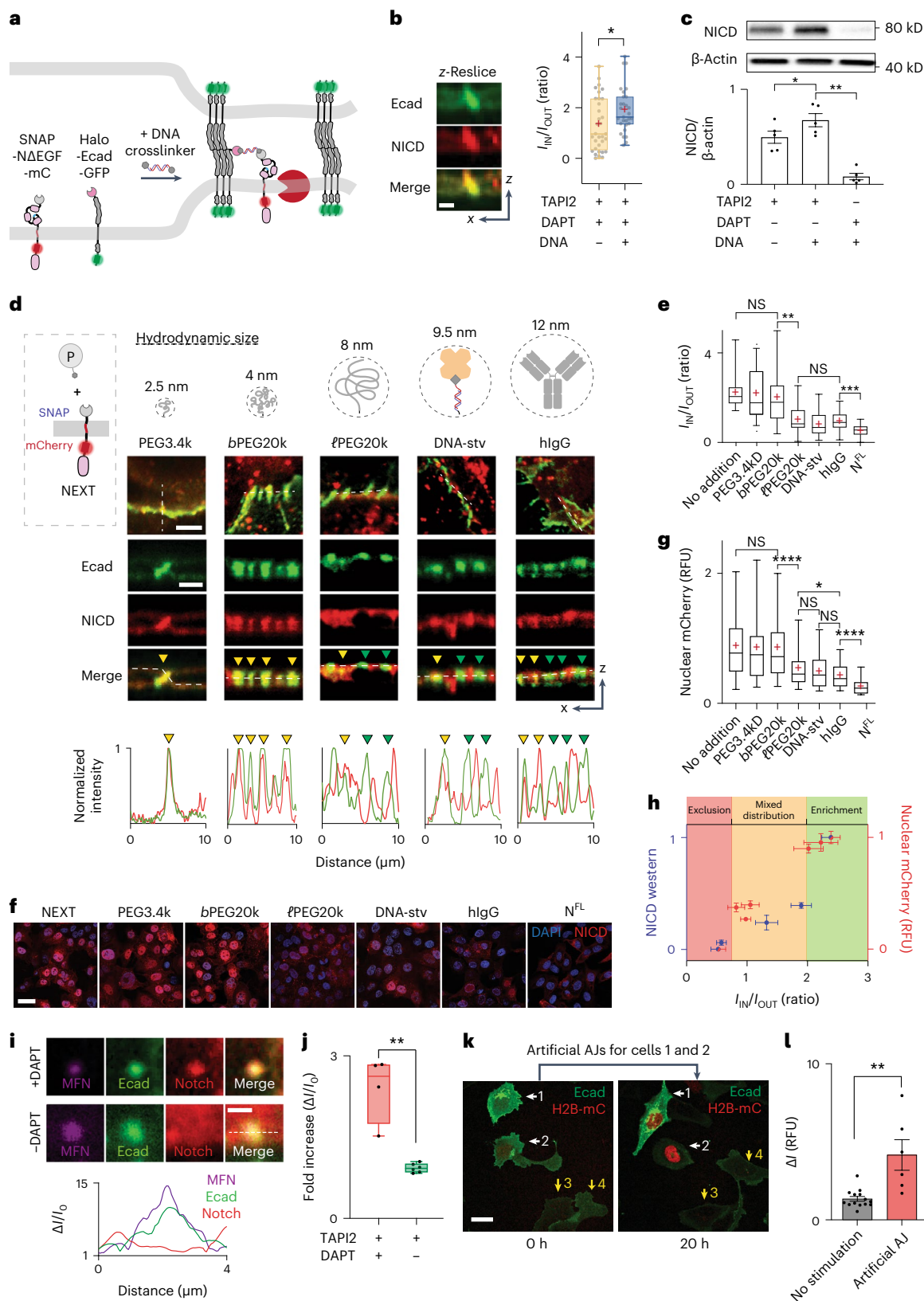
Given the critical role of AJs creating LRE and RIP microdomains, we next interrogated Notch activation in cells lacking AJs. We plated UAS-Gal4 reporter cells expressing SNAP-N^{FL}-Gal4 on a Dll4-coated substrate at low density (to minimize physical contact between cells and hence AJ formation) or high density (to facilitate AJ formation), and then monitored Notch activation of the cells via the reporter signals. While cells with physical contacts with adjacent cells exhibited a robust increase in nuclear mCherry signal, those without cell–cell contact showed no

Fig. 4 | Spatial mutations alter Notch activation, regardless of ligand presentation or S2 cleavage. **a**, The DNA-mediated crosslinking strategy to enhance Δ EGF localization at the AJ. **b**, Confocal z-resliced images showing intense Δ EGF fluorescence (red) enriched at the AJ (green) after the DNA crosslinking. Quantification of enrichment (I_{IN}/I_{OUT}) without ($n = 33$ AJs pooled from three independent experiments) and with ($n = 29$ AJs pooled from three independent experiments) DNA crosslinker treatment ($*P = 0.023$; two-tailed Mann–Whitney–Wilcoxon test). **c**, Western blot analyses of NICD in the Δ EGF cells treated with the DNA crosslinker. Top: a representative blot. Bottom: quantification of cleaved NICD levels. Data are mean \pm s.d. of $n = 5$ biological replicates ($*P = 0.004$, $**P = 0.005$; ordinary one-way ANOVA followed by Tukey's). **d**, Spatial mutation of NEXT via chemical ligation of macromolecular pendants (denoted as P). Confocal images showing size-dependent spatial mutation of NEXT (red) at the AJs (green). The top row shows maximum intensity projection images of the cells treated with the indicated pendants. The middle row shows confocal z-resliced images along the white dashed lines in the maximum intensity projection images. Yellow and green arrowheads, AJs enrichment with and exclusion with Notch, respectively. The bottom row, line profiles quantifying fluorescence signals from NEXT (red) and E-cadherin (green) along the white lines in the z-resliced images. **e**, I_{IN}/I_{OUT} of NEXT with macromolecular pendants. $n = 20$ (no addition), 18 (PEG3.4k), 23 (*b*-PEG20k), 21 (*l*-PEG20k), 16 (DNA-stv), 32 (IgG) and 15 (N^{FL}) cells examined over two independent experiments for **d** and **e** ($**P = 0.002$, $***P = 0.0016$; ordinary one-way ANOVA). **f**, **g**, Confocal fluorescence images (**f**) and quantification (**g**) of nuclear mCherry signal for the

NEXT-expressing cells treated with macromolecular pendants. Cells expressing N^{FL} were used as a negative control. $n = 327$ (no addition), 182 (PEG3.4k), 746 (*b*-PEG20k), 288 (*l*-PEG20k), 179 (DNA-stv), 412 (IgG) and 300 (N^{FL}) cells examined over two independent experiments ($*P = 0.013$, $****P < 0.0001$; ordinary one-way ANOVA). **h**, NICD level of various Notch variants as a function of the enrichment factor. Red and blue dots are spatial mutations of NEXT and Notch variants with different truncation length, respectively. Data are median \pm s.e.m. of $n = 5$ biological replicates (NICD western) and same as **g** for nuclear mCherry. **i**, Representative confocal fluorescence images of cells with an artificial AJ in the presence of TAPI2 and DAPT (top), and TAPI2 only (bottom). Line profiles of MFNs, E-cadherin and Notch signal along the white dashed line. $\Delta I/I_0$: fold change relative to non-junctional membrane signal. **j**, Quantification of mCherry signal at artificial AJs after μ MT application in the presence or absence of DAPT. $n = 4$ (with DAPT) and 6 (TAPI2 only) biologically independent samples ($**P = 0.0003$; two-tailed unpaired Student's *t*-test). In **b**, **e**, **g** and **j**, for box-and-whisker plots, the centre lines and '+' marks indicate median and mean, respectively. The box limits and whiskers indicate the interquartile and the full ranges, respectively. **k**, Representative confocal fluorescence images of the reporter cells with artificial AJs. White and yellow arrows: cells with stimulation and the control cells, respectively. **l**, Statistical analysis of stimulated cells ($n = 6$) versus control cells ($n = 14$). Data are mean \pm s.e.m.; $**P = 0.004$; two-tailed unpaired Student's *t*-test. RFU: Relative fluorescence unit. Scale bars, 3 μ m (**b**), 5 μ m (**d**, top), 3 μ m (**d**, middle), 5 μ m (**f**), 2 μ m (**i**) and 10 μ m (**k**).

increase in signal (Fig. 5a–c and Supplementary Video 1). Re-establishing AJs by plating cells on a substrate coated with Ecad-Fc and Dll4-Fc rescued Notch signalling in solitary cells (Fig. 5a,d and Supplementary Video 2). We further confirmed AJ-dependent Notch activation in cells cultured with varying densities across a Dll4-coated substrate (Fig. 5b). These results support a model wherein AJs are required for

Notch processing at the cell surface and downstream signalling. Critically, E-cadherin seems to function by recruiting γ -secretase but independent of its role in mediating cell–cell contact. To further validate the role of AJs, we knocked out the gene encoding E- and N-cadherin (CDH1/2) in the reporter cell line using CRISPR–Cas9 (Extended Data Fig. 7a–d), then plated the cells at high density on Dll4-Fc-coated plates.



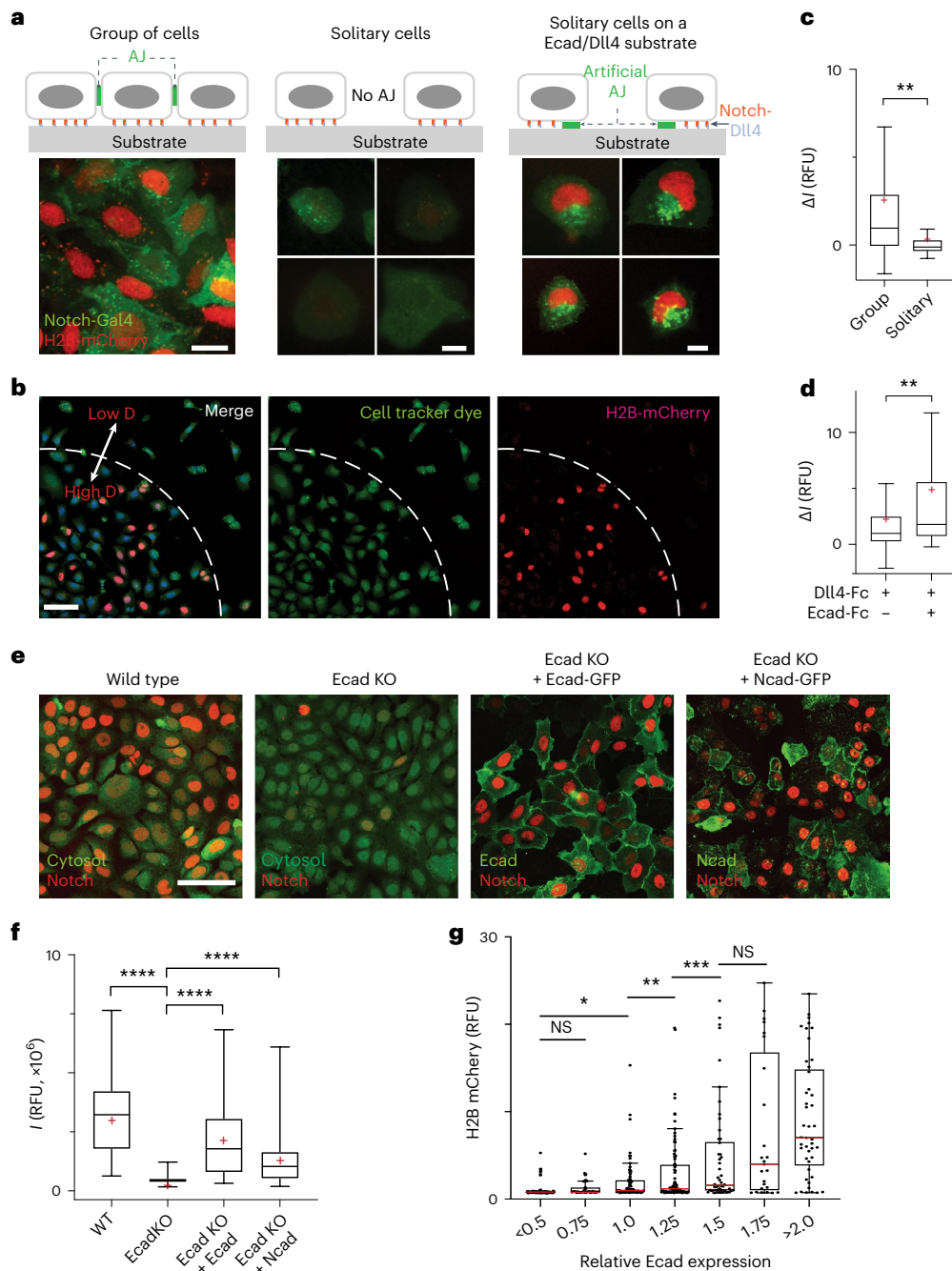


Fig. 5 | The AJ-mediated spatial switch regulates Notch signalling.

a, Representative epifluorescence images showing Notch activation in U2OS SNAP-N^{FL}-Gal4 reporter cell lines in different cellular environments: group of cells on a Dll4-Fc-coated substrate (left), solitary cells with no prior contact on a Dll4-Fc-coated substrate (middle) and solitary cells plated on a Dll4-Fc- and Ecad-Fc-coated substrate (right). Scale bars, 20 μm . **b**, Representative low-magnification epifluorescence image showing both grouped cells and multiple solitary cells. D: Density. Scale bar, 100 μm . **c**, Quantification of Notch activation by measuring H2B-mCherry fluorescence changes in cells within a group ($n = 152$ cells from three independent experiments), solitary cells ($n = 50$ cells from three independent experiments). $**P = 0.0034$ (unpaired two-tailed Student's t -test). **d**, Quantification of Notch activation in solitary cells cultured on a Dll4-Fc-coated substrate and those cultured on a Dll4-Fc- and Ecad-Fc-coated substrate ($n = 27$ cells for both conditions from three independent experiments). $**P = 0.005$ (unpaired two-tailed Student's t -test). **e**, Representative confocal images of H2B-mCherry fluorescence in U2OS SNAP-N^{FL}-Gal4 reporter cells (wt), E-cadherin knockout cells (Ecad-KO), Ecad-KO cells with recombinant E-cadherin transfection (Ecad-KO + Ecad) and Ecad-KO cells with N-cadherin

transfection (Ecad-KO + Ncad). WT and Ecad-KO cells were also stained with CMFDA dye. E-cadherin and N-cadherin were shown for Ecad-KO + Ecad and Ecad-KO + Ncad cells. Scale bar, 100 μm . **f**, Quantification of Notch activation in the WT ($n = 86$), Ecad-KO ($n = 100$), Ecad-KO + Ecad ($n = 52$) and Ecad-KO + Ncad ($n = 80$) cells (all pooled from two independent experiments). $****P < 0.0001$ (ordinary one-way ANOVA followed by Tukey's). In **c**, **d** and **f**, boxes and whiskers indicate the interquartile and full ranges, respectively. Black lines and '+' marks indicate median and mean, respectively. **g**, Comparison of Notch signal activation (measured by mean nuclear H2B-mCherry fluorescence) as a function of E-cadherin expression (measured by membrane GFP fluorescence signal). Each dot represents H2B-mCherry signal of a single cell, and cells are grouped into bins based on their levels of Ecad expression. Left to right: $n = 94, 35, 71, 87, 50, 25$ and 45 cells examined across two independent experiments. $*P = 0.019$, $**P = 0.049$, $***P = 0.036$; NS, non-significant (ordinary one-way ANOVA followed by Tukey's). In the box-and-whisker plot, the red lines indicate median. The boxes and whiskers indicate the 25th to 75th percentiles, and the 10th to 90th percentiles, respectively.

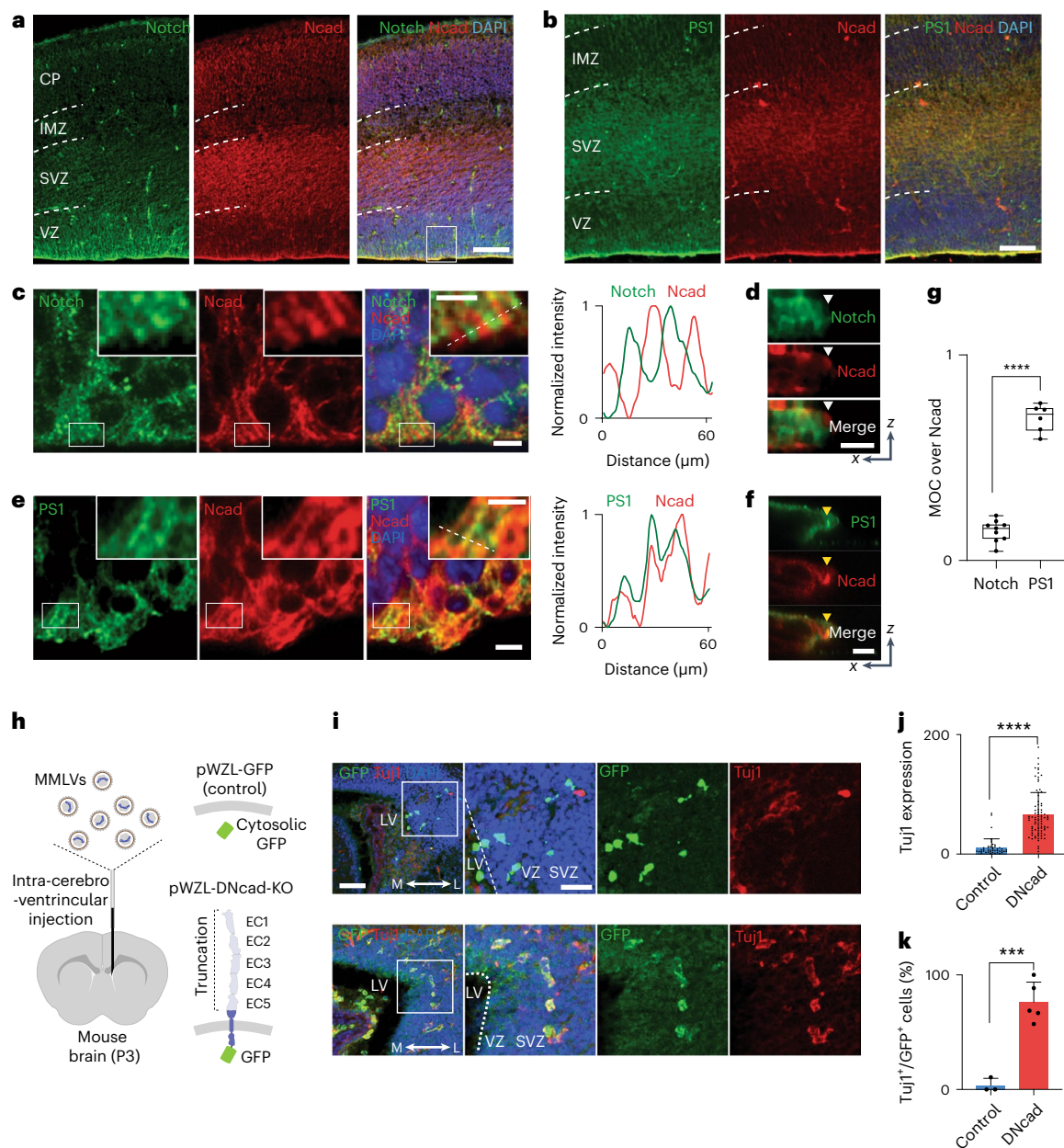


Fig. 6 | The AJ-mediated spatial switch regulates neuronal progenitor cell differentiation in vivo. **a–f**, Immunostaining of the subventricular zone (SVZ) in the lateral ventricle (LV) of the E13.5 mouse brain. Notch (**a**, **c** and **d**) and PS1 (**b**, **e** and **f**) distributions relative to AJs. Representative low (**a** and **b**) and high (**c** and **e**) magnification images. Scale bars, 100 μm and 5 μm , respectively. The boxed area in **c** and **e** is further magnified in the inset. Scale bar, 2.5 μm . Line profile analysis shown in **c** and **e**. Representative confocal z-resliced image showing Notch exclusion (white arrowhead) and PS1 co-localization (yellow arrowhead) with the AJ (**d** and **f**). Scale bar, 3 μm . **g**, Quantitative assessment of Notch and PS1 co-localization with N-cadherin in vivo. Each dot represents MOCs quantifying co-localized Notch (MOC 0.14 ± 0.05 , $n = 9$ cells examined across two independent experiments) or PS1 (MOC 0.69 ± 0.07 , $n = 6$ cells examined across two independent experiments) over selected AJs (**** $P < 0.0001$; two-tailed unpaired Student's *t*-test). In the box-and-whisker plot, the boxes show the 25th to 75th percentiles (with the black bar indicating the mean),

and the whiskers extend to the maxima and minima. **h**, Retroviral infection of developing P3 mice via intracerebroventricular injection using a control vector (EGFP) or using a vector encoding a dominant-negative form of E-cadherin (DN-cad-EGFP). **i**, Immunofluorescent staining images of brain slices of mice retrovirally infected with DN-cad-GFP with control plasmids, respectively. Cells differentiated into post-mitotic neurons can be identified as EGFP⁺/Tuj1⁺, while those which remained as NPCs with plasmid transfection are only EGFP⁺. Data are representative from $n = 3$ (control) and 5 (DN-cad-GFP) independent animals. Scale bar, 50 μm . **j**, Quantification of the expression of Tuj1 per single cells ($n = 43$ cells across three mice and $n = 86$ cells across five mice per control and DN-cad, respectively). Data are mean \pm s.e.m. (**** $P < 0.0001$; two-tailed unpaired Student's *t*-test). **k**, Quantification of the percentage of Tuj1-expressing post-mitotic neurons among all transfected EGFP⁺ cells were quantified. $n = 3$ (control plasmid) and 5 (DN-cad-GFP) animals. Data are mean \pm s.e.m. (*** $P = 0.0005$; two-tailed unpaired Student's *t*-test).

Strikingly, cadherin knockout (cad-KO) resulted in abrogation of Notch activation even in the presence of extensive cell-cell contacts (Fig. 5e,f and Extended Data Fig. 7e–g). Re-introduction of plasmids encoding E-cadherin or N-cadherin into Ecad-KO cells recovered Notch activation

(Fig. 5e,f and Extended Data Fig. 7e–g). Single-cell analysis of the nuclear fluorescence signal revealed a positive correlation with E-cadherin expression in the respective cells, confirming AJ-dependent Notch signalling (Fig. 5g).

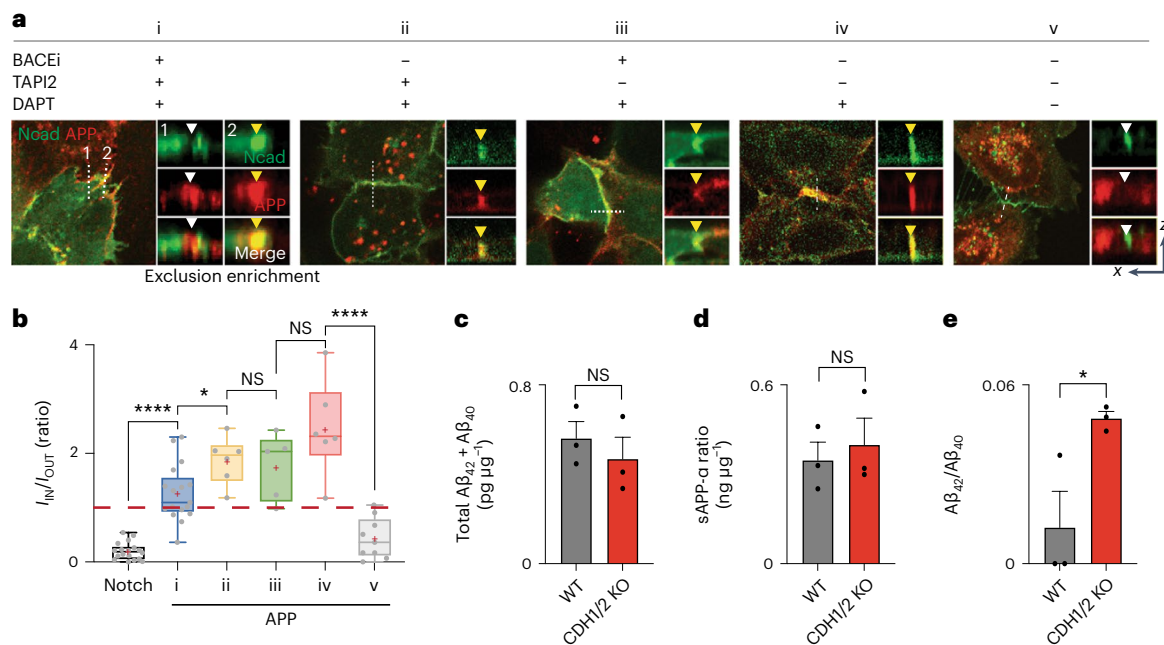


Fig. 7 | The AJ-mediated spatial switch regulates APP signalling. **a**, Confocal fluorescence maximum intensity projection (left) and z-resliced images (right) of U2OS cells co-expressing Ncad-mCherry (green) and APP-EGFP (red) in different combinations of α -, β - and γ -secretase inhibitors. White and yellow arrows indicate APP exclusion from and colocalization with AJs, respectively. Scale bars, 10 μ m (maximum intensity projection) and 3 μ m (inset). **b**, Quantification of the enrichment factor (I_{IN}/I_{OUT}) of APP signal relative to the NAJs. In the box-and-whisker plot, the boxes show the 25th to 75th percentiles, and the

whiskers extend to the maxima and minima. Black lines and '+' marks indicate median and mean, respectively. Left to right: $n = 18, 16, 6, 5, 6$ and 9 biologically independent cells examined across two independent experiments. * $P = 0.049$; **** $P < 0.0001$; NS, non-significant; ordinary one-way ANOVA followed by Tukey's multiple comparison. **c-e**, Total sum of $A\beta_{42}$ and $A\beta_{40}$ (**c**), soluble APP α (**d**) and $A\beta_{42}/A\beta_{40}$ ratio (**e**) measured by ELISA in wild-type cells or CDH1/2 knockout cells. Data are mean \pm s.e.m. of $n = 3$ biological replicates (* $P = 0.041$; NS, non-significant; two-tailed unpaired Student's t -test).

AJ-mediated RIP microdomains regulate NPC differentiation in vivo

Notch signalling is essential for the maintenance of stemness, self-renewal and differentiation of neural progenitor cells (NPCs)^{67,68}. In the mammalian cerebral cortex, Notch signalling orchestrates developmental neurogenesis, where it modulates a balance between tangential proliferative and radial differentiative expansion of the apical ventricular-zone NPCs (VZ-NPCs) to establish a stratified neuronal organization⁶⁹. Interestingly, radial expansion of VZ-NPCs accompanies its differentiation, suggesting that Notch signalling in VZ-NPCs may be coupled with cells' spatial cues. Several reports also emphasize the critical role of apical-endfoot AJs in Notch signalling and in the decision-making process of VZ-NPC development⁷⁰⁻⁷².

Given the essential role of the AJ-mediated microdomain formation for Notch signalling in cell line models, we reasoned that apical-endfoot AJs may also organize proteolytic hotspots for Notch activation. To test this hypothesis, we mapped the spatial distribution of Notch and γ -secretase relative to N-cadherin-based AJs (NAJs) in VZ-NPCs of the developing mouse brain (E13.5) (Fig. 6a-g). Notch and PS1 exhibited exclusion from and enrichment within AJs, respectively, confirming compartmentalization between LRE and RIP microdomains (Fig. 6c-g). We also captured the spatial distribution of the Notch activation intermediate by intra-cerebroventricular injection of DAPT into post-natal mice (P3). Immunostaining showed enhanced Notch signal within AJs, presumably resulting from NEXT accumulation (Extended Data Fig. 8a) as observed in cell lines (Fig. 1d-f and Extended Data Fig. 3b,c). These results support the notion that AJs also drive compartmentalized microdomains and serve as a spatial switch regulating Notch signalling in vivo.

To understand the function of the AJs on VZ-NPC development, we disrupted AJs using dominant-negative cadherin expression, preventing RIP-microdomain formation. We retrovirally transduced VZ-NPCs

in developing mice (P3) using a dominant-negative form of E-cadherin having an ECD truncation (DN-cad)⁷² and a C-terminal GFP tag (Fig. 6h). While mice injected with control retroviruses showed negligible Tuj1-neuronal marker immunostaining, those with retroviruses encoding DN-cad exhibited robust Tuj1 expression, presumably through downregulation of Notch signalling (Fig. 6i-k and Extended Data Fig. 8b,c). These results support that AJ-mediated RIP microdomains modulate NPC maintenance and differentiation via Notch signalling.

Size-dependent spatial dynamics and proteolysis of APPs

To test whether AJs serve as proteolytic hotspots with size-dependent substrate selectivity for other large cell surface proteins, we investigated the processing of APP. APP has a similar topology and proteolytic cleavage sequence to that of Notch. Like Notch, upon activation, APP is processed by two rounds of proteolysis: first α - or β -secretase and then γ -secretase releasing its extracellular and intracellular domains, respectively⁷³⁻⁷⁵. We generated U2OS cells co-expressing APP-GFP and SNAP-N-cadherin and monitored the cell surface spatial distribution of APP intermediates relative to NAJs in the presence of protease inhibitors. Having an intermediate ECD size (80 kD), full-length APP showed binary localization (that is, excluded or enriched) relative to AJs in the presence of inhibitors, similar to the Notch variant with EGF repeat truncation (that is, Δ EGF) (Fig. 7a,b and Extended Data Fig. 9a,b). APP diffused into the NAJs after ECD shedding by α - or β -secretase, and then was processed by γ -secretase within it (Fig. 7a,b and Extended Data Fig. 9a,b).

APP proteolysis by γ -secretase produces more soluble p3 and $A\beta_{40}$ predominately, along with less soluble and pathogenic $A\beta_{42}$ and longer isoforms^{73,74}. Previous reports showed that locally acidic microenvironment (for example, pH 5.5) leads to a gain in the proportion of

pathogenic A β species⁷⁶. Additionally, N-cadherin expression in cells stabilizes an open conformation of PS1 that favours A β ₄₀ production over A β ₄₂ (ref. ⁷⁷). Given our previous observation that loss of AJs leads to a decrease in cell-surface γ -secretase, we hypothesized that APP processing would be biased under these conditions towards A β ₄₂. We tested this hypothesis by measuring APP fragment production in U2OS cell lines recombinantly expressing APP but lacking both E- and N-cadherins (CDH1/2-KO cells) (Extended Data Fig. 7a–d). While no significant changes were observed in total A β (40 + 42) and soluble APP α (sAPP α) (Fig. 7c,d), CDH1/2-KO cells produced higher relative levels of A β ₄₂, compared with cells with endogenous cadherin expression⁵⁵ (Fig. 7e).

Discussion

The Notch ligand–receptor interaction (a binding switch) is converted into intracellular signals only following multiple additional regulatory steps gated by mechanical, proteolytic and spatial events. These include unfolding of NRR domain (a mechanical switch), S2 and S3 cleavage (proteolytic switches) and finally translocation of NICD from the cell membrane to the nucleus (a spatial switch)^{17,19,78}. Our study reveals that Notch integrates an additional spatial switch by AJ-driven interfacial membrane compartmentalization to tightly choreograph the critical and irreversible proteolytic cleavage sequence before NICD release. Previously, it was thought that full-length Notch could interact with γ -secretase interaction at the cell surface^{79,80}, where this proteolytic sequence was regulated by modification of the molecular interface between Notch and nicastrin after S2 cleavage^{62,64}. Our model is not incompatible with a contribution of the nicastrin–Notch chemical interface on γ -secretase activity in that evidence suggests the S2 proteolysis lowers the K_m of the enzyme for Notch. However, it strongly suggests that the AJ-driven membrane compartmentalization is the major regulator of Notch– γ -secretase interaction and signalling, functioning by increasing the concentration of the γ -secretase substrate to the point that it exceeds the K_m and is efficiently processed by the enzyme.

The operating principle of this new spatial switch is closely related to another unique feature of Notch receptor: its unusually tall ECD. The functional residues responsible for ligand binding are located near the N-terminus, which protrudes above the crowded cell surface, where they are poised to engage ligands on neighbouring cells. However, it has also been shown that replacing the EGF-like domain repeats with a smaller ligand binding domain (for example, synNotch) maintains receptor function^{81,82}. Why then does Notch receptor bear such a massive ECD? Our study provides insight into this question, where the large ECD is crucial for its spatial segregation from γ -secretase thereby minimizing non-specific ligand-independent activation. Low-level NICD production was observed even for Notch variants with partial EGF truncation (N Δ EGF_{1–25}) and levels gradually increased upon successive truncations. N Δ EGF_{1–25} has a comparable size to smaller Notch family homologues, including LIN-12/Notch and GLP-1/Notch, suggesting the relevance of a spatial switch across the Notch family and metazoans. Our model also explains previous observations where synNotch with a relatively small ECD exhibited significant ligand-independent activation (10–50% of ligand-induced activation)⁶⁰.

We also show that size-dependent spatial segregation regulates APP cleavage and A β production. It has been previously shown that γ -secretase present in different subcellular compartments cleaves APP into diverse A β isoforms^{73,74,83}. Our study shows that, after the ECD cleavage, AJs potentiate cell surface processing of APPs within the junction, yielding A β ₄₀ predominantly, while removal of AJ produces more A β ₄₂ (ref. ⁸⁴). To establish the relevance of this observation to APP processing will require further investigation in a neuronal system, but our results suggest a potential role of the AJ-mediated APP– γ -secretase compartmentalization in A β pathology, possibly influenced by APOE-dependent intracellular and cerebral cholesterol levels⁸⁵. More importantly, these finding suggest that AJ may represent

proteolytic hotspots with size-dependent substrate selectivity across a more diverse range of cell-surface proteins.

Our study also suggests a critical role of the AJ-mediated membrane compartmentalization in VZ-NPC maintenance and differentiation during development. It has been previously proposed that apical-endfoot AJs promote Notch signalling in NPCs^{70–72}, but the mechanism underlying precise Notch signal regulation was unclear. Our findings suggests that Notch signalling is maintained by creating RIP microdomains within AJs, and disruption of the AJs downregulates Notch signalling and hence promotes NPC differentiation. This result also provides important insights on the molecular mechanism of how environmental spatial and physical changes of cells (that is, VZ-NPC detachment and radial migration) direct cell signalling (that is, Notch signalling) and differentiation, to facilitate spatio-temporally coordinated tissue development. Importantly, coupled delamination (due to AJ disruption) and differentiation (due to Notch inactivation) is not limited to this specific case, but seen in many other developmental processes, including intestinal stem cells^{86–88}, supporting hair cells⁸⁴, pituitary gland stem cells⁸⁹ and epithelial–mesenchymal transition⁹⁰. In these cases, loss of AJs could serve as a self-limiting mechanism for Notch signalling, enforcing proper tissue architecture during differentiation.

The size-dependent segregation of Notch from the RIP microdomain has important analogies to the kinetic segregation model of immune cell activation, where the large CD45 phosphatase is excluded from T-cell receptor (TCR) or FC γ receptor (FC γ R) immunological synaptic clefts^{11,12,91,92}. However, several distinct features of the Notch spatial switch exist. First, unlike the immunological synapse where TCR, FC γ R and CD45 remain constant in size throughout activation, Notch undergoes a dramatic size change during activation, enabling its relocalization and sequential proteolysis. Second, the role of AJs in Notch signalling is not limited to creating a physical barrier, but also plays the critical role of recruiting and concentrating γ -secretase to provide proteolytic hotspots at the cell surface. Finally, the consequences of size-dependent segregation on signalling are reversed compared with the immunological synapse. While spatial segregation of CD45 enables sustained TCR/FC γ R phosphorylation and downstream signalling, Notch segregation from AJs inhibits signal activation. Our result extends the relevance of size-dependent spatial segregation models beyond immune cells^{11,12,91}, supporting the notion that size-dependent protein segregation can serve as a general mechanism for regulating a broad range of receptor signalling at the cell–cell interface. It is also important to note that our model may not be limited to the AJs, but may be extended to other cell–cell junctions that provides an environment for size-dependent protein segregation while effectively concentrating proteases.

Overall, AJ-mediated interfacial membrane compartmentalization sheds light on the mechanism underlying the sequential proteolysis of Notch and APPs. We anticipate further implications of our work in other areas of research such as providing new design principles for synthetic receptors like synNotch, as well as new therapeutic approaches that target Notch and APP signalling by spatial mutation in cancer and neurodegenerative diseases.

Online content

Any methods, additional references, Nature Portfolio reporting summaries, source data, extended data, supplementary information, acknowledgements, peer review information; details of author contributions and competing interests; and statements of data and code availability are available at <https://doi.org/10.1038/s41556-022-01031-6>.

References

1. Manz, B. N. & Groves, J. T. Spatial organization and signal transduction at intercellular junctions. *Nat. Rev. Mol. Cell Biol.* **11**, 342–352 (2010).

2. Chen, C. S., Tan, J. & Tien, J. Mechanotransduction at cell–matrix and cell–cell contacts. *Annu. Rev. Biomed. Eng.* **6**, 275–302 (2004).
3. Südhof, T. C. Synaptic neuroligin complexes: a molecular code for the logic of neural circuits. *Cell* **171**, 745–769 (2017).
4. Südhof, T. C. & Malenka, R. C. Understanding synapses: past, present, and future. *Neuron* **60**, 469–476 (2008).
5. Zeng, M. et al. Reconstituted postsynaptic density as a molecular platform for understanding synapse formation and plasticity. *Cell* **174**, 1172–1187.e16 (2018).
6. Sanes, J. R. & Zipursky, S. L. Synaptic specificity, recognition molecules, and assembly of neural circuits. *Cell* **181**, 536–556 (2020).
7. Narui, Y. & Salaita, K. Membrane tethered Delta activates Notch and reveals a role for spatio-mechanical regulation of the signaling pathway. *Biophys. J.* **105**, 2655–2665 (2013).
8. Schmid, E. M. et al. Size-dependent protein segregation at membrane interfaces. *Nat. Phys.* **12**, 704–711 (2016).
9. Salaita, K. et al. Restriction of receptor movement alters cellular response: physical force sensing by EphA2. *Science* **327**, 1380–1385 (2010).
10. Dustin, M. & Shaw, A. Costimulation: building an immunological synapse. *Science* **283**, 649–650 (1999).
11. Groves, J. T. & Kuriyan, J. Molecular mechanisms in signal transduction at the membrane. *Nat. Struct. Mol. Biol.* **17**, 659–665 (2010).
12. van der Merwe, P. A. & Dushek, O. Mechanisms for T cell receptor triggering. *Nat. Rev. Immunol.* **11**, 47–55 (2010).
13. Belardi, B., Son, S., Felce, J. H., Dustin, M. L. & Fletcher, D. A. Cell–cell interfaces as specialized compartments directing cell function. *Nat. Rev. Mol. Cell Biol.* **21**, 750–764 (2020).
14. Case, L. B., Zhang, X., Ditlev, J. A. & Rosen, M. K. Stoichiometry controls activity of phase-separated clusters of actin signaling proteins. *Science* **363**, 1093–1097 (2019).
15. James, J. R. & Vale, R. D. Biophysical mechanism of T-cell receptor triggering in a reconstituted system. *Nature* **487**, 64–69 (2012).
16. Case, L. B., Ditlev, J. A. & Rosen, M. K. Regulation of transmembrane signaling by phase separation. *Annu. Rev. Biophys.* **48**, 465–494 (2019).
17. Kovall, R. A., Gebelein, B., Sprinzak, D. & Kopan, R. The canonical Notch signaling pathway: structural and biochemical insights into shape, sugar, and force. *Dev. Cell* **41**, 228–241 (2017).
18. Kopan, R. & Ilagan, M. X. G. The canonical Notch signaling pathway: unfolding the activation mechanism. *Cell* **137**, 216–233 (2009).
19. Bray, S. J. Notch signalling in context. *Nat. Rev. Mol. Cell Biol.* **17**, 722–735 (2016).
20. van Es, J. H. et al. Notch/γ-secretase inhibition turns proliferative cells in intestinal crypts and adenomas into goblet cells. *Nature* **435**, 959–963 (2005).
21. Artavanis-Tsakonas, S. & Notch, M. R. R. L. Signaling: cell fate control and signal integration in development. *Science* **284**, 770–776 (1999).
22. Boukhatmi, H., Martins, T., Pillidge, Z., Kamenova, T. & Bray, S. Notch mediates inter-tissue communication to promote tumorigenesis. *Curr. Biol.* **30**, 1809–1820.e4 (2020).
23. South, A. P., Cho, R. J. & Aster, J. C. The double-edged sword of Notch signaling in cancer. *Semin. Cell Dev. Biol.* **23**, 458–464 (2012).
24. Nicolas, M. et al. Notch1 functions as a tumor suppressor in mouse skin. *Nat. Genet.* **33**, 416–421 (2003).
25. Lai, E. C. Notch signaling: control of cell communication and cell fate. *Development* **131**, 965–973 (2004).
26. Haines, N. & Irvine, K. D. Glycosylation regulates Notch signalling. *Nat. Rev. Mol. Cell Biol.* **4**, 786–797 (2003).
27. Stanley, P. & Okajima, T. Roles of glycosylation in Notch signaling. *Curr. Top. Dev. Biol.* **92**, 131–164 (2010).
28. Wang, X. & Ha, T. Defining single molecular forces required to activate integrin and Notch signaling. *Science* **340**, 991–994 (2013).
29. Gordon, W. R. et al. Mechanical allostery: evidence for a force requirement in the proteolytic activation of Notch. *Dev. Cell* **33**, 729–736 (2015).
30. Seo, D. et al. A mechanogenetic toolkit for interrogating cell signaling in space and time. *Cell* **165**, 1507–1518 (2016).
31. Marambaud, P. et al. A presenilin-1/γ-secretase cleavage releases the E-cadherin intracellular domain and regulates disassembly of adherens junctions. *EMBO J.* **21**, 1948–1956 (2002).
32. Georgakopoulos, A. et al. Presenilin-1 forms complexes with the cadherin/catenin cell–cell adhesion system and is recruited to intercellular and synaptic contacts. *Mol. Cell* **4**, 893–902 (1999).
33. Guillaume, E. et al. Flotillin microdomains stabilize cadherins at cell–cell junctions. *J. Cell Sci.* **126**, 5293–5304 (2013).
34. Brasch, J., Harrison, O. J., Honig, B. & Shapiro, L. Thinking outside the cell: how cadherins drive adhesion. *Trends Cell Biol.* **22**, 299–310 (2012).
35. Honig, B. & Shapiro, L. Adhesion protein structure, molecular affinities, and principles of cell–cell recognition. *Cell* **181**, 520–535 (2020).
36. Yap, A. S., Gomez, G. A. & Parton, R. G. Adherens junctions revisualized: organizing cadherins as nanoassemblies. *Dev. Cell* **35**, 12–20 (2015).
37. Faló-Sanjuan, J. & Bray, S. J. Membrane architecture and adherens junctions contribute to strong Notch pathway activation. *Development* **148**, 19 (2021).
38. Taulet, N. et al. N-cadherin/p120 catenin association at cell–cell contacts occurs in cholesterol-rich membrane domains and is required for RhoA activation and myogenesis. *J. Biol. Chem.* **284**, 23137–23145 (2009).
39. Causeret, M., Taulet, N., Comunale, F., Favard, C. & Gauthier-Rouvière, C. N-Cadherin association with lipid rafts regulates its dynamic assembly at cell–cell junctions in C2C12 myoblasts. *Mol. Biol. Cell* **16**, 2168–2180 (2005).
40. Szaruga, M. et al. Alzheimer’s-causing mutations shift Aβ length by destabilizing γ-secretase-Aβn interactions. *Cell* **170**, 443–456.e14 (2017).
41. Lee, S.-J. et al. A detergent-insoluble membrane compartment contains Aβ in vivo. *Nat. Med.* **4**, 730–734 (1998).
42. Vetrivel, K. S. et al. Spatial segregation of γ-secretase and substrates in distinct membrane domains. *J. Biol. Chem.* **280**, 25892–25900 (2005).
43. Chow, V. W., Mattson, M. P., Wong, P. C. & Gleichmann, M. An overview of APP processing enzymes and products. *Neuromolecular Med.* **12**, 1–12 (2009).
44. Ehehalt, R., Keller, P., Haass, C., Thiele, C. & Simons, K. Amyloidogenic processing of the Alzheimer β-amyloid precursor protein depends on lipid rafts. *J. Cell Biol.* **160**, 113–123 (2003).
45. Wahrle, S. et al. Cholesterol-dependent γ-secretase activity in bioactive cholesterol-rich membrane microdomains. *Neurobiol. Dis.* **9**, 11–23 (2002).
46. Vetrivel, K. S. et al. Association of γ-secretase with lipid rafts in post-Golgi and endosome membranes. *J. Biol. Chem.* **279**, 44945–44954 (2004).
47. Urano, Y. et al. Association of active γ-secretase complex with lipid rafts. *J. Lipid Res.* **46**, 904–912 (2005).
48. Galbiati, F., Razani, B. & Lisanti, M. P. Emerging themes in lipid rafts and caveolae. *Cell* **106**, 403–411 (2001).
49. Owen, D. M., Rentero, C., Magenau, A., Abu-Siniyeh, A. & Gaus, K. Quantitative imaging of membrane lipid order in cells and organisms. *Nat. Protoc.* **7**, 24–35 (2012).

50. Komura, N. et al. Raft-based interactions of gangliosides with a GPI-anchored receptor. *Nat. Chem. Biol.* **12**, 402–410 (2016).
51. Raghupathy, R. et al. Transbilayer lipid interactions mediate nanoclustering of lipid-anchored proteins. *Cell* **161**, 581–594 (2015).
52. Kusumi, A. et al. Paradigm shift of the plasma membrane concept from the two-dimensional continuum fluid to the partitioned fluid: high-speed single-molecule tracking of membrane molecules. *Annu. Rev. Biophys. Biomol. Struct.* **34**, 351–378 (2005).
53. Struhl, G. & Adachi, A. Requirements for presenilin-dependent cleavage of Notch and other transmembrane proteins. *Mol. Cell* **6**, 625–636 (2000).
54. Palmer, W. H. & Deng, W.-M. Ligand-independent mechanisms of Notch activity. *Trends Cell Biol.* **25**, 697–707 (2015).
55. Kouchi, Z. et al. p120 catenin recruits cadherins to γ -secretase and inhibits production of A β peptide. *J. Biol. Chem.* **284**, 1954–1961 (2009).
56. Kim, J., Jeong, H., Southard, K. M., Jun, Y. & Cheon, J. Magnetic nanotweezers for interrogating biological processes in space and time. *Acc. Chem. Res.* **51**, 839–849 (2018).
57. Kwak, M. et al. Small, clickable, and monovalent magnetofluorescent nanoparticles enable mechanogenetic regulation of receptors in a crowded live-cell microenvironment. *Nano Lett.* **19**, 3761–3769 (2019).
58. Harrison, O. J. et al. The extracellular architecture of adherens junctions revealed by crystal structures of type I cadherins. *Structure* **19**, 244–256 (2011).
59. Polacheck, W. J. et al. A non-canonical Notch complex regulates adherens junctions and vascular barrier function. *Nature* **552**, 258–262 (2017).
60. Yang, Z., Yu, Z., Cai, Y., Du, R. & Cai, L. Engineering of an enhanced synthetic Notch receptor by reducing ligand-independent activation. *Commun. Biol.* **3**, 1–7 (2020).
61. Mumm, J. S. et al. A ligand-induced extracellular cleavage regulates γ -secretase-like proteolytic activation of Notch1. *Mol. Cell* **5**, 197–206 (2000).
62. Bolduc, D. M., Montagna, D. R., Gu, Y., Selkoe, D. J. & Wolfe, M. S. Nicastrin functions to sterically hinder γ -secretase–substrate interactions driven by substrate transmembrane domain. *Proc. Natl Acad. Sci. USA* **113**, E509–E518 (2016).
63. Liang, S. I. et al. Phosphorylated EGFR dimers are not sufficient to activate Ras. *Cell Rep.* **22**, 2593–2600 (2018).
64. Shah, S. et al. Nicastrin functions as a γ -secretase-substrate receptor. *Cell* **122**, 435–447 (2005).
65. Sprinzak, D. et al. *Cis*-interactions between Notch and Delta generate mutually exclusive signalling states. *Nature* **465**, 86–90 (2010).
66. Nandagopal, N. et al. Dynamic ligand discrimination in the Notch signaling pathway. *Cell* **172**, 869–880.e19 (2018).
67. Ables, J. L., Breunig, J. J., Eisch, A. J. & Rakic, P. Not(ch) just development: Notch signalling in the adult brain. *Nat. Rev. Neurosci.* **12**, 269–283 (2011).
68. Louvi, A. & Artavanis-Tsakonas, S. Notch signalling in vertebrate neural development. *Nat. Rev. Neurosci.* **7**, 93–102 (2006).
69. Franco, S. J. & Müller, U. Shaping our minds: stem and progenitor cell diversity in the mammalian neocortex. *Neuron* **77**, 19–34 (2013).
70. Das, R. M. & Storey, K. G. Apical abscission alters cell polarity and dismantles the primary cilium during neurogenesis. *Science* **343**, 200–204 (2014).
71. Fujita, I. et al. Endfoot regeneration restricts radial glial state and prevents translocation into the outer subventricular zone in early mammalian brain development. *Nat. Cell Biol.* **22**, 26–37 (2019).
72. Hatakeyama, J. et al. Cadherin-based adhesions in the apical endfoot are required for active Notch signaling to control neurogenesis in vertebrates. *Development* **141**, 1671–1682 (2014).
73. de Strooper, B. & Karran, E. The cellular phase of Alzheimer’s disease. *Cell* **164**, 603–615 (2016).
74. Selkoe, D. J. & Hardy, J. The amyloid hypothesis of Alzheimer’s disease at 25 years. *EMBO Mol. Med.* **8**, 595–608 (2016).
75. O’Brien, R. J. & Wong, P. C. Amyloid precursor protein processing and Alzheimer’s disease. *Annu. Rev. Neurosci.* **34**, 185–204 (2011).
76. Quintero-Monzon, O. et al. Dissociation between the processivity and total activity of γ -secretase: implications for the mechanism of Alzheimer’s disease-causing presenilin mutations. *Biochemistry* **50**, 9023–9035 (2011).
77. Uemura, K. et al. N-cadherin-based adhesion enhances A β release and decreases A β 42/40 ratio. *J. Neurochem.* **108**, 350–360 (2009).
78. Bray, S. J. Notch signalling: a simple pathway becomes complex. *Nat. Rev. Mol. Cell Biol.* **7**, 678–689 (2006).
79. J, R. W. et al. Evidence for a physical interaction between presenilin and Notch. *Proc. Natl Acad. Sci. USA* **96**, 3263–3268 (1999).
80. Ray, W. J. et al. Cell surface presenilin-1 participates in the γ -secretase-like proteolysis of Notch. *J. Biol. Chem.* **274**, 36801–36807 (1999).
81. Morsut, L. et al. Engineering customized cell sensing and response behaviors using synthetic Notch receptors. *Cell* **164**, 780–791 (2016).
82. Roybal, K. T. et al. Precision tumor recognition by T cells with combinatorial antigen-sensing circuits. *Cell* **164**, 770–779 (2016).
83. Yang, G. et al. Structural basis of Notch recognition by human γ -secretase. *Nature* **565**, 192–197 (2018).
84. Collado, M. S. et al. The postnatal accumulation of junctional E-cadherin is inversely correlated with the capacity for supporting cells to convert directly into sensory hair cells in mammalian balance organs. *J. Neurosci.* **31**, 11855–11866 (2011).
85. Hao, W. et al. Regulation of beta-amyloid production in neurons by astrocyte-derived cholesterol. *Proc. Natl Acad. Sci. USA* **118**, e2102191118 (2021).
86. Maeda, K., Takemura, M., Umemori, M. & Adachi-Yamada, T. E-cadherin prolongs the moment for interaction between intestinal stem cell and its progenitor cell to ensure Notch signaling in adult *Drosophila* midgut. *Genes Cells* **13**, 1219–1227 (2008).
87. Soh, B. S. et al. N-cadherin prevents the premature differentiation of anterior heart field progenitors in the pharyngeal mesodermal microenvironment. *Cell Res.* **24**, 1420–1432 (2014).
88. Kwon, C. et al. A regulatory pathway involving Notch1/ β -catenin/Is1 determines cardiac progenitor cell fate. *Nat. Cell Biol.* **11**, 951–957 (2009).
89. Yoshida, K., Murata, M., Yamaguchi, T., Matsuzaki, K. & Okazaki, K. Reversible human TGF- β signal shifting between tumor suppression and fibro-carcinogenesis: implications of Smad phospho-isoforms for hepatic epithelial-mesenchymal transitions. *J. Clin. Med.* **5**, 7 (2016).
90. Arefin, B., Parvin, F., Bahrampour, S., Stadler, C. B. & Thor, S. *Drosophila* neuroblast selection is gated by Notch, Snail, SoxB, and EMT gene interplay. *Cell Rep.* **29**, 3636–3651.e3 (2019).
91. Dustin, M. L. & Groves, J. T. Receptor signaling clusters in the immune synapse. *Annu. Rev. Biophys.* **41**, 543–556 (2012).
92. Bakalar, M. H. et al. Size-dependent segregation controls macrophage phagocytosis of antibody-opsonized targets. *Cell* **174**, 131–142.e13 (2018).

Publisher's note Springer Nature remains neutral with regard to jurisdictional claims in published maps and institutional affiliations.

Springer Nature or its licensor (e.g. a society or other partner) holds exclusive rights to this article under a publishing agreement with

the author(s) or other rightsholder(s); author self-archiving of the accepted manuscript version of this article is solely governed by the terms of such publishing agreement and applicable law.

© The Author(s), under exclusive licence to Springer Nature Limited 2022

¹Department of Otolaryngology, University of California, San Francisco, CA, USA. ²Department of Pharmaceutical Chemistry, University of California, San Francisco, CA, USA. ³Helen Diller Family Cancer Comprehensive Center (HDFCCC), University of California, San Francisco, CA, USA. ⁴Center for Nanomedicine, Institute for Basic Science (IBS), Seoul, Republic of Korea. ⁵Graduate Program of Nano Biomedical Engineering (Nano BME), Advanced Science Institute, Yonsei University, Seoul, Republic of Korea. ⁶SKKU Advanced Institute of Nanotechnology (SAINT), Sungkyunkwan University, Suwon, Republic of Korea. ⁷Department of Nano Engineering, Sungkyunkwan University, Suwon, Republic of Korea. ⁸Imnewrun Inc., Suwon, Republic of Korea. ⁹Department of Pharmacology, Yonsei University College of Medicine, Seoul, Republic of Korea. ¹⁰Department of Psychiatry and Neuroscience, Icahn School of Medicine at Mount Sinai, New York, NY, USA. ¹¹Department of Neurology, University of California, San Francisco, CA, USA. ¹²Department of Cell and Tissue Biology, University of California, San Francisco, CA, USA. ¹³Department of Physics and Chemistry, DGIST, Daegu, Republic of Korea. ¹⁴Brain Korea 21 Plus Project, Yonsei University College of Medicine, Seoul, Republic of Korea. ¹⁵Severance Biomedical Science Institute, Yonsei University College of Medicine, Seoul, Republic of Korea. ¹⁶Department of Chemistry, Yonsei University, Seoul, Republic of Korea. ¹⁷Chan Zuckerberg Biohub, San Francisco, CA, USA. ¹⁸These authors contributed equally: Minsuk Kwak, Kaden M. Southard, Woon Ryoung Kim. ✉e-mail: zev.gartner@ucsf.edu; young-wook.jun@ucsf.edu

Methods

Plasmid construction

Plasmid constructs used in this study are listed in Supplementary Table 1. All constructs used in this paper were assembled using standard restriction enzyme-based cloning, in-fusion cloning and/or Gibson isothermal assembly. The maps, sequences and construction details of all plasmids are available upon request. All constructs were sequenced to confirm mutation. All primers were purchased from Integrated DNA Technology. Complete details of all cloning procedures are available upon request.

Flag-human Notch1 (N^{FL})-Gal4 and pGF1-UAS-H2B-mCherry were gifts from S. Blacklow (Harvard University). Flag-human N^{FL}-Gal4 was provided in a Tet-ON Flp-IN vector (pcDNA5). SNAP-N^{FL}-mCherry and SNAP-N^{FL}-Gal4 were constructed as previously reported³⁰. All Notch1 variants with partial or full ECD truncation were constructed by linearizing and amplifying SNAP-hNI-mCherry vector via inverse PCR while omitting the sequence corresponding to the ECD truncation. Notch ectodomain sequences of amino acids 23–981, 23–1,426 and 23–1,709 were deleted for SNAP-ΔEGF₁₂₅-mCherry, SNAP-ΔEGF-mCherry and SNAP-NEXT-mCherry, respectively. Note that similar Notch variants with partial ECD truncation were reported previously³¹ where the structural integrity and function of Notch NRR domain were preserved. Ecad-GFP was purchased from Addgene (plasmid number 28009; <http://n2t.net/addgene:28009>). SNAP-Ecad-GFP and Halo-Ecad-GFP were constructed first by linearizing and amplifying Ecad-EGFP vector via inverse PCR. SNAP- and Halo tags were then inserted in frame with E-cadherin, downstream of the E-cadherin pro-peptide (amino acid number 155) and upstream of the ECD sequence, using Gibson assembly (NEB). pCMV6-Flotillin-1-Halo (Flot1-Halo) was constructed by replacing the myc tag within the pCMV6-Flotillin1-myc (purchased from Origene (MR206823)) with the Halo-tag sequence in frame with Flot1 using In-Fusion cloning (Clontech). Human amyloid precursor protein1-EGFP (APP-EGFP) was created by cloning human APP695 (a gift from C. Miller of King's College London) into a pEGFP-N1 plasmid (Clontech). To facilitate membrane distribution mapping, we used APP constructs used in confocal imaging lack YENPTY motifs (Fig. 7a,b), and compared the result with full-length APP (Fig. 7a,b). APP^{ΔYENPTY}-EGFP was constructed by first linearizing the vector via inverse PCR, and deleting the sequence of final 15 amino acids upstream of C-terminus of APP (amino acids 681–695), which includes YENPTY motif (amino acids 682–687) using Gibson assembly.

shRNA targeting ADAM10 was inserted into the lentiviral expression vector pLV-mTurquoise-MLC-IRES-neo (addgene plasmid number 85145) using BamHI. The targeting sequences were gacatttcaacctgaat for ADAM10 messenger RNA⁹³. To form the shRNA, sequences were separated by a non-complementary spacer (tcaagaga) from their corresponding reverse complement sequence. Lentiviral particles for ADAM17 shRNA (sc-36604-V) were purchased from Santa Cruz Biotechnology.

Tissue culture

Human U2OS cells were cultured in McCoy's 5A medium supplemented with 10% heat-inactivated FBS (Life Technologies) and 1% Pen-Strep (Life Technologies) and passaged with 0.05% trypsin–EDTA. Madin-Darby canine kidney (MDCK) cells were grown in Eagle's Minimum Essential Medium (University of California, San Francisco (UCSF) cell culture facility) supplemented with 10% heat-inactivated FBS and 1% Pen-Strep. MDCK cells were lifted by treating for 10 min with PBS Ca²⁺ and Mg²⁺ free with 0.05% EDTA followed by trypsinization. Human umbilical vein endothelial cells were purchased from ATCC (ATCC CRL-1730) and grown in Endothelial Cell Growth Medium-2 (EGM-2, Lonza CC-3162) for up to four passages (0.05% trypsin–EDTA) after thawing. Human immortalized keratinocyte cell line, HaCaT, was purchased from ATCC (ATCC PCS-200-011) and grown in Dulbecco's modified Eagle medium (Gibson) supplemented with 10% FBS and 1% Pen-Strep. All cell lines

were maintained at 37 °C in a humidified incubator with 5% CO₂ and passaged every 2–3 days, depending on confluency, using 0.05% trypsin–EDTA (UCSF cell culture facility). For polarized MDCK culture, cells were for use on a transwell filter (0.4 μm, collagen coated) at high density. All cells were authenticated on the basis of their morphology, growth condition and immunostaining with specific markers. The plain U2OS and Flp-IN T-rex U2OS cell lines were previously authenticated in Seo et al.³⁰ and Kim et al.⁹⁰.

Transfection and cell line generation

All cell lines expressing recombinant proteins used in this study are listed in Supplementary Table 1. U2OS stable cell lines were constructed from parental U2OS T-rex cell lines (Flp-IN, Tet-ON engineered cell line, gift from S. Blacklow). Constructs were inserted into the engineered Flp-IN site by co-transfection with a plasmid containing the Flp-recombinase (pOG44) via electroporation with the Neon Transfection System (ThermoFisher) according to the manufacturer's protocol (shock conditions: 1,230 V, 10 ms, four pulses, number of cells 5 × 10⁶). The amount of total DNA used was 10 μg per well: 1 μg of DNA containing the desired construct and 9 μg pOG44. Cells transfected with desired plasmids were incubated in a selection medium containing 400 μg ml⁻¹ hygromycin (Invitrogen) for at least 10 days. All cells with Notch truncation and reporter were further sorted for inducible expression of Notch variants via fluorescence-activated cell sorting on a FacsAria2 (BD) by staining for the appropriate tag (SNAP or Halo) with fluorescently tagged antibody. For single-cell monoclonal population establishment, fluorescently positive bulk-sorted populations were plated into 96 well plates at 0.2 cells per well by serial dilution and grown in selection medium. Each clonal cell population was tested and selected on the basis of the levels of Notch reporter activity or Notch membrane expression. U2OS cells expressing recombinant proteins transiently were generated by transfecting plasmids encoding desired proteins using Neon-based electroporation. Cells were allowed to settle in a six-well cell culture dish post-electroporation for 6–8 h. To remove dead cells, cells were lifted and re-plated on a fibronectin-coated glass-bottom dish at a density of 1 × 10⁵ cells per well. MDCK cells were plated at 70% density then transfected with N^{FL}-mCherry utilizing Lipofectamine 3000 (ThermoFisher) or Neon electroporation according to the manufacturer's protocol (shock conditions: 1,650 V, 20 ms, one pulse, number of cells 5 × 10⁶). Human umbilical vein endothelial cells were transfected via electroporation with SNAP-N^{FL} via the Bio-Rad Gene Pulser system (250 V, 20 ms square wave, 1 × 10⁶ cells ml⁻¹ Gene Pulser Electroporation Buffer, 5 μg ml⁻¹ SNAP-N^{FL}-mC). All cells transiently expressing recombinant proteins were incubated for 24–48 h from the transfection, and then used for further analyses.

Live cell mechanogenetics experiment

Mechanogenetics experiments were performed as previously described in Kwak et al. with some modifications^{30,56,57}. Monovalent magnetofluorescent nanoparticles (MFNs) were synthesized as previously described⁵⁷.

Micro-magnetic tweezers (μMT) setup. The μMT was set up and aligned on the inverted microscope with point-scanning confocal imaging capabilities (Nikon) as previously described^{30,57,94}. The needle probe–NdFeB magnet assembly was attached to the z-translation stage (Sutter Instrument, MP-325), and its location was carefully aligned with the microscopic objective lens while observing the dummy substrate filled with DPBS. The μMT tip was positioned at the centre of the objective oculus with bright-field illumination using the X–Y translation stage linked to PIMikroMove (Physik Instrumente) and μManager (UCSF). Using the z-translation stage, the μMT was carefully lowered to set the height of the tip to 10 μm above the focal plane while recording the X–Y coordinates and the z-position of the needle probe.

Preparation of cells expressing recombinant Flotilin-1 for mechanogenetics experiments. U2OS cells were co-transfected with SNAP-Ecad-GFP (5 μg) and Flot1-Halo (5 μg) plasmids using Neon electroporation. Twenty-four hours later, cells were re-plated on a #1.5 glass-bottom dish (MatTek, $d = 10\text{ mm}$) coated with collagen at a density of 1×10^5 cells per dish. To fluorescently label Flot1-Halo, cells were treated in a complete McCoy's 5A medium containing 3.5 μM cell membrane permeable Halo-ligand 660 dye (Promega) for 30 min at 37 °C. Cells were washed three times with DPBS, incubated with a phenol-red-free complete medium, and then mechanogenetically stimulated (see below). For the cholesterol depletion experiment, we also treated cells 10 mM of M β CD (Sigma-Aldrich) in serum-free McCoy's 5A medium for 30 min at 37 °C and washed with complete medium three times. To label SNAP-Ecad-GFP with MFNs, cells were first treated with 5 μM of an oligonucleotide bearing benzylguanine (BG-T₆₀ACTG₁₀) for 45 min at 37 °C, washed two times with 10 ml of serum-free medium, and then incubated with serum-free medium containing 10 nM monovalent MFNs bearing complementary sequence (T₆₀CAGT₁₀) and 0.5% alkali casein for 10 min at 37 °C, 5% CO₂. Cells were washed with 10 ml of complete medium two times, and then incubated with phenol-red-free medium for mechanogenetic experiments on a confocal or wide-field epifluorescence microscope.

Preparation of cells expressing human Notch1 receptor for the mechanogenetic experiment. Inducible U2OS cells stably integrated with SNAP-N^{FL}-mCherry were transfected with Halo-Ecad-GFP (10 μg) using Neon electroporation. Twenty-four hours later, cells were re-plated on a collagen (or fibronectin)-coated glass-bottom dish. To induce surface expression of SNAP-N^{FL}-mCherry, cells were incubated with complete medium containing doxycycline (Sigma, 2 $\mu\text{g ml}^{-1}$) for 18 h. To inhibit γ -secretase activity, cells were treated with DAPT (5 μM) and further incubated for 6 h. Cells were treated with 5 μM of an oligonucleotide bearing chloroalkane (Cl-T₆₀ACTG₁₀) for 45 min at 37 °C and labelled with MFNs via the procedure described above.

Mechanogenetic regulation of artificial E-cadherin junctions. To induce MFN and hence cadherin clustering, the μMT was carefully directed towards a targeted subcellular location until the tip-to-membrane distance (d) reached 10 μm . As the tip approached the target membrane, the formation of an artificial E-cadherin junctions (AJs) was monitored every 5 min. After 30 min of mechanogenetic stimulation, the spatial distribution of MFNs and artificial AJs was monitored using time-lapse confocal fluorescence imaging. To investigate γ -secretase processing of full-length Notch, the spatial distribution of membrane mCherry (S-N^{FL}-mC) or nuclear mCherry signals (S-N^{FL}-Gal4) were monitored using time-lapse live cell confocal imaging. To observe localization of membrane microdomains, the spatial distribution of Flot1 fluorescence signal was monitored using live cell confocal imaging. Time-lapse live cell confocal imaging was performed using a 60 \times Plan-Apo oil objective (numerical aperture (NA) 1.4) on a Nikon A1 laser scanning confocal microscope equipped with an environmental chamber maintaining cells at 37 °C, 5% CO₂. Cells were immediately fixed with 4% paraformaldehyde (Life Technologies) in DPBS for 15 min and washed with DPBS three times for 5 min before immunostaining.

Fluorescence labelling and immunostaining

Fluorescence labelling of cells expressing SNAP- or Halo-tag proteins. Cells expressing SNAP- and/or Halo-tagged fusion proteins were labelled with BG- and/or chloroalkane-functionalized fluorescence dyes, respectively. Dox-inducible cell lines grown on a collagen-I-coated substrate were treated with doxycycline (2 $\mu\text{g ml}^{-1}$) 24 h before labelling. Cells with transient receptor expression were labelled with dyes 48 h post-transfection. Dye labelling was performed by treating the cells with 5 μM fluorescence dye in serum-containing medium for 30 min. Cells were then washed three times with complete medium.

For live cell imaging, cells were incubated with phenol-red-free complete medium. For imaging of fixed cells, cells were washed with PBS, fixed with 4% paraformaldehyde in PBS for 10 min and then washed thoroughly with PBS.

Immunofluorescence staining. Fixed cells were permeabilized with 0.5% Tween-20 diluted in PBS for 15 min, then blocked by incubation with blocking buffer (5% normal goat serum and 1% BSA in 1 \times PBS) for 1 h in room temperature. For immunostaining of surface ADAM10 and ADAM17 expression, the sample was directly blocked without a permeabilization step. Cells were incubated overnight at 4 °C or 2 h at 25 °C with the primary antibodies: mouse monoclonal anti-ADAM10 (1:100; Santa Cruz Biotechnology), mouse monoclonal anti-ADAM17 (1:200, R&D Systems), rabbit polyclonal anti-PS1 antibody R222 (1:50) (ref. ³²), rabbit monoclonal anti-Nicastrin (1:200, Santa Cruz Biotechnology), mouse polyclonal anti-Paxillin (1:500; BD Bioscience), rabbit polyclonal anti-myc tag (1:200; abcam), mouse monoclonal anti-VE-cadherin (1:400, BD Biosciences) and Alexa Fluor 488 Phalloidin (1:400 dilution of 200 units ml⁻¹ stock; Life Technologies). All antibodies were diluted in the 0.5 \times blocking buffer (2.5% normal goat serum and 0.5% BSA in 1 \times PBS). Following primary antibody incubation, cells were washed in PBS for 5 min four times and incubated with Alexa Fluor 405 goat anti-mouse (1:400, PS-1), Alexa Fluor 594 conjugated goat anti-mouse (1:400; Paxillin), Alexa Fluor 488-conjugated goat anti-mouse (1:400; VE-cadherin), Alexa Fluor 647-conjugated goat anti-mouse (1:500, ADAM10) and Alexa Fluor 647-conjugated goat anti-rabbit (1:500, nicastrin) as appropriate. Nucleus staining was performed using Hoechst 33342 (ThermoFisher) diluted in 1 \times PBS (1 $\mu\text{g ml}^{-1}$) for 15 min and then washed once. Cells were incubated at room temperature in the dark for 1 h, washed with PBS for 5 min three times, and imaged by epifluorescence or confocal microscopy. Epifluorescence microscopy was performed with 60 \times Apo, 1.40 NA or 100 \times Apo, 1.49 NA oil objectives (Nikon) on a Nikon Ti Eclipse microscope equipped with OBIS solid-state lasers (488, 552 and 647 nm, Coherent), a 300 W Xenon lamp (Sutter Instrument, Lambda LS), a motorized stage (ASI, MS-2000), and a temperature- and CO₂-controlled stage top incubator (Okolab, Bold Line). Unless otherwise noted, confocal microscopy was performed using Plan-Apo 60 \times , 1.4 NA or Plan-Apo 100 \times , 1.4 NA oil objectives (Nikon) on a Nikon AIR laser scanning confocal microscope. Images were acquired using Galvano scanning mode and confocal zoom of 3–4 \times magnification.

Spatial distribution of Notch signalling molecules at cellular interface

We used three different cell culture model systems to investigate spatial distribution of Notch1 during its surface activation: Notch ligand- and receptor-expressing cells that form the signalling interface (1; Fig. 1a–c), the signalling interface formed by the cells exclusively expressing either Notch ligand or receptor (2; Extended Data Fig. 1a,b,d), and Notch-expressing cells cultured on a Dll4-coated substrate (2; Fig. 1d–f).

Model system 1. U2OS cells co-expressing SNAP-N^{FL}-mCherry and Halo-Dll1 were plated on a collagen-coated #1.5 glass-bottom Mattek dish at a density of 2×10^5 cells ml⁻¹. Cells were incubated with the appropriate inhibitors, either TAPI2 (100 μM), shRNA cocktails against ADAM10/17, and/or DAPT (5 μM). Different combinations of inhibitors were used to capture the respective intermediates. After 48 h, cells were labelled with SNAP-594 (NEB, 5 μM) and Janelia Fluor HaloTag 646 (Promega, 5 μM). Then cells were then fixed and immunostained for PS1 using the protocol described above. Briefly, following the permeabilization and blocking steps, cells were incubated overnight at 4 °C with rabbit polyclonal anti-PS1 and 1 h at 25 °C with AF405-conjugated goat anti-rabbit antibodies. Respective inhibitors were maintained during wash and fixation steps. Spatial distribution of respective Notch signalling molecules was then imaged with a confocal fluorescence microscope, as described above.

Model system 2. We repeated identical experiments where cells exclusively expressing either SNAP-N^{FL}-mCherry or Halo-Dll1 were co-cultured with the ratio of 1:1, to form *trans* ligand–receptor interactions exclusively. We observed amplified mCherry signals at some RIP microdomains upon rescuing ADAM10/17 activity in the presence of DAPT (Extended Data Fig. 1d; box (i) and (ii)), but we also observed decreased mCherry signals at other RIP microdomains (Extended Data Fig. 1d; box (iii)). Because both full-length Notch and the Notch intermediate (that is, S2-processed Notch1) bear mCherry tag, spatial mapping of the activated Notch intermediate using mCherry fluorescence is challenging unless the fraction of the Notch intermediate is much higher than unprocessed full-length Notch. We reasoned that the relatively small cell–cell contact area (0.5–10 μm²) and low ligand density (<300 molecules μm⁻²)⁹⁵ limited receptor activation in this configuration, and hence the mCherry fluorescence signal from unprocessed Notch overwhelmed that from S2-processed Notch in some areas of the cell.

Model system 3. To maximize the ligand–receptor engagement and hence robust Notch activation, we used culture system 3 allowing high-density ligand loading (>3,000 molecules μm⁻²) and increased ligand–receptor contact area (100–500 μm²) (ref.⁷). To activate Notch, we plated cells expressing SNAP-N^{FL}-mCherry on a substrate coated with Dll4 fused with a Fc fragment (Dll4-Fc). Briefly, a glass-bottom dish (Lab-Tek II Chambered Coverglass, ThermoFisher, or 7 mm glass-bottom dish, MatTek) was coated with fibronectin (hamster, 5 μg ml⁻¹) and Dll4-Fc (2.5 μg ml⁻¹) for 1 h at 37 °C, and washed thoroughly with 10 ml of PBS. A negative-control dish was also prepared by coating it with fibronectin only. U2OS cells co-expressing SNAP-N^{FL}-mCherry and Ecad-GFP were plated and incubated with doxycycline (2 μg ml⁻¹), TAPI2 (100 μM) (ref.⁹⁶) and/or DAPT (5 μM). Different combinations of inhibitors were used to capture the respective intermediates. After 48 h, cells were labelled with SNAP-647 (NEB, 5 μM) and then fixed as detailed above. Inhibitor concentrations were maintained during wash and fixation steps. In this system, significantly more Notch becomes activated, and as a result, we observed strong enrichment of mCherry signals within the RIP microdomain as presented in Fig. 1d–f, indicating translocation of Notch after S2 cleavage.

To map spatial dynamics of Notch relative to AJs during activation (Extended Data Fig. 3a–e), we plated U2OS cells co-expressing SNAP-N^{FL}-mCherry and Ecad-GFP on a Dll4-Fc coated substrate to trigger Notch activation as described above. Cells were also treated with TAPI2 (S2 cleavage inhibition) or DAPT (S3 cleavage inhibition) to capture Notch intermediates. For time-lapse imaging (Extended Data Fig. 3d,e), we washed the cells with large volumes of PBS to remove DAPT, incubated cells with DAPT-free medium, and imaged at each timepoint (0, 0.5, 1.5, 3, 6 and 12 h), respectively. The spatial distribution of Notch intermediates and AJs was monitored using spinning disk confocal fluorescence microscopy (Zeiss Cell Observer Z1), equipped with Yokagawa spinning disk and Evolve 512EMCCD camera (Photometrics). Images were obtained with Plan-Apo 63×, 1.4 NA or Plan-Apo 100×, 1.46 NA oil objectives (Zeiss) with solid-state lasers of 405, 488, 561 nm and 647 nm. The microscope was controlled with Zeiss Zen software (Zeiss).

Spectral GP imaging of the live-cell plasma membrane

Cells were prepared for di-4-ANEPPDHQ imaging as previously reported⁴⁹. Briefly, U2OS cells expressing Ecad-GFP were plated on a fibronectin-coated glass bottom dish and incubated with di-4-ANEPPDHQ (Invitrogen, 2 μM) for 30 min at 37 °C in a humidified 5% CO₂ atmosphere. Cells were then washed three times with PBS. Spectral imaging was performed on a Nikon AIR laser scanning confocal microscope equipped with a 32-channel GaAsP detector array. Laser at 488 nm was selected for excitation and the detection range was set between 495 nm and 750 nm for di-4-ANEPPDHQ. Calculation and generation of GP images were performed as previously

described using the provided ImageJ plugin macro codes⁴⁹. GP values for di-4-ANEPPDHQ imaging were calculated according to the following equation: $GP = \frac{I_{500-580} - G \times I_{620-750}}{I_{500-580} + G \times I_{620-750}}$ and G (the G factor) = $G = \frac{GP_{ref} + GP_{ref} \times GP_{mes} - GP_{mes} - 1}{GP_{mes} + GP_{ref} \times GP_{mes} - GP_{ref} - 1}$. For the imaging of cell membranes, GP_{ref} is ~0.85. GP_{mes} is the GP value of di-4-ANEPPDHQ dye in pure dimethylsulfoxide (DMSO) measured with the same microscope setup. The plugin applies above calculation to produce a histogram of the GP map and a pseudo-coloured GP map representing the GP value for each pixel of the image.

Single-cell cleavage kinetics of SNAP-NΔEGF-mC

A six-channel μ-slide flow chamber (Ibidi, VI 0.4) was coated with fibronectin (2.5 μg ml⁻¹) for 1 h at 37 °C and washed with PBS four times. U2OS cells co-expressing SNAP-NΔEGF-mCherry and Ecad-GFP were plated on the μ-slide flow chamber by applying 60 μl of single-cell suspension at a density of 3 × 10⁵ cells ml⁻¹. After 3 h, the channel was filled with a complete McCoy's 5A medium containing doxycycline (2 μg ml⁻¹), TAPI2 (100 μM) and DAPT (5 μM). Cells were grown for 48 h in normal growth medium to reach 70–80% confluency and form cadherin AJs. Cells were labelled with BG-Alexa Fluor 647 (NEB) for 30 min to stain cell surface NΔEGF. Multiple cells with stable AJs were identified using large-area epifluorescence scanning (500 μm × 500 μm), and the spatial distribution of SNAP-NΔEGF-mCherry at AJs under TAPI2 and DAPT inhibition was imaged by confocal z-stack (step size 0.2 μm, total range of z-stacks 10 μm) scanning from basal to apical membranes. Then, DAPT-containing medium was removed and replaced by flowing complete medium containing doxycycline and TAPI2 at a flow rate of 50 μl min⁻¹ for 10 min using a syringe pump. Localization of NECD and NICD at the AJs before and during DAPT washout was monitored every 30 min in multiple colour channels (NICD, mCherry; NECD, AF647; AJ, GFP) by time-lapse confocal z-stack microscopy for 12 h. Time-lapse live cell confocal imaging was performed using a 60× Plan-Apo oil objective (NA 1.4) on a Nikon A1 laser scanning confocal microscope equipped with an environmental chamber maintaining cells at 37 °C, 5% CO₂.

Western blot analysis

U2OS cells co-expressing Notch variants and Ecad-GFP (or Halo-Ecad-GFP) were incubated with culture medium containing doxycycline (2 μg ml⁻¹) and TAPI2 (100 μM) in a six-well plate at a density of 1 × 10⁶ cells per well. After 24 h, cells were washed with ice-cold DPBS twice and lysed in RIPA (Invitrogen) or 1% NP-40 (Invitrogen) supplemented with complete protease and phosphatase inhibitor cocktail (100×; Cell Signaling Technology) at 4 °C while gently shaking for 30 min. Insoluble fractions were removed by centrifugation of the cell lysates at 13,000 rpm for 10 min. Total protein concentrations in lysates were determined by a BCA assay (Bio-Rad). Twenty micrograms of whole-cell lysates were then mixed with 4× Laemmli sample buffer (Bio-Rad) with 10% β-mercaptoethanol and heated to 95 °C for 5 min. For western blot analysis of DNA-crosslinked heterodimers, the cell lysates were mixed with 4× Laemmli sample buffer (Bio-Rad) without β-mercaptoethanol before boiling to denature. Samples were then loaded into a 4–15% Mini-Protein TGX precast gel (Bio-Rad) and were run at 70 V for 30 min and then 120 V for 45 min. Separated proteins were transferred to a PVDF membrane using Mini Trans-Blot Cell (100 V constant, 1 h) or the Trans Turbo Blot system (Bio-Rad). Membranes were blocked for 1 h at room temperature in blocking solution (5% w/v non-fat dry milk in 1× TBST). The membranes were probed with anti-V1744 NICD antibody (1:1,000; Cell Signaling Technology #4147), anti-SNAP (1:1,000; NEB), anti-Notch1 (1:1,000, Cell Signaling Technology #3447 or #4380), anti-mCherry (1:500, Abcam #167453), anti-E-cadherin (1:100, Santa Cruz Biotechnology, sc-8426) and anti-β-actin (1:5,000; Cell Signaling Technology #4970) antibodies overnight at 4 °C with gentle rocking. The membranes were washed in TBST three times for 5 min and incubated with an anti-rabbit (Cell

Signaling Technology, at 1:2,000 for NICD, mCherry, SNAP detection and at 1:10,000 for β -actin detection) or anti-mouse (Cell Signaling Technology, at 1:2,000 for E-cadherin detection) HRP-conjugated antibody. The target proteins were visualized by chemiluminescence using an ECL detection kit and a ChemiDoc MP imaging system (Bio-Rad). Quantification of band intensities by densitometry was carried out using the Image Lab software (Bio-Rad). For quantification, the average intensity of NICD band was normalized to that of β -actin band in each sample, unless otherwise noted.

Spatial mutation of SNAP- Δ EGF-mCherry via DNA crosslinking

DNA-mediated crosslinking of SNAP- Δ EGF-mCherry with Halo-Ecad-GFP. DNA crosslinkers including benzylguanine (BG)- and chloroalkane (Cl)-modified oligonucleotides were synthesized as previously described. To prepare 10 \times crosslinking DNA stock solution, complementary BG- and Cl-modified oligonucleotides were hybridized in situ. BG-T₁₀(ACTG)₅ and Cl-T₁₀(CAGT)₅ were mixed at equimolar concentration (20 μ M) in PBS, incubated at 95 $^{\circ}$ C on a dry heat block for 5 min, and slowly cooled down to room temperature for 2 h. U2OS cells co-expressing SNAP- Δ EGF-mCherry and Halo-Ecad-GFP were cultured in a six-well plate for western blot analysis at a density of 1×10^6 cells ml⁻¹ or in a channel of an Ibidi μ -slide for confocal imaging analysis at a density of 3×10^5 cells ml⁻¹. Cells were grown to 70–80% confluency for typically 24 h, followed by overnight incubation with complete medium containing doxycycline (2 μ g ml⁻¹), TAPI2 (100 μ M) and DAPT (5 μ M). Cells were then serum starved with 2 ml of serum-free medium with doxycycline, DAPT, and TAPI2 for 6 h. Before adding DNA crosslinkers, cells were washed and placed in 450 μ l of serum-free medium. Fifty microlitres of pre-warmed 10 \times DNA crosslinker stock solution was added to each well and incubated at 37 $^{\circ}$ C. Western blot analysis to validate receptor crosslinking was performed after 30 min incubation of the DNA crosslinkers as detailed above.

Live cell confocal time-lapse imaging. After overnight incubation with the DNA crosslinkers, imaging was performed on an inverted laser scanning confocal microscope (Nikon A1) equipped with an environmental chamber at 37 $^{\circ}$ C and 5% CO₂. Images were obtained with a Plan-Apochromat 60 \times , 1.4 NA oil objective (Nikon) with solid-state lasers of 405, 488, 561 and 647 nm. Additionally, the microscope was equipped with Ti-E Perfect Focus System (Nikon). To examine the effect of DNA-mediated crosslinking on spatial distribution of SNAP- Δ EGF-mCherry at AJs, multiple AJs were imaged in entirety from basal to apical sides for Halo-Ecad-GFP and SNAP- Δ EGF-mCherry using a 488 nm and 561 nm laser, respectively, for a 12 μ m range at a z-step size of 0.25 μ m. To monitor dissipation of SNAP- Δ EGF-mCherry at AJs upon removal of DAPT inhibition, fresh phenol-red-free McCoy's 5A medium containing doxycycline and TAPI2 was introduced into the channel using a syringe pump for 10 min, and confocal z-stack images of the previously selected AJs were acquired every 30 min for 6 h. Images were acquired using NIS-element software (Nikon), and image post-processing and analyses were done using Fiji/ImageJ and custom-built scripts.

Spatial mutation of SNAP-NEXT-mCherry via molecular pendant addition

Synthesis of BG-modified PEG. Amine-functionalized polyethylene glycols (PEGs) with different molecular weights and structures were purchased from Creative PEGWorks (NH₂-PEG3.4k), Sigma (NH₂-bPEG20k) and NanoCS (NH₂-tPEG20k) and used without further purification. BG functionalization of PEGs was performed by amine-NHS (N-hydroxysuccinimide; NEB) coupling reaction. Briefly, NH₂-PEG (0.5 μ mol), BG-GLH-NHS (2.4 mg, 5 μ mol), and *N,N*-dimethylaminopyridine (0.73 mg, 6 μ mol; Sigma) were dissolved in anhydrous DMSO. The mixture allowed to react overnight with

constant shaking. Crude products were recovered by evaporating DMSO using a Speed-Vac concentrator (Vacufuge, Eppendorf), reconstituted in 500 μ l de-ionized water, and insoluble precipitates were removed by centrifugation at 14,000 rpm for 10 min. The BG-modified PEG was then dissolved in 200 μ l in de-ionized water and purified by reverse-phase high-performance liquid chromatography with an Agilent Eclipse XDB C-18, 5 μ m, 4.6 \times 250 mm² column using an elution gradient of 5–75% acetonitrile in 0.02% trifluoroacetic acid.

Synthesis of BG-modified DNA-stv. DNA oligonucleotides bearing biotin- and BG-functional groups were synthesized by reacting biotin-(ACTG)₅-NH₂ (Integrated DNA Technology) with BG-GLH-NHS as described above⁶³. Equimolar amounts of streptavidin (10 nmol) and BG-DNA-biotin (10 nmol) were dissolved in PBS (0.5 ml) for 2 h, forming streptavidin-BG complex. The solution was concentrated to approximately 50 μ l using an Amicon centrifugal filter (molecular weight cut-off 30,000) and then diluted again with 0.45 ml of PBS. This concentration and reconstitution step was repeated three times to remove unconjugated DNA.

Synthesis of BG-modified hlgG. hlgG (10 mg) and BG-GLA-NHS (0.82 mg) were dissolved in 850 μ l of PBS and 150 μ l of anhydrous DMSO, respectively. Two solutions were mixed and reacted for 2 h at room temperature with gentle shaking. The solution was desalted with NAP-10 and then with NAP25 pre-equilibrated with PBS. The proteins were further concentrated until the final volume is 300–500 μ l using Amicon centrifugal filter (molecular weight cut-off 30,000). The IgG concentration was determined by measuring the absorbance at 280 nm.

Spatial mutation of SNAP-NEXT-mCherry using the BG-modified macromolecules. U2OS cells co-expressing SNAP-NEXT-mCherry and Ecad-GFP were incubated in complete McCoy's 5A medium containing doxycycline (2 μ g ml⁻¹), TAPI2 (100 μ M), DAPT (5 μ M) and respective BG-modified macromolecules (10 μ M). After 24 h, cells were fixed and imaged by confocal microscopy to determine the enrichment factor of SNAP-NEXT-mCherry at AJs. Images were taken with a 100 \times objective and 3 \times confocal zoom. Twenty stage positions per each treatment were manually selected, and their coordinates were stored in the computer. In each position, confocal z-stacks of DAPI, Ecad-GFP and Notch-mCherry were acquired for a 12 μ m range at a z-step size of 0.25 μ m to monitor the AJs in their entirety from basal to apical sides. To assess the levels of Notch activation, a set of identical experiment but without DAPT was performed. After 24 h, cells were fixed, stained with DAPI and imaged by confocal microscopy to determine nuclear mCherry signal. Images were taken with a 60 \times objective and 1 \times confocal zoom. Five stage positions per each condition were selected manually. For each position, a confocal large-area scan of DAPI, Ecad-GFP and SNAP-NEXT-mCherry was acquired for a 1 mm \times 1 mm area.

Plate-bound Dll4 Notch activation in high-density grouped versus solitary cells

To activate Notch, we plated SNAP-N^{FL}-Gal4 reporter cells on a substrate coated with Dll4-Fc as detailed above. Two different cell seeding densities were used: We plated cells with a density of 1×10^3 cells per 10 mm glass-bottom dish (MatTek, No. 1.5 glass), predominantly yielding solitary cells. We also plated cells with a density of 1×10^4 cells per dish, predominantly yielding high-density grouped cells.

Plate-bound E-cadherin Notch activation experiment. Glass-bottom dishes (MatTek, #1.5, *d* = 10 mm) were coated with recombinant human E-cadherin-Fc (50 μ g ml⁻¹, R&D Systems), recombinant human Dll4-Fc (2.5 μ g ml⁻¹, Sino Biological) and fibronectin (5 μ g ml⁻¹, Sino Biological) diluted in PBS for 1 h at 37 $^{\circ}$ C, and rinsed with 10 ml PBS with calcium and magnesium (UCSF cell culture facility). The U2OS

SNAP-N^{FL}-Gal4 reporter cells were transfected with Ecad-GFP (10 µg) via electroporation, incubated overnight and re-plated onto a fibronectin, E-cadherin-Fc and Dll4-Fc coated glass-bottom dish at a density of 0.3×10^5 cells ml⁻¹, same as the solitary cell assay. Negative-control experiment was performed with the cells plated on E-cadherin-Fc- and fibronectin-coated glass-bottom dishes without Dll4-Fc coating.

Time-lapse epifluorescence imaging. All cells were treated with 2 µg ml⁻¹ doxycycline (Sigma-Aldrich) at the time of plating. Two hours post-plating, cells were imaged using time-lapse microscopy. For a high-density cell seeding assay, several groups of cells having cell–cell contacts were manually identified and their coordinates were stored. For a solitary cell assay, a number of solitary cells without any prior cell–cell contact were manually identified and their coordinates were stored. While maintaining live cells on a microscope stage with a top stage incubator, time-lapse fluorescence images were acquired in GFP and mCherry channels. In each position, the microscope (Nikon) first found focuses using the Perfect Focus System (Nikon) and took a differential interference contrast (DIC) image and two fluorescent images (GFP, mCherry). To image multiple solitary cells and grouped cells in one large image, cells were first plated at a high density (2×10^5 ml⁻¹) at the centre, and after 15 min, cells were seeded at a low density (2×10^3 ml⁻¹) over the entire substrate area. After 24 h, cells were fixed and stained for membrane and nucleus. Epifluorescence images were obtained with an inverted microscope (Nikon, Ti Eclipse) equipped with 300 W Xenon lamp (Sutter Instrument, Lambda LS), a motorized stage (ASI, MS-2000) and a temperature- and CO₂-controlled stage top incubator (Okolab, Bold Line). Images were taken with 40× (CFI Plan fluor, NA 1.3, Nikon) objective lens. The microscopy setup was controlled using µ-manager software.

CRISPR editing to generate E-cadherin and N-cadherin knockout mutants

CRISPR–Cas9 was used to knock out E-cadherin and N-cadherin expression from U2OS SNAP-N^{FL}-Gal4 reporter cells. The genes coding for the E-cadherin (CDH1) and N-cadherin (CDH2) protein from *Homo sapiens* (gene IDs ENSG0000039068 and ENSG00000170558) were truncated by a CRISPR–Cas9 paired single guide RNA (sgRNA) excision strategy^{97,98}. For the fragment deletion of genomic DNA, we used a pair of gRNAs against the target locus of *CDH1* (exons 1 and 2 (940 bp deletion) or 13 and 14 (-4,712 bp deletion) (Extended Data Fig. 5a) and *CDH2* (exons 1 and 2 (-29,255 bp deletion) (Extended Data Fig. 5b) genes.

sgRNA design and expression vector cloning. Cas9 and sgRNAs were expressed using the CMV promoter-driven Cas9-2A-mRFP-2A-Puro plasmid (hereafter, Cas9-puro vector) and the hU6 promoter-driven sgRNA plasmid (Toolgen), respectively. To design sgRNAs for fragmental deletion of target loci of genes, all candidate sgRNA target sites with a protospacer-adjacent motif (5'-NGG-3') within the coding sequence of *CDH1* and *CDH2* were initially identified. For efficient deletion, selected sgRNAs for the candidate target sites were evaluated with DeepSpCas9 sgRNA prediction tool (<http://deepcrispr.info/DeepSpCas9/>)^{99,100}. sgRNAs with high DeepSpCas9 score were selected and sgRNA oligonucleotides annealed and cloned into the vector as previously described¹⁰¹. Sequences of the vectors and sgRNAs listed here are available upon request.

Generation of single-cell derived knockout clones. For CDH1 knockout, SNAP-N^{FL}-Gal4 reporter cells were transfected with plasmid mixtures containing Cas9-puro, U6-sgRNA encoding individual sgRNAs at a weight ratio of 1:2 using the Neon system. For CDH1/2 knockout, cells were transfected with plasmid mixtures containing Cas9-puro, U6-sgRNA targeting CDH1 loci, and U6-sgRNA targeting CDH2 loci at a weight ratio of 1:1:1 using the Neon system. One day after transfection, puromycin was added to the culture media at a final concentration of

2.5 µg ml⁻¹. Three days after transfection, the pooled cells were analysed for the indel efficiency of sgRNA pairs using T7E1 assay. To obtain single-cell-derived clones containing the fragment deletion, we plated the cells after puromycin selection into 96-well plates at an average density of 0.25 cells per well. Fourteen days after plating, individual clones were isolated and analysed using PCR and gel electrophoresis of genomic DNA to check the deletion and wild-type alleles. We next sequenced the genomic DNA of the clones containing targeted deletions to check if the two cleavage sites were joined by the generation of indels. Sequencing of genomic regions including the target sequence was performed as previously described¹⁰¹. Briefly, PCR amplicons that included the junction regions of the deleted lncRNA target sites were cloned into the T-Blunt vector (Promega) and sequenced using universal M13FP or RP primers.

T7E1 assay. The T7E1 assay was performed as previously described¹⁰². Briefly, genomic DNA was isolated using the Wizard Genomic DNA purification Kit (Promega) according to the manufacturer's instructions. The region including the target site was nested PCR-amplified using appropriate primers. The amplicons were denatured by heating and annealed to allow the formation of heteroduplex DNA, which was treated with 5 units of T7 endonuclease 1 (NEB) for 20 min at 37 °C followed by analysis using 2% agarose gel electrophoresis. Mutation frequencies were calculated as previously described on the basis of the band intensities using ImageJ software and the following equation:¹⁰² mutation frequency (%) = $100 \times (1 - (1 - \text{fraction cleaved})^{1/2})$, where the fraction cleaved is the total relative density of the cleavage bands divided by the sum of the relative density of the cleavage bands and uncut bands.

RT-PCR. Total RNA was extracted from wild-type SNAP-N^{FL}-Gal4 reporter (WT) cells and knockout clonal cells using TRIzol (Ambion) or an RNeasy Kit (QIAGEN), after which complementary DNA synthesis was performed using a DiaStar™ RT Kit (SolGent). The synthesized cDNA was subjected to quantitative PCR in triplicate using an Applied Biosystems StepOnePlus Real Time PCR System with PowerSYBR Green PCR Master Mix (Applied Biosystems). Gene expression was normalized to that of the *CDH1* gene in WT cells. Error bars represent the standard deviation (s.d.) of the mean of triplicate reactions. Primer sequences for quantitative PCR are available upon request.

Notch activation assay. WT cells, CRISPR *CDH1* knockout cells (*CDH1*^{-/-}), *CDH1*^{-/-} transfected with E-cadherin-GFP (*CDH1*^{-/-} + E-cad), and *CDH1*^{-/-} transfected with N-cadherin (*CDH1*^{-/-} + N-cad) were plated on eight-well Nunc Lab-Tek II chambered coverglass pre-coated with recombinant human Dll4-Fc (2.5 µg ml⁻¹) and fibronectin (5.0 µg ml⁻¹) as previously described. All cells were plated at a density of 30,000 cells per well. After 24 h incubation with doxycycline (2 µg ml⁻¹), cell cytoplasm and nucleus were stained with CellTracker CMFDA dye (Invitrogen) and Hoechst 33342 (ThermoFisher), respectively. The cells were then fixed with 4% paraformaldehyde for 15 min at room temperature and proceeded to epifluorescence and confocal imaging.

Aβ40, Aβ42 and sAPPα ELISA

A total of 1×10^6 of wild-type or CDH1/CDH2 knockout cells were transfected with APP-mCherry (10 µg) and plated on six-well tissue culture plate. After 48 h incubation, conditioned medium supplemented with 1× protease/phosphatase inhibitor cocktail (ThermoFisher) were centrifuged at 3,000g 10 min at 4 °C to remove cell debris and the supernatant were transferred to a new tube and stored at -80 °C. The conditioned media were analysed for Aβ40, Aβ42 and sAPPα contents using Aβ (Invitrogen) and sAPPα (Cusa Biosci.) ELISA kits. All ELISAs were performed according to the manufacturer's protocols. Briefly, 50 µl per well of samples, followed by 50 µl per well of detection antibodies, were applied to Aβ40, Aβ42, sAPPα-coated 96-well plate, and incubated for 3 h at room

temperature with shaking at 300 rpm. After washing, 100 μ l of HRP-IgG solution was applied and incubated for 30 min at room temperature with shaking. After washing, 100 μ l of stabilized substrate solution was applied and incubated for 30 min at room temperature with shaking. Finally, 100 μ l of stop solution was applied. Absorbance at 450 nm was read and analysed using a plate reader (Biotek Synergy 2). Wells were washed with wash buffer four times between each incubation step. Standard curves were generated using recombinant A β 40, A β 42, sAPP α provided by the manufacturer (Invitrogen).

In vivo experiments

Animals. We used CD-1 embryonic day 13.5 (E13.5) and post-natal day 3 (P3) newly born mice for in vivo experiments. P3 pups (four males and four females) were obtained by purchase of an untimed pregnant female mouse (E13–15) from Charles River Laboratories and waited for birth. Room temperature was maintained at 22 ± 1 °C with 30–70% humidity. All mice were housed under specific-pathogen-free conditions under a 12 h light–dark cycle, and all animal handling and use were in accordance with institutional guidelines approved by the University of California San Francisco Institutional Animal Care and Use Committee (AN180609-02B).

Retrovirus injection. To generate retrovirus, we used pWZL-GFP control vector (pWZL-Blast-GFP: addgene plasmid number 12269) and pWZL-dominant-negative E-cadherin (pWZL-Blast-DN-E-cadherin addgene plasmid number 18800, gift from Dr Kenji Shimamura). GFP sequence was inserted in frame with dominant-negative E-cadherin, downstream of C-terminus using In-Fusion cloning. For retrovirus production, we transfected retroviral vectors into Phoenix-Ampho cells using Calcium Phosphate Transfection Kit (Sigma, CAPHOS) with 50 μ M chloroquine (Sigma, C6628), and collected supernatant from transfected cells after 48 h. Collected supernatant containing viral solutions was ultracentrifuged yielding concentrated solution of viral particles (25,000 rpm for 2 h at 4 °C). Approximately 10^7 transducing units per millilitre (TU ml⁻¹) viral solution was injected into the lateral ventricular of neonatal mouse pups (P3). After hypothermic anaesthesia, viral solutions (5 μ l) were slowly injected using IM-9B Narishige microinjector with 2 μ l min⁻¹ speed. After recovery on the warming pad, the pups were placed back to the cage. After additional 2 h, mice were subject to intracardiac perfusion fixation using 4% paraformaldehyde in PBS.

DAPT injection. DAPT (10 μ M) was injected into neonatal mouse pups (P3) into a lateral ventricle (10 μ l in each hemisphere). DMSO was injected into control mice. After 7 h, mice were subject to fixation procedure using intracardiac perfusion of 4% paraformaldehyde in PBS.

Immunohistochemistry. Mice were perfused with 4% paraformaldehyde in PBS (pH 7.4) and the brains were subject to post-fixation in the same fixative for 24 h. Brains were then cryoprotected in 30% sucrose in PBS, sectioned serially (20 μ m) onto Superfrost Plus glass slides (Fisher Scientific). The brain slices were permeabilized and blocked with PBS solution containing 3% goat serum albumin and 0.3% Triton-X100, and then treated with anti-Ncadherin (1:200, ThermoFisher), anti-Notch (1:200, ThermoFisher), anti-PS1 antibody (1:50) and anti- β III tubulin (1:500, Abcam) overnight at 4 °C. The brain slices were washed three times with PBS and treated with secondary antibodies (1:1,000, ThermoFisher) for 30 min. Subsequently, the slices were washed with PBS, mounted and observed with a confocal microscope (Olympus, Fluoview 3000).

Image processing and analysis

Cadherin junction co-localization analysis. Co-localization analysis was carried out in ImageJ, using thresholding to identify AJs and then applying the JACOP plugin to quantify co-localization using Pearson coefficient, Manders' overlap coefficients and cross-correlation

analysis. All ImageJ macros and codes used for image post-processing and co-localization analysis have been deposited and are available at Github (<https://github.com/sukgi333/yonsei-notch-activation>).

Confocal 3D z-stack image processing. Custom Python code was used for automatic segmentation and junction intensity ratio analysis for Notch activation and truncation studies. Code is available at <https://github.com/kmsouthard/JunctionAnalysis>. In brief, resliced z-stacks of cell–cell interfaces were thresholded to identify the AJs and membrane Notch signal. To minimize the domination of high Notch intensity, we identified the membrane expressing Notch using a minimal threshold of membrane intensity just above background. An unbiased signal analysis window along each side the junction was selected, and the Notch membrane intensity was measured for each cell by averaging along the respective windows, while junctional intensity was measured within segments determined by cadherin junctional intensity. The ratio of junctional intensity was calculated as $\text{ratio} = I_{\text{junc}} / (I_{\text{cell1}} + I_{\text{cell2}})$ as deviations from the expected intensity at the junction is a function of the sum of each cell's expression level.

Intracellular mCherry nuclear translocation analysis. mCherry nuclear translocation analysis was carried out in ImageJ. GFP images were used for automated identification of cell edges and segmentation of single cells. DAPI images were used for automated identification of nucleus by implementing the Otsu thresholding method. Nuclear mCherry fluorescence data were extracted from nuclear segments by calculating the integrated fluorescence within the nucleus and subtracting a background scattering signal. In Fig. 4h, nuclear mCherry fluorescence intensities for NEXT cells treated with the macromolecular pendants were rescaled to make the intensity of N^{FL} and NEXT to 0.002 and 1.0, respectively, which are identical to the normalized band intensities of N^{FL} and NEXT measured by western blot.

Quantification of single-cell fluorescence. Single-cell tracking and nuclear mCherry fluorescence signal analysis of UAS-Gal4 reporter cells were performed with ImageJ, as previously described^{57,65,66}.

Western blot quantification. Quantification of band intensities by densitometry was carried out using the Image Lab software (Bio-Rad). Band intensities of NICD in each lane were normalized by band intensities of loading control β -actin in the corresponding lane.

Estimation of protein heights

Protein heights including extended Notch height was estimated by measuring the structural size of each domain (that is, EGF, NRR and SNAP) in Pymol (The PyMOL Molecular Graphics System, Version 2.0 Schrödinger, LLC.) and then creating an additive estimate based on the number of domains in the full-length Notch construct and each Notch truncation.

MD simulations

All MD simulations were conducted using the GROMACS package¹⁰³. Polarized MARTINI 2.2 parameters were used for the simulations¹⁰⁴. The system was composed of 54 PPCS, 54 DPPC, 108 DPPS, 288 DIPC, 216 cholesterol and 10,108 water molecules with a molar lipid composition of cholesterol:PPCS:DPPC:DIPC 3.0:1.5:1.5:4.0 in upper layer and cholesterol:DPPS:DIPC 3.0:3.0:4.0 in lower layer. To create immobilized lipids, we increased the mass of the phosphorus atom within DPPS by a factor of 1,000, keeping everything else the same in the parameter file. The pressure was set at 1.0 bar with a semi-isotropic Parrinello–Rahman coupling with compressibility 4.5×10^{-5} bar⁻¹ and the temperature was set to 295 K using Nosé–Hoover coupling. Each system was neutralized and brought to a concentration of 0.15 M with randomly placed sodium and chloride ions. We employed the LINCS algorithm to constrain to bond lengths¹⁰⁵. A time step of 20 fs

was used with an update of the neighbour list every ten steps, which are typical values employed in MARTINI simulations. Each simulation was run afterwards for 12 μ s, the last 3 μ s of which was used for analysis. The MD simulations were analysed using the in-built GROMACS tools. MDAnalysis libraries^{106,107} were used for calculating diffusion constant of lipid component, and `g_energy` was used for calculating inter-layer interaction.

Statistics and reproducibility

Statistical analysis was performed in GraphPad Prism 8.0 (GraphPad) or Microsoft Excel. Figure legends indicate all statistical tests used in the figure. Unless otherwise noted in the figure legends, statistical differences were determined using Student's *t*-test (two-tailed unpaired or paired *t*-test, depending on the experiment) when only two groups were compared or by ordinary one-way ANOVA followed by Tukey post-hoc test when multiple groups were analysed. The number of samples (*n*) used for each experimental analysis is indicated in the figure legends. Sample sizes of sufficient power were chosen on the basis of general standards accepted by the field and previous published studies in the field to enable statistical analyses and ensure reproducibility (for example, PMID: 27180907, 26051539, 29398116 and 30628888). No statistical method was used to pre-determine sample size. No data were excluded from the analyses. Data distribution was assumed to be normal, but this was not formally tested. Randomization was not necessary for this basic science study. All samples used in each set of experiments were equal, except the experimental condition being tested. All experiments were performed with appropriate control.

The number of independent experiments repeated for each representative result shown in extended data figures is provided here: for Extended Data Fig. 1a–c, *n* = 5 independent experiments; Extended Data Fig. 1d, *n* = 3 independent experiments; Extended Data Fig. 1e, *n* \geq 7 biologically independent cells; Extended Data Fig. 2a, *n* = 3 biologically independent samples; Extended Data Fig. 2b, *n* = 18 cells over two independent experiments; Extended Data Fig. 2c, *n* = 3 biological replicates; Extended Data Fig. 2h,i, *n* = 5 biological replicates; Extended Data Fig. 2k–n, *n* = 3 biological replicates; Extended Data Fig. 4c, *n* = 6 independent experiments; Extended Data Fig. 4e, *n* = 3 independent experiments; Extended Data Fig. 4f, *n* = 5 independent experiments; Extended Data Fig. 4h–j, *n* = 3 independent experiments; Extended Data Fig. 5g, *n* = 31 cells examined across two independent experiments; Extended Data Fig. 5l, *n* = 39 (+TAPI2, +DAPT) and *n* = 21 cells (+TAPI2, –DAPT) examined across three independent experiments; Extended Data Fig. 6a,b, *n* = 2 independent samples; Extended Data Fig. 6c, *n* = 33 (–DNA) and *n* = 29 (+DNA) cells over three independent experiments; Extended Data Fig. 6h, *n* = 2 independently synthesized samples; Extended Data Fig. 6i, *n* = 2 independent samples; Extended Data Fig. 6j, *n* = 4 independent experiments; Extended Data Fig. 6k, *n* = 6 independent experiments; Extended Data Fig. 7f,g, *n* = 3 independent experiments; Extended Data Fig. 8b, *n* = 3 (control) and *n* = 5 (DN Ecad) independent animals.

Reporting summary

Further information on research design is available in the Nature Portfolio Reporting Summary linked to this article.

Data availability

Previously published genomic sequence data that were re-analysed here are available from Ensembl for E-cadherin (CDH1) and N-cadherin (CDH2) protein from homo sapiens (gene IDs ENSG0000039068 and ENSG00000170558). Source data are provided with this paper. All raw images acquired using confocal, epifluorescence and time-lapse microscopy, and additional data that support the findings of this study are available from the corresponding authors upon reasonable request. All other data supporting the findings of this study are available from the corresponding author on reasonable request.

Code availability

Custom Python code used for automatic segmentation and junction intensity ratio analysis for Notch activation and truncation studies is available at <https://github.com/kmsouthard/JunctionAnalysis>. Co-localization analysis was carried out in ImageJ and the JACOP plugin available at <https://imagej.nih.gov/ij/plugins/track/jacop.html>. Custom ImageJ codes for other analyses, including quantification of Manders' overlap coefficients, Pearson's coefficients and lipid polarization analyses, are available at <https://github.com/sukgi333/yonsei-notch-activation>. Selected sgRNAs for the candidate target sites were evaluated with DeepSpCas9 sgRNA prediction tool (<http://deepcrispr.info/DeepSpCas9/>)⁹⁹.

References

- Pruessmeyer, J. et al. A disintegrin and metalloproteinase 17 (ADAM17) mediates inflammation-induced shedding of syndecan-1 and –4 by lung epithelial cells. *J. Biol. Chem.* **285**, 555–564 (2010).
- Kim, J. et al. Single-cell mechanogenetics using monovalent magnetoplasmonic nanoparticles. *Nat. Protoc.* **12**, 1871–1889 (2017).
- Dudok, B. et al. Cell-specific STORM super-resolution imaging reveals nanoscale organization of cannabinoid signaling. *Nat. Neurosci.* **18**, 75–86 (2014).
- Moss, M. L. & Rasmussen, F. H. Fluorescent substrates for the proteinases ADAM17, ADAM10, ADAM8, and ADAM12 useful for high-throughput inhibitor screening. *Anal. Biochem.* **366**, 144–148 (2007).
- Lee, H. J. et al. En bloc and segmental deletions of human XIST reveal X chromosome inactivation-involving RNA elements. *Nucleic Acids Res.* **47**, 3875–3887 (2019).
- Pulido-Quetglas, C. et al. Scalable design of paired CRISPR guide RNAs for genomic deletion. *PLoS Comput. Biol.* **13**, e1005341 (2017).
- Kim, H. K. et al. SpCas9 activity prediction by DeepSpCas9, a deep learning-based model with high generalization performance. *Sci. Adv.* **5**, eaax9249 (2019).
- Ramakrishna, S. et al. Gene disruption by cell-penetrating peptide-mediated delivery of Cas9 protein and guide RNA. *Genome Res.* **24**, 1020–1027 (2014).
- Gopalappa, R., Suresh, B., Ramakrishna, S. & Kim, H. Paired D10A Cas9 nickases are sometimes more efficient than individual nucleases for gene disruption. *Nucleic Acids Res.* **46**, e71 (2018).
- Guschin, D. Y. et al. A rapid and general assay for monitoring endogenous gene modification. *Methods Mol. Biol.* **649**, 247–256 (2010).
- van der Spoel, D. et al. GROMACS: fast, flexible, and free. *J. Comput. Chem.* **26**, 1701–1718 (2005).
- de Jong, D. H. et al. Improved parameters for the Martini coarse-grained protein force field. *J. Chem. Theory Comput.* **9**, 687–697 (2013).
- Hess, B., Bekker, H., Berendsen, H. J. C. & Fraaije, J. G. E. M. LINCS: a linear constraint solver for molecular simulations. *J. Comput. Chem.* **18**, 1463–1472 (1997).
- Michaud-Agrawal, N., Denning, E. J., Woolf, T. B. & Beckstein, O. MDAnalysis: a toolkit for the analysis of molecular dynamics simulations. *J. Comput. Chem.* **32**, 2319–2327 (2011).
- Chavent, M. et al. Methodologies for the analysis of instantaneous lipid diffusion in MD simulations of large membrane systems. *Faraday Discuss.* **169**, 455–475 (2014).

Acknowledgements

The authors thank S. Blacklow (Harvard U.), C. Miller (King's College London) and K. Shimamura (Kumamoto U.) for the kind gifts of Notch, APP and DN-cadherin plasmids, respectively. We also thank A. Balmain,

M. Moasser and E. Collison (UCSF) for sharing cell lines. D. Fletcher (UC Berkeley), A. Joffe (UC Berkeley) and D. Al-Rawi (Stanford U.) provided insightful discussion. For reagents, technical support, and discussions, we thank the Kim, Cheon, Gartner and Jun laboratories, as well as the Nikon Imaging Center and Wynton at UCSF. M.K. was supported by a Life Science Research Foundation fellowship as the Shurl and Kay Curci Foundation fellow, and by Burroughs Wellcome Travel Fund. This work was supported by NRF, NRF-2021R1F1A1063378 (M.K.), NRF-2018R1A5A1025511 (D.S.) and NRF-2017R1A2B3004198 (H.H.K.), HI17C0676 from Korean Ministry of Health and Welfare (H.H.K.), 5R01NS047229 from National Institute on Aging (NIA) and the National Institute of Health (NIH) (A.G.), 5R01AG008200 from National Institute on Aging (NIA) and the National Institute of Health (NIH) (N.K.R.), IBS-R026-D1 from IBS (M.K., H.H.K. and J.C.), NRF-2019R1A2C1085712 (Y.H.K.), the UCSF Center for Cellular Construction (an NSF Science and Technology Center, no. DBI-1548297) (Z.J.G.), U01CA244109 from the National Cancer Institute (Z.J.G.), 1R01GM112081, 1R01GM126542-01 and R35GM134948 from the National Institute of General Medical Science (NIGMS) and the NIH (Y.Jun), 1R21AG072232-01 from the National Institute on Aging (NIA) and the NIH (M.L.K. and Y.Jun), RO0CA226366 from the National Cancer Institute (M.L.K) and NIH, and the UCSF Program for Breakthrough Biomedical Research (PBBR) funded in part by the Sandler Foundation (M.L.K and Y.Jun). Z.J.G. is a Chan Zuckerberg BioHub Investigator.

Author contributions

M.K., K.M.S., Z.J.G. and Y.Jun conceived the ideas and designed research; M.K. and K.M.S. constructed plasmids, generated cell lines and performed confocal microscopy. M.K. performed mechanogenetics, truncation study, spatial mutation, immunoblot analysis, reporter cell assay and APP experiment. K.M.S. performed Notch exclusion and activation experiments, designed truncation study and wrote custom Python image analysis scripts. W.R.K. performed animal experiment, flotillin staining and mechanogenetic experiment. A.L. performed confocal imaging and lipid order imaging experiments. N.H.K. performed coarse-grained MD simulation. R.G. generated cadherin-KO cells. M.A. synthesized magnetic

nanoparticles. H.J.L., S.H.C. and K.N. helped with confocal imaging/western blot analysis. Y.Jung helped with lipid order imaging experiment. M.K.K. performed ELISA analysis of A β secretion from CDH-KO cells. S.H.C. performed western blot analysis. J.F. and D.S. performed initial proof-of-concept experiments. A.G. and N.K.R. provided anti-PS1 antibodies and critically read the manuscript. M.L.K. helped with the VE-cad experiment, H.H.K., Y.H.K. and J.C. oversaw CRISPR-Cas9 KO experiment, MD simulation and magnetic nanoparticle synthesis, respectively. Z.J.G. oversaw and supervised all spatial mapping and Notch truncation experiments. Y.Jun oversaw and supervised all aspects of the study. M.K. and K.M.S. analysed data. M.K., K.M.S., Z.J.G. and Y.Jun wrote the manuscript.

Competing interests

Z.J.G. is an equity holder in Scribe Biosciences and Provenance Bio and is an advisor for Serotiny. Y.H.K. is a vice president of, and has a financial interest in, Imnewrun. J.F. is a co-founder and a chief technology officer of, and has a financial interest in, Serotiny. The other authors declare no competing interests.

Additional information

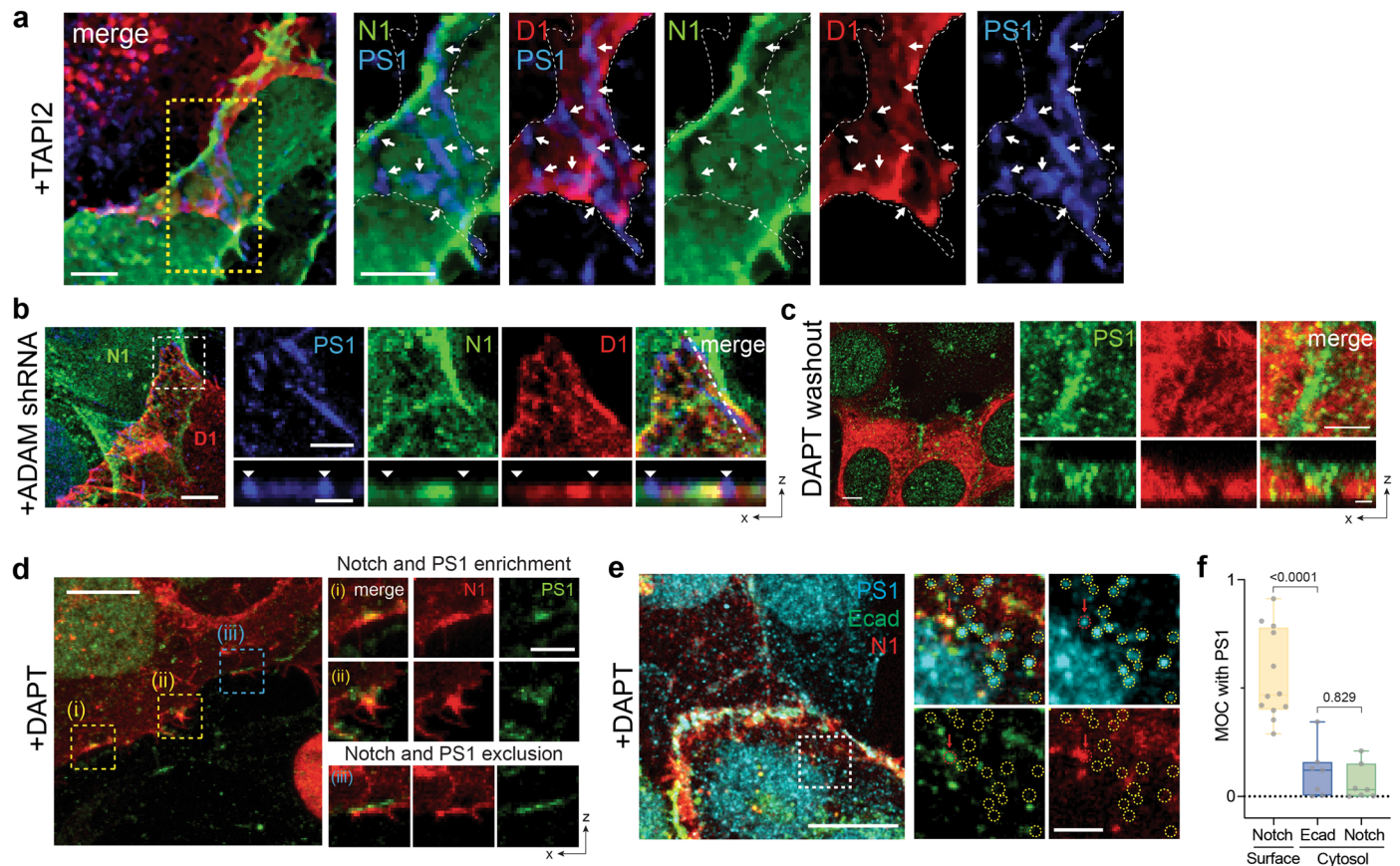
Extended data is available for this paper at <https://doi.org/10.1038/s41556-022-01031-6>.

Supplementary information The online version contains supplementary material available at <https://doi.org/10.1038/s41556-022-01031-6>.

Correspondence and requests for materials should be addressed to Zev J. Gartner or Young-wook Jun.

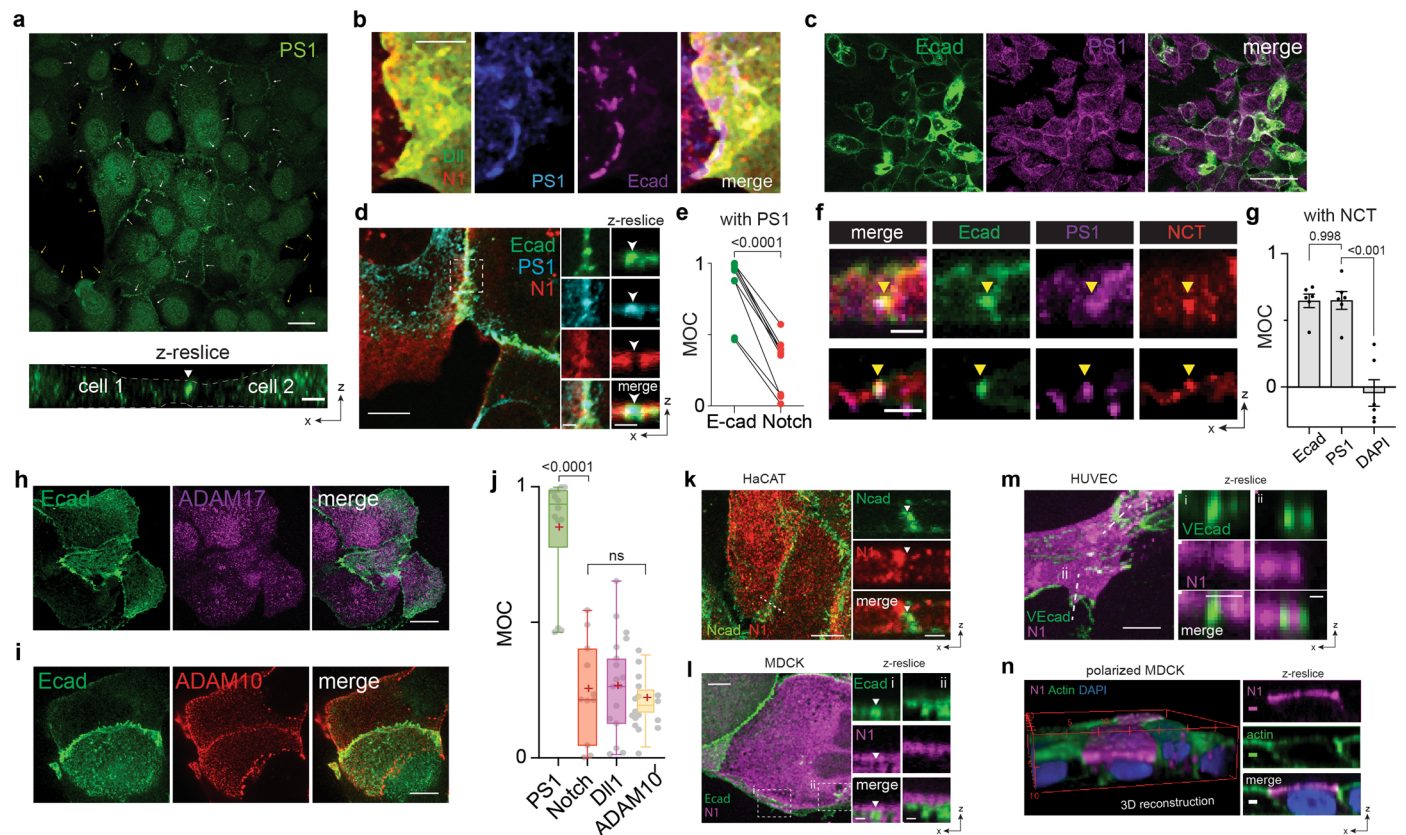
Peer review information *Nature Cell Biology* thanks Alf Honigmann, Alpha Yap and the other, anonymous, reviewer(s) for their contribution to the peer review of this work. Peer reviewer reports are available.

Reprints and permissions information is available at www.nature.com/reprints.



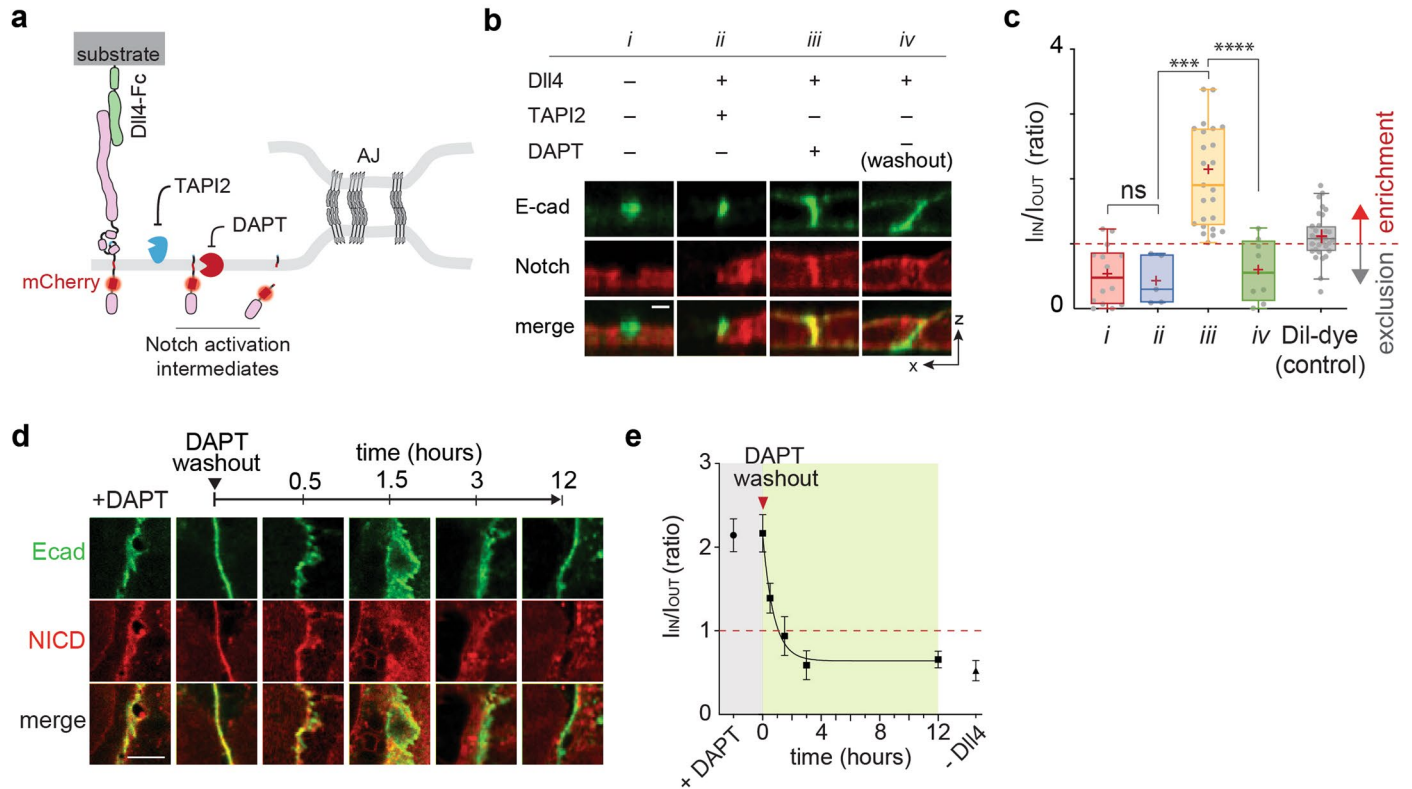
Extended Data Fig. 1 | Interfacial membrane compartmentalization choreographs the sequential molecular processing of Notch. (a) Representative confocal images showing Dll1 (D1), Notch1 (N1), or presenilin1 (PS1) distributions at the interfacial junction between two cells exclusively expressing D1 or N1 in the presence of TAPI2. (left) A maximum intensity projection image of a LRE μ domains. Scale bar, 5 μ m. (right) Magnified individual fluorescent channel and merged images of the yellow boxed region. The white dashed area and the white arrows indicate the cellular interface and the RIP μ domains, respectively. Scale bars, 3 μ m. (b) Representative confocal images showing the interfacial junction between two cells exclusively expressing N1 and D1 in the presence of ADAM10/17 shRNA. The cell on top labeled 'N1' expresses N1 only, while the bottom cell labeled 'D1' expresses D1 only. (left) A maximum intensity projection image of a LRE μ domains. Scale bar, 5 μ m. (top-right) Magnified individual fluorescence channel images of the boxed region. Scale bar, 3 μ m. (bottom-right) Z-resliced images showing the sections of the cellular interfaces. Scale bar, 2 μ m. (c) Representative confocal images showing N1, and PS1 distributions at the interfacial junction after washed out to remove TAPI2 and DAPT inhibition. With TAPI2 and siRNA treatment, Notch and γ -secretase compartmentalization was observed, while upon DAPT wash-out, Notch signals at the RIP μ domains disappeared. (left) A maximum intensity projection image of the cells showing enriched Notch mCherry signal at the RIP μ domains. Scale bar, 10 μ m. (Top-right) Magnified individual fluorescence channel images of the

boxed region. Scale bar, 2 μ m. (right) Z-resliced images showing the sections of the cellular interfaces. Scale bar, 2 μ m. (d) A representative confocal image showing Notch1 (N1) and presenilin1 (PS1) distribution at cellular interface. DAPT was added to inhibit S3 cleavage. (left) A maximum intensity projection image of a LRE μ domains. Scale bar, 10 μ m. (right) Magnified individual fluorescent channel and merged images of the boxed region. Scale bar, 3 μ m. (e) Representative confocal images showing intracellular distribution of PS1, E-cadherin (Ecad), and Notch1 (N1) in the presence of DAPT. (left) A maximum intensity projection image. Scale bar, 10 μ m. (right) Magnified individual fluorescent channel and merged images of the specified intracellular region (a white dashed box). The yellow dashed circles represent intracellular puncta enriched with PS1 with no Ecad or N1 signals. The red dashed circle indicated with the red arrow represents an intracellular punctum showing all PS1, Ecad, and N1 fluorescence signals. Scale bar, 2 μ m. (f) Manders' overlap coefficients (MOCs) for quantitative assessment of PS1 with Notch1 at cell surface, PS1 with Ecad at cytosol, and PS1 with Notch1 at cytosol, respectively. Each dot represents the MOC of a selected cell surface or cytosol. In the box-whisker plot, the boxes show the 25th to 75th percentiles, and the whiskers extend to the maxima and the minima. Solid lines indicate median, respectively. $n = 12$ (Notch1 at surface), 7 (Ecad in cytosol), and 7 (Notch1 in cytosol) biologically independent cells across 2 independent experiments; ordinary one-way ANOVA with Tukey's multiple comparison testing.



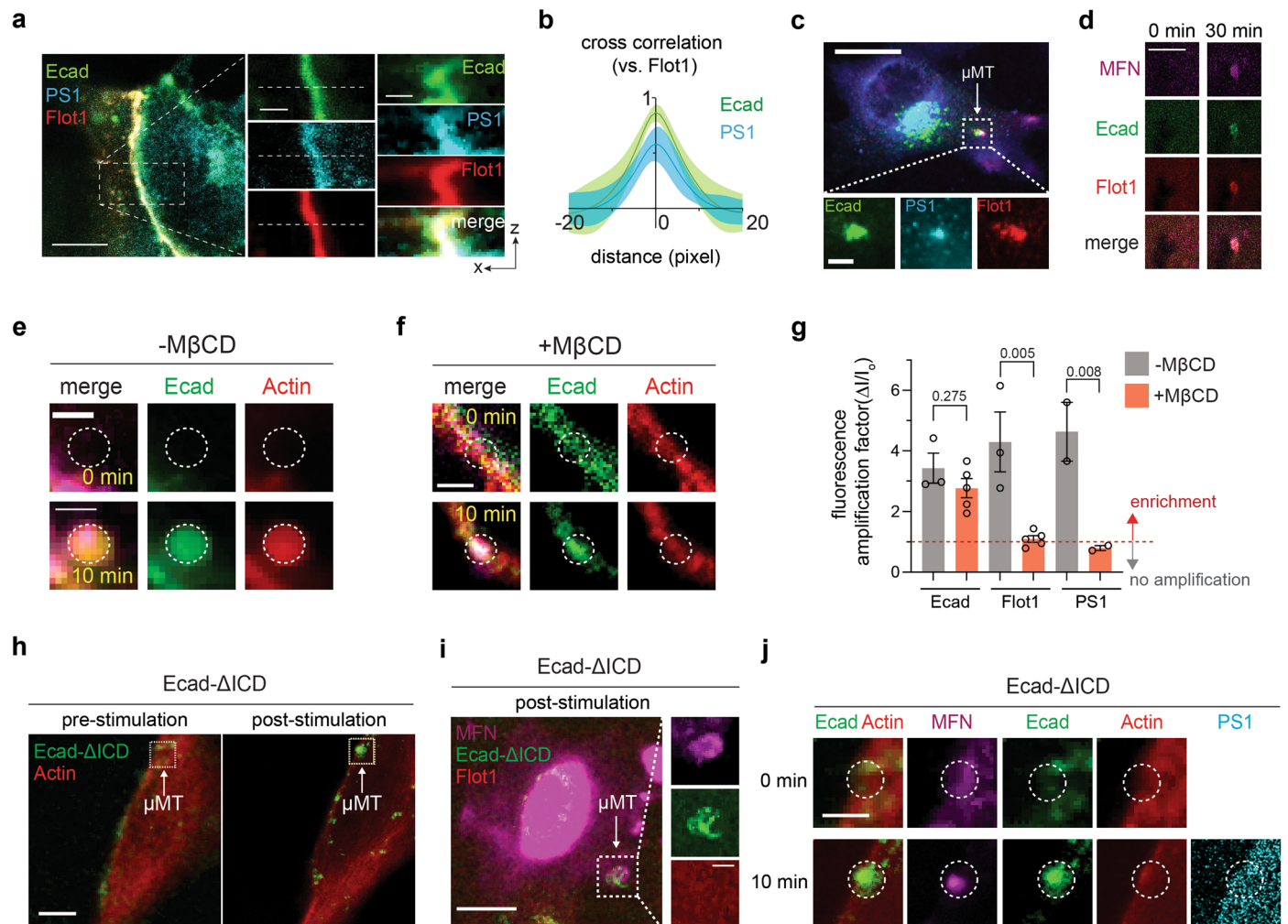
Extended Data Fig. 2 | Adherens junctions reorganize Notch signaling biomolecules into two distinct membrane microdomains (μ domains). **(a)** Representative confocal immunofluorescence images showing distribution of presenilin1 (PS1) across entire cell membranes. White and yellow arrows indicate the cell-cell interfacial membranes and the cell membranes without contact, respectively. (top) A maximum intensity projection of the wide-field confocal z-stacks. Scale bar, 20 μm . (bottom) A confocal z-resliced image along the representative membranes of two contacting cells. A white arrow indicates the cell-cell interfacial membrane where strong PS1 signals were observed. Yellow dashed lines represent the cell membranes without cell-cell contacts. Scale bar, 3 μm . **(b)** Maximum intensity projection images showing distribution of PS1 and E-cadherin AJs (Ecad) relative to LRE- μ domain with Notch1-Dll1 pair enrichment at the interfacial membrane in the presence of TAPI2. PS1 and Dll1 were visualized by immunostaining, Notch and AJs by expression of their respective mCherry- or EGFP-fusion constructs. AJs showed nearly identical spatial distribution with the γ -secretase enriched RIP- μ domain, but exhibited inverse distribution with the LRE- μ domain. Scale bar, 5 μm . **(c)** Representative wide-field confocal immunofluorescence images showing PS1 (magenta) enrichment within AJs (green). Scale bar, 50 μm (low-magnification), 10 μm (zoom-in). **(d)** Confocal images of U2OS cells co-expressing Ecad-GFP (green) and SNAP-N^{FL}-mCherry (red), and immunostained with PS1 antibody (cyan). Scale bars, 10 μm , 2 μm , and 2 μm for maximum intensity projection, zoomed-in, and z-resliced images, respectively. **(e)** Paired analysis of Manders' overlap coefficients of E-cadherin and Notch signals over PS1 in multiple cells ($n = 9$ examined across

3 independent experiments). Two-tailed paired Student's *t* test. **(f)** Confocal z-resliced images showing PS1 (magenta) and Nicastrin (NCT, red) distribution relative to cadAJs (green). Scale bar, 2 μm . **(g)** Analysis of Manders' overlap coefficients (MOC) of E-cadherin, PS1, and DAPI over Nicastrin in multiple cells ($n = 6$ examined across 2 independent experiments). One-way ordinary ANOVA followed by Tukey's multiple comparison testing. **(h, i)** Representative confocal immunofluorescence images showing **(h)** ADAM17 and **(i)** ADAM10 distribution relative to AJs. ADAM17 exhibited no preferential localization relative to AJs. Scale bar, 20 μm . **(j)** Box-whisker plots showing Manders' overlap coefficients (MOCs) of PS1 (green), Notch (red), Dll1 (purple), and ADAM10 (yellow) relative to AJs. Each dot represents the MOC of a selected AJ. Boxes and whiskers denote the inner-quartile and full ranges. Colored lines and (+) marks indicate median and mean, respectively ($n = 15$ (Dll1), 11 (Notch1), 14 (PS1), and 19 (ADAM10) cells examined over two independent experiments; ns, not significant; ordinary one-way ANOVA with Tukey's test). **(k)** Representative confocal fluorescence images of HaCaT cells immunostained with anti-Notch1 (red) and anti-N-cadherin (green). **(l)** Confocal images of MDCK cells expressing Ecad-GFP (green) and SNAP-N^{FL}-mCherry. Notch receptors were labeled with BG-Alexafluor647 (magenta). **(m)** Confocal images of HUVECs expressing SNAP-N^{FL}-mCherry and immunostained with vascular endothelial cadherin (VE-cad) antibody. **(l-m)** Scale bar, 10 μm and 2 μm for maximum intensity projection and z-resliced images, respectively. **(n)** Polarized MDCK cells grown on a transwell filter. Notch, actin, and nucleus were immunostained with BG-AF647, phalloidin-488, and DAPI, respectively. Scale marked every 5 μm for 3D construction. Scale bar, 2 μm .



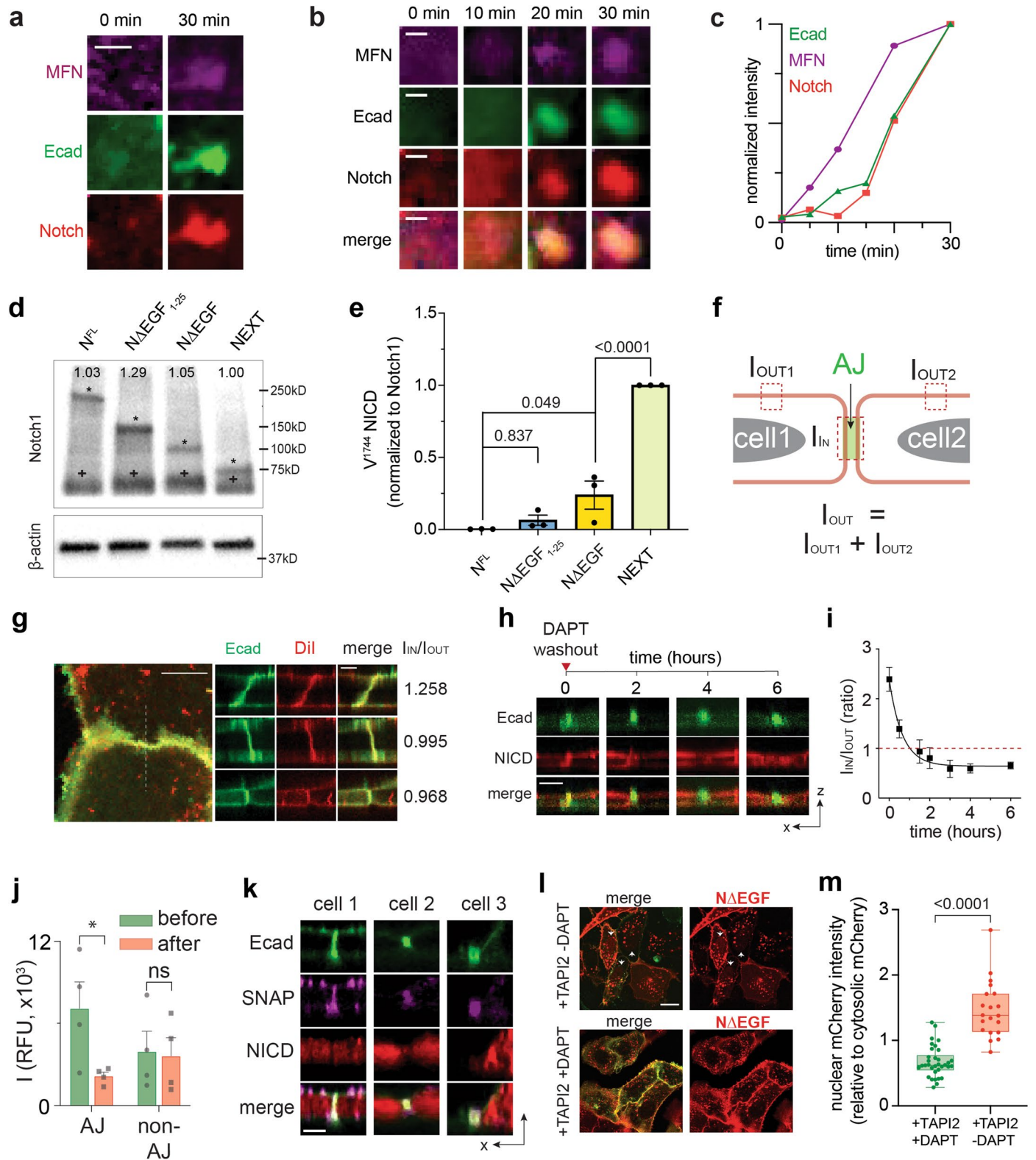
Extended Data Fig. 3 | Spatial dynamics of Notch receptors relative to AJs during cell-surface activation. (a) A schematic to capture the spatial distribution of Notch intermediates during the cell-surface activation pathway. (b) Confocal z-resliced images showing Notch distribution (red) relative to AJ (green) from the cells without DII4 activation (i), treated with DII4 and TAPI2 (ii), treated with DII4 and DAPT (iii), and washed out to remove DAPT inhibition (iv). Scale bar, 3 μ m. (c) Quantification of Notch signal enrichment at the AJs during the activation. Notch enrichment (I_{IN}/I_{OUT}) is calculated as the ratio of average Notch fluorescence intensity within AJs (I_{IN}) and outside AJ (I_{OUT}). The enrichment factor of Dil is present as a control showing AJ-independent distribution. In the box-whisker plot, the boxes show the 25th to 75th percentiles, and the whiskers extend to the 10th and 90th percentiles, with individual data points above the

whiskers shown for the lowest and highest 10% of each dataset. Solid lines and (+) marks indicate median and mean, respectively. $n =$ (left to right) 13, 4, 25, 17 cells analyzed across three independent experiments. *** $P = 0.0005$, **** $P < 0.0001$, ns: non-significant, one-way ordinary ANOVA followed by Tukey's multiple comparison testing. (d) Representative time-course confocal z-resliced images showing S2-cleaved Notch at AJs as a function of time after DAPT removal. The NICD signal (red) at the AJ gradually decreases, indicating NICD release. Images shown here are not from identical cells, but represent a general trend of NICD signal at AJs for each time point. Scale bar, 5 μ m (e) Quantification I_{IN}/I_{OUT} ratio as a function of time after DAPT washout. Data are the mean \pm s.d of $n = 25$ (+DAPT), 9 (0 hr), 10 (0.5 hr), 6 (1.5 hr), 8 (3 hr), 17 (12 hr), and 14 (-DII4) biological replicates examined across 3 independent experiments.



Extended Data Fig. 4 | Interrogation of the mechanism underlying γ -secretase recruitment into AJs. (a) Representative confocal fluorescence images showing the PS1 and Flot1 distribution relative to native cell-cell AJs. (left) A maximum intensity projection image of merged channels. Scale bar, 10 μ m. (center) Magnified images showing greater details of the boxed region. Scale bar, 2 μ m. (right) Z-resliced images showing the sections of the AJs. Scale bar, 2 μ m. Line profiles of fluorescence signals from E-cadherin, PS1, and Flot1 along the white dashed lines in the z-resliced images. (b) Cross-correlation analysis of E-cadherin and PS1 over Flot1. Both Flot1 and PS1 fluorescence intensities exhibited strong positive correlation with the AJ. The solid curves and the shades indicate means and s.e.m., respectively. $n = 7$. (c) Confocal fluorescence images showing PS1 and Flot1 localization at artificial AJs by mechanogenetics. E-cadherin and Flot1 were labeled with fluorescent tags. Endogenous PS1 was immunostained after fixation. Scale bar, 20 μ m. (d) Magnified confocal images showing PS1 and Flot1 localization before (0 min) and after (30 min) the formation of artificial AJs via mechanogenetics. Scale bar, 20 μ m. (e) Magnified confocal images showing strong accumulation of Actin at the artificial AJ by

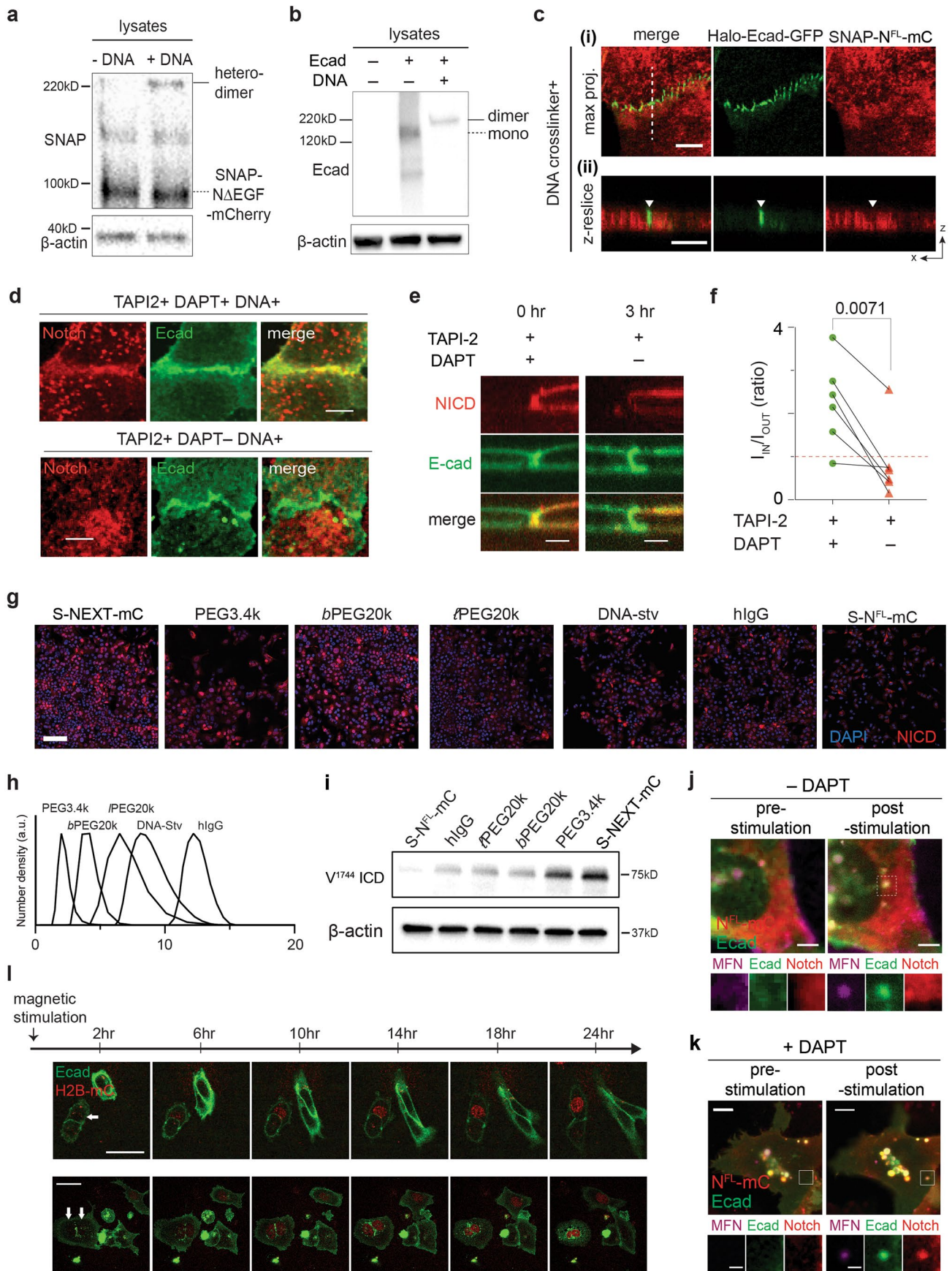
mechanogenetics. Scale bar, 5 μ m. (f) Representative confocal fluorescence images showing no enrichment of Actin signal at the artificial AJs during M β CD treatment. Scale bar, 5 μ m. (g) Fluorescence amplification factors (I/I_0) of E-cadherin, Flot1, and PS1 localization in response to the mechanogenetic formation of AJs quantified for multiple replicates. The effect of M β CD treatment on Flot1 and PS1 relocalization was assessed. Data are the mean \pm s.e.m. of $n = 3$ (Ecad, -M β CD), 5 (Ecad, +M β CD), 3 (Flot1, -M β CD), 5 (Flot1, +M β CD), 2 (PS1, -M β CD), and 2 (PS1, +M β CD) biologically independent mechanogenetic experiments. One-way analysis of variance (ANOVA) with Tukey's multiple comparisons test. (h) Representative fluorescence image showing the mechanogenetic formation of Ecad- Δ ICD cluster. A white dashed box indicates the subcellular region where the μ MT was applied. Scale bar, 10 μ m. (i) Confocal image showing that the mechanogenetically induced Ecad- Δ ICD clusters did not recruit Flot1. Scale bar, 20 μ m. Zoom-in of the white frame-marked region of μ MT application is shown on the right. Scale bar, 5 μ m. (j) Spatial distribution of F-actin and PS1 in response to Ecad- Δ ICD clustering. Neither F-actin nor PS1 were localized at the cluster region. Scale bar, 5 μ m.



Extended Data Fig. 5 | See next page for caption.

Extended Data Fig. 5 | AJ-induced membrane juxtaposition drives Notch exclusion via size-dependent protein segregation. **(a)** Additional artificial AJs showing Notch recruitment. Scale bar, 2 μm . **(b)** Time-lapse epifluorescence images (were acquired before micromagnetic tweezer (μMT) stimulation and then at 10, 20, 30 minutes of the μMT application. Gradual MFN and E-cadherin clustering was clearly seen, followed by Notch accumulation at the AJ. Scale bar, 2 μm . **(c)** Kinetics of signal enrichments at the artificial AJ shown in the panel (b). This is a representative result from $n = 3$ artificial AJs from 3 independent experiments. **(d)** Representative western blot for total Notch ICD from the U2OS cells stably expressing Notch1 truncation variants. The blot was probed with anti-Notch1-ICD. The same lysates were used in (Fig. 3F). The asterisk (*, upper band) represent the intact Notch truncation variants. Expected molecular weight of N^{E1} , $\text{N}\Delta\text{EGF1-25}$, $\text{N}\Delta\text{EGF}$, and NEXT are 250 kD, 150 kD, 110 kD, and 95 kD, respectively. The cross (+, lower) represents the reduced protein band of 70 kD. All variants contain the SDS/DTT-sensitive link that produces the protein band corresponding to the polypeptide of Notch ECD and transmembrane-intracellular domain (TMICD). The number shown in each lane indicates the quantified band intensity of the corresponding lane normalized to that of NEXT variant. The intensity is calculated by summing the intensities measured from two bands detected in each lane. **(e)** Western blot quantification of cleaved NICD levels over total Notch levels. Data are the mean \pm s.e.m. of $n = 3$ experiments. One-way analysis of variance (ANOVA) with Tukey's multiple comparisons test. **(f)** Method to quantify Notch enrichment. Please see methods for more details. **(g)** Representative confocal images and enrichment factors ($I_{\text{IN}}/I_{\text{OUT}}$) of Dil membrane staining dye distribution relative to AJs. Scale bars, 10 μm (maximum

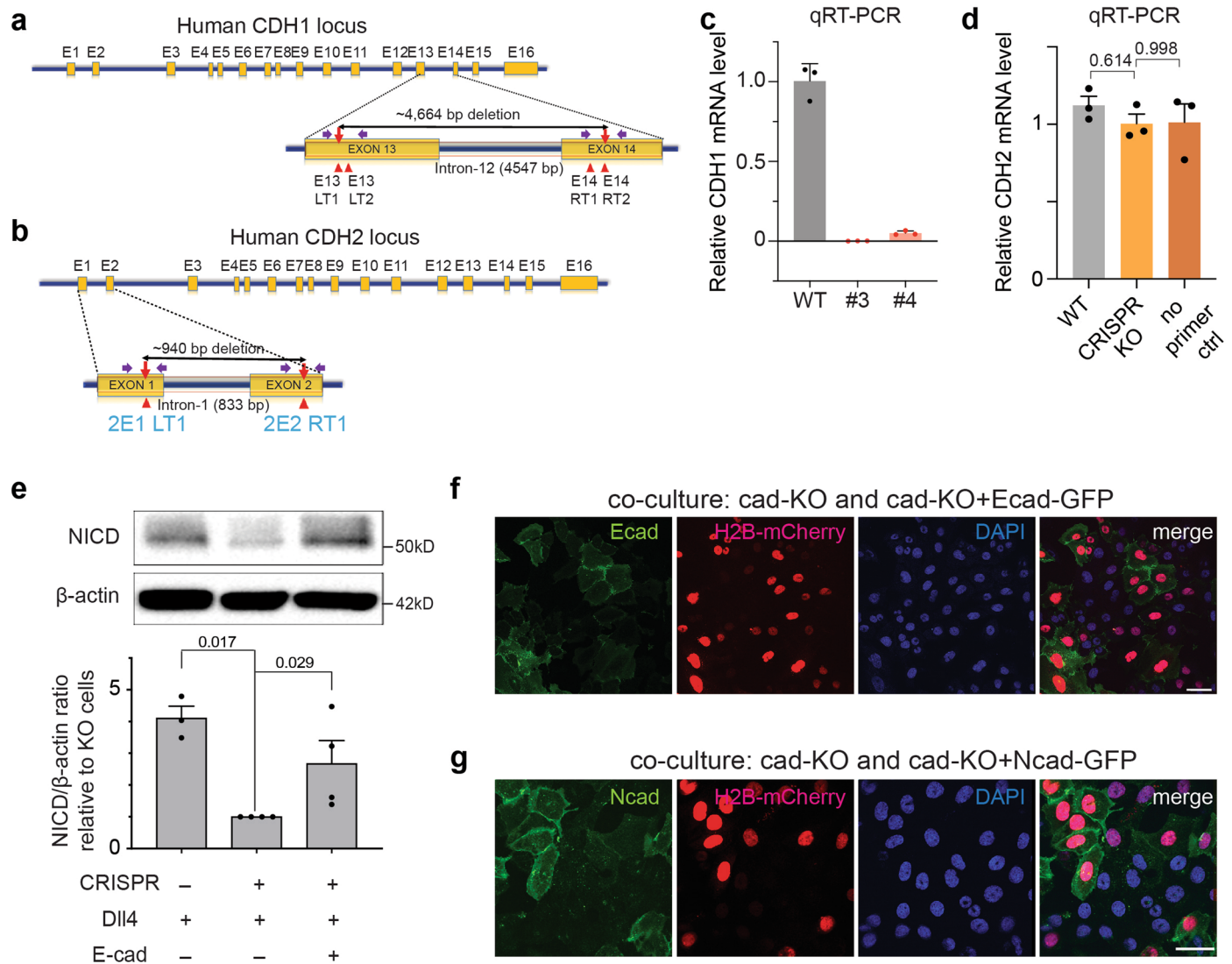
intensity projection), 3 μm (z-resliced images). **(h)** Time series of confocal z-resliced images showing the enrichment of $\text{N}\Delta\text{EGF}$ (red) at the AJ (green) under DAPT treatment ($t = 0$), and the dissipation during DAPT washout ($t \geq 2$). Scale bar, 3 μm . **(i)** Single-cell traces showing the time-course of the decline of $\text{N}\Delta\text{EGF}$ enrichment factor at the AJs during DAPT washout (mean \pm s.e.m.; $n = 4$ independent single-cell experiments). **(j)** Quantification of changes in NICD signal from these four cells at the AJs and non-AJ membrane, at $t = 0$ (green, before washout) and $t = 6$ hr (red, after DAPT washout). AJs and non-AJ membrane were detected based on thresholding and automatic segmentation using the custom-built script. Intracellular-mCherry signal significantly decreased at the AJs, but not at non-AJ membranes (* $P = 0.035$, ns: $P = 0.075$, Student's t and Wilcoxon test, $n = 4$ cells examined across 2 independent experiments). **(k)** Confocal z-resliced images showing the distribution of extracellular SNAP (purple) and intracellular mCherry (red) tags of $\text{N}\Delta\text{EGF}$ relative to AJs (green) after DAPT removal. Scale bar, 3 μm . **(l, m)** Nuclear location of NICD released from cell membrane that recombinantly expresses $\text{N}\Delta\text{EGF}$. **(l)** Confocal fluorescence images of U2OS cells expressing SNAP- $\text{N}\Delta\text{EGF}$ -mCherry and Ecad-GFP. (Upper) Cells treated with TAPI2 only. White arrowheads indicate the cells with nuclear NICD-mCherry accumulation. (Lower) Cells treated with both TAPI2 and DAPT. Scale bar, 20 μm . **(m)** Quantification of the ratio of nucleus-to-cytosolic mCherry signals in cells with DAPT ($n = 39$ AJs) and those without DAPT ($n = 21$ AJs) from 3 independent experiments. A box and a whisker indicate the interquartile and the full range, respectively. Colored lines indicate median. Two tailed unpaired Student's t -test.



Extended Data Fig. 6 | See next page for caption.

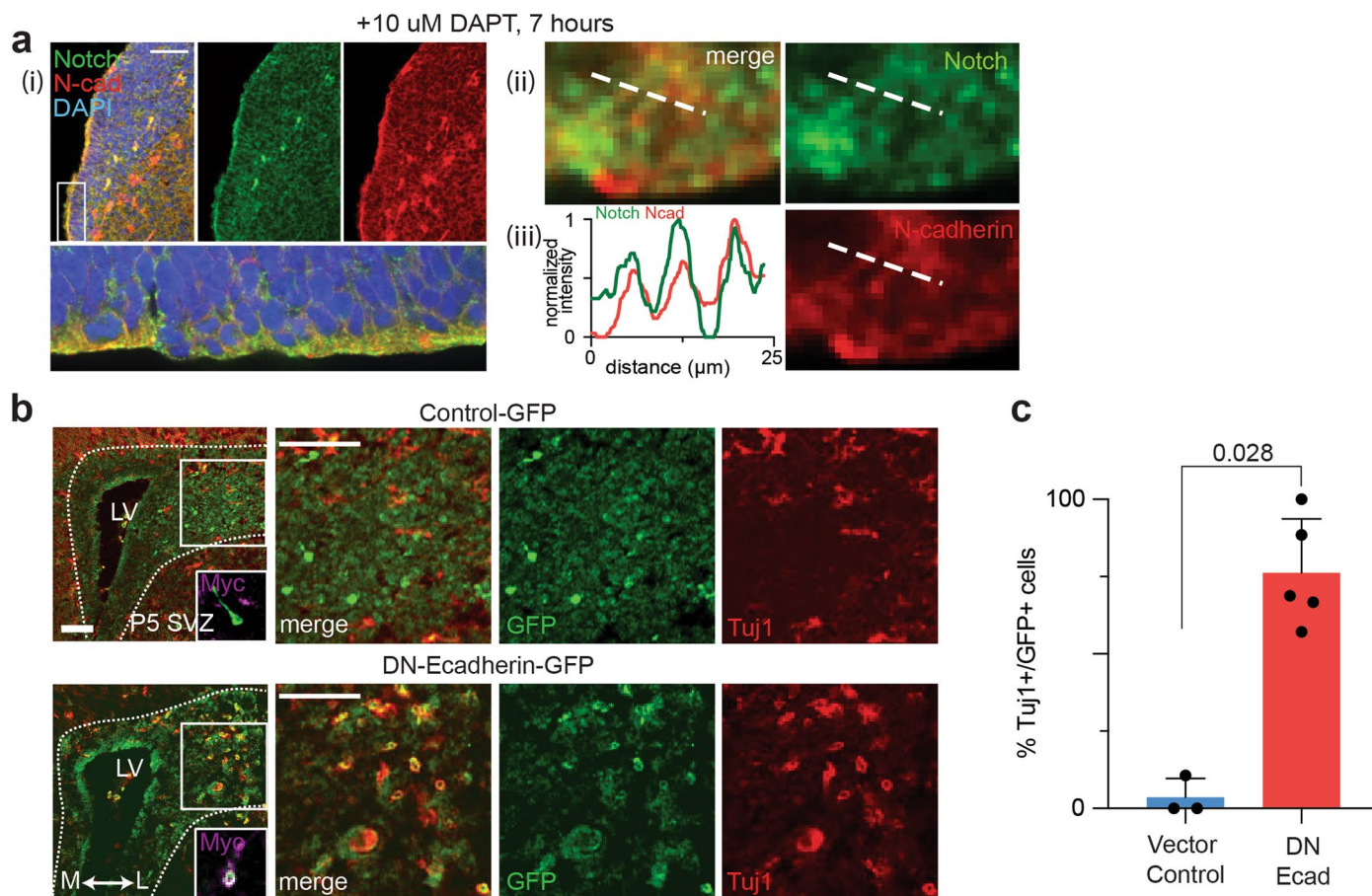
Extended Data Fig. 6 | Spatial mutations of Notch to study the effect of membrane compartmentalization on the signaling. A representative western blot of lysate from cells expressing NΔEGF and Halo-Ecad-GFP after 2 hr incubation with or without DNA crosslinkers. The blot was labelled with anti-SNAP (a) and anti-Ecadherin (b) antibodies. The expected mass of NΔEGF, E-cadherin monomer, and the complex with the Notch construct and E-cadherin forming a heterodimer are 90 kD, 158 kD, and 230 kD, respectively. β-actin detection was used to assess protein loading. In both blots, predicted bands representing Notch-E-cadherin heterodimers (solid black lines) and SNAP-NΔEGF-mCherry or Halo-Ecad-GFP monomers (dashed black lines) are indicated. (c) A representative maximum intensity projection of XY images (i) and a XZ-resliced image (ii) showing exclusion of full-length Notch1 (SNAP-N^{FL}-mCherry) from the AJs (green) after the DNA crosslinking. (d) Representative confocal maximum intensity projection images showing the distribution of NΔEGF relative to the AJs after crosslinking. Cells were treated with or without DAPT. Scale bar, 10 μm. (e) Single-cell confocal z-resliced images showing intracellular mCherry signal at the AJ under DNA and DAPT treatment (left) and after washing out DAPT (right). Removing DAPT elicited a significant reduction in mCherry signal intensity from the AJ. Scale bar, 5 μm. (f) Paired analysis of multiple cells expressing NΔEGF in enrichment factor (I_{IN}/I_{OUT}) after DAPT washout. Each dot represents I_{IN}/I_{OUT} value before and after DAPT washout from a single cell. Each

line corresponds to the I_{IN}/I_{OUT} changes before and after DAPT washout in a same single cell (paired two-tailed Student's t test; n = 6 cells examined across 2 independent experiments). (g) Larger area (1 × 1 mm²) confocal fluorescence images shown in Fig. 4f. Scale bar, 200 μm. (h) Dynamic light scattering spectra of BG-modified macromolecules used in the experiment to induce spatial mutation of NEXT in Fig. 4d-g. (i) Western blot analyses showing that spatial mutations of NEXT alter the level of Notch activation. Representative western blot from three independent experiments. The blot was probed with specific antibodies for cleaved NICD (Val¹⁷⁴⁴) and β-actin. Each lane was loaded with the lysates from NEXT-expressing cells incubated with different BG-modified polymers or proteins for 20 h. The lysate from N^{FL} was used as control. (j,k) Representative images of artificial AJs formed in live cells. Cells treated with both TAPI2 and DAPT (j) or with only TAPI2 but no DAPT (k). Magnified images were shown in lower panels. An intense mCherry signal was observed at the artificial AJ with TAPI2 and DAPT treatment, while no enrichment of Notch1 signal was seen from cells without DAPT. Scale bar, 5 μm (low-magnification), 2 μm (zoomed-in images). (l) Representative time-lapse images showing Notch signal activation in UAS-Gal4 reporter cells with artificial AJs (white arrows). Cells were cultured in the presence of TAPI2 and no source of S2 cleavage. Neighboring cells without magnetic stimulation were used as internal negative controls. Images were acquired using epifluorescence imaging every 2 hr for 24 hr. Scale bar, 50 μm.



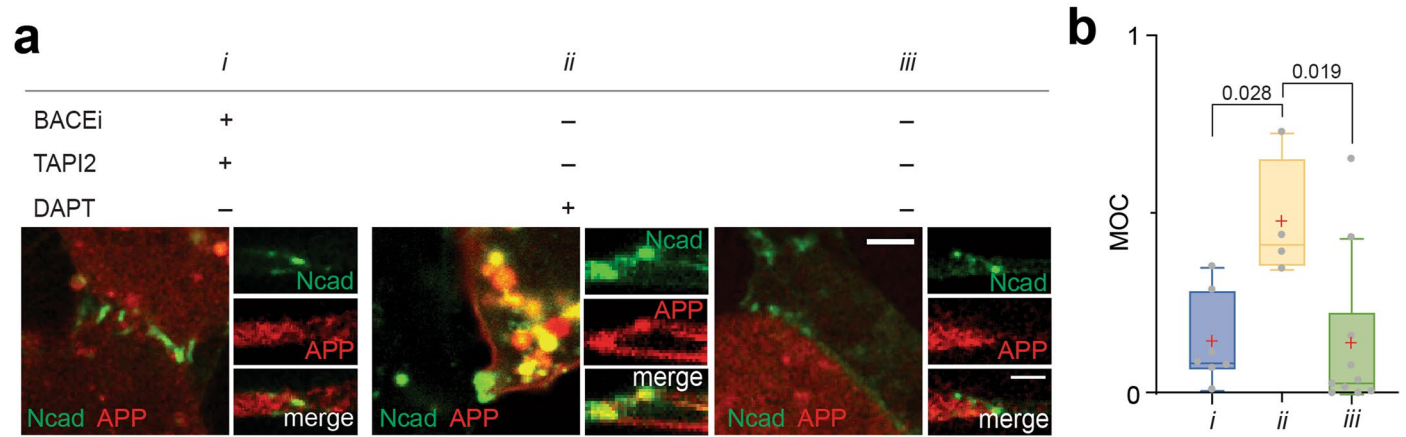
Extended Data Fig. 7 | Generation of U2OS SNAP-N^{FL}-Gal4 fluorescence reporter cell lines lacking E-cadherin via CRISPR/Cas9. (a,b) Schematic representation of human CDH1 (a) and CDH2 (b) gene structure and targeted segmental deletion sites. The sixteen exons are shown in orange boxes (E1-E16). Red arrowheads indicate the sgRNA-binding sites (E13LT1, E13LT2, E14RT1 and E14RT2 for CDH1, 2E1LT1 and 2E2RT1 for CDH2). The targeted segmental deletions of 4.6 kb for CDH1 and 940 bp for CDH2 knockout are shown with a black line with red arrow tips, respectively. Purple arrows represent PCR primers used for the T7E1 assay and detection of alleles with targeted deletions, respectively. (c) CDH1 mRNA expression levels in CDH1 KO clone #3 and #4 were determined using qRT-PCR. CDH1 expression levels in the selected clones containing a segmental deletion were quantified relative to CDH1 mRNA levels of the wild-type U2OS SNAP-N^{FL}-Gal4 cells. Clone #3 was used for subsequent experiments. Data are the mean \pm s.d. of $n = 3$ biologically independent samples. (d) qRT-PCR analysis of CDH2 mRNA expression levels in U2OS SNAP-N^{FL}-Gal4 reporter cells (WT), CDH1 KO clone #3 (Ecad-KO), and a negative control sample

(no primer pair added). CDH2 mRNA levels in both WT and Ecad-KO cells were quantified relative to the negative control sample. Both WT and Ecad-KO cells showed negligible CDH2 mRNA levels, indicating that Ecad-KO cells have minimal mRNA expression of both CDH1 and CDH2. Data are the mean \pm s.e.m. of $n = 3$ biologically independent samples; one-way ordinary ANOVA test. (e) Western blot analyses of cleaved NICD levels in the wild-type SNAP-N^{FL}-Gal4 cells, CDH1 knock-out (Ecad-KO) cells, and Ecad-KO cells with recombinant E-cadherin transfection. (top) A representative image of immunoblotting. (bottom) Quantification of cleaved NICD levels. The average intensity of NICD bands relative to β -actin bands was quantified and then normalized to that of Ecad-KO cells. Data are the mean \pm s.d. of $n = 5$ biological replicates; one-way ANOVA followed by Tukey's test. (f,g) Representative epi-fluorescence images showing Notch activation in co-culture of Ecad-KO cells with Ecad-KO + Ecad cells (f) or with Ecad-KO + Ncad cells (g). Ecad-KO cells show no GFP signal (green) while Ecad-KO + Ecad or Ecad-KO + Ncad cells show robust GFP signal indicative of reintroduction of E- or N-cadherin. Scale bar, 50 μ m.



Extended Data Fig. 8 | Additional immunofluorescence images showing that the AJ-mediated membrane compartmentalization modulates neural progenitor cell (NPC) differentiation. (a) Immunostaining of the subventricular zone (SVZ) in the lateral ventricle (LV) of the E13.5 DAPT-treated mouse brain. Notch was colocalized at NAJ, visualized by immunostaining with anti-N-cadherin and anti-Notch1 antibodies. (i) Representative lower magnification image. The indicated area (a white box) is magnified and rotated 90° clockwise in the lower panel. Scale bar, 100 μ m. (ii) Magnified view of the region indicated with a white dashed box in the (i) lower panel. Scale bar, 2.5 μ m. (iii) Line profiles of N-cadherin and Notch distributions. (b) Additional confocal

images of coronal sections of developing mouse brain retrovirally infected with dominant negative form of E-cadherin vector (DN-Ecad-EGFP). Transduced cells differentiated into post-mitotic neurons can be identified as EGFP⁺/Tuj1⁺, while those remained as NPCs with plasmid transfection are only EGFP⁺. (left) Low-magnification images. Insets show the magnified image of a representative single cell immunostained for myc-tag. (right) Magnified view of the boxed region. Scale bar, 50 μ m. (c) Ratio of GFP/Tuj1-double positive cells to total Tuj1-positive post-mitotic neurons in these two conditions. Data are the mean \pm s.e.m. of $n = 3$ (vector control) and 5 (DN-Ecad-EGFP) biologically independent animals. Two-tailed unpaired Student's t test.



Extended Data Fig. 9 | Amyloid precursor proteins (APPs) with intact YENPTY motif show size-dependent spatial segregation and membrane proteolysis, consistent with APP lacking the YENPTY motif. (a) Representative confocal maximum intensity projection (right) and z-resliced (left) images of U2OS cells co-expressing N-cadherin (green) and full-length APP (red). To capture the spatial distribution of the APP intermediates, cells were cultured with a combination of α -, β -, and γ -secretase inhibitors. Scale bar, 3 μ m (max. projection) and

2 μ m (z-resliced). **(b)** The spatial redistribution of APP relative to the NAJs was quantified using Manders' overlap coefficient (MOC). Data are presented as boxes and whiskers, representing interquartile and min-to-max ranges, respectively; $n = 7$ (i), 4 (ii), and 10 (iii) NAJs examined over two independent experiments, each detected from a single cell. One-way ANOVA followed by Tukey's multiple comparison test.

Reporting Summary

Nature Research wishes to improve the reproducibility of the work that we publish. This form provides structure for consistency and transparency in reporting. For further information on Nature Research policies, see our [Editorial Policies](#) and the [Editorial Policy Checklist](#).

Statistics

For all statistical analyses, confirm that the following items are present in the figure legend, table legend, main text, or Methods section.

- | | |
|-------------------------------------|--|
| n/a | Confirmed |
| <input type="checkbox"/> | <input checked="" type="checkbox"/> The exact sample size (n) for each experimental group/condition, given as a discrete number and unit of measurement |
| <input type="checkbox"/> | <input checked="" type="checkbox"/> A statement on whether measurements were taken from distinct samples or whether the same sample was measured repeatedly |
| <input type="checkbox"/> | <input checked="" type="checkbox"/> The statistical test(s) used AND whether they are one- or two-sided
<i>Only common tests should be described solely by name; describe more complex techniques in the Methods section.</i> |
| <input type="checkbox"/> | <input checked="" type="checkbox"/> A description of all covariates tested |
| <input type="checkbox"/> | <input checked="" type="checkbox"/> A description of any assumptions or corrections, such as tests of normality and adjustment for multiple comparisons |
| <input type="checkbox"/> | <input checked="" type="checkbox"/> A full description of the statistical parameters including central tendency (e.g. means) or other basic estimates (e.g. regression coefficient) AND variation (e.g. standard deviation) or associated estimates of uncertainty (e.g. confidence intervals) |
| <input type="checkbox"/> | <input checked="" type="checkbox"/> For null hypothesis testing, the test statistic (e.g. F , t , r) with confidence intervals, effect sizes, degrees of freedom and P value noted
<i>Give P values as exact values whenever suitable.</i> |
| <input checked="" type="checkbox"/> | <input type="checkbox"/> For Bayesian analysis, information on the choice of priors and Markov chain Monte Carlo settings |
| <input checked="" type="checkbox"/> | <input type="checkbox"/> For hierarchical and complex designs, identification of the appropriate level for tests and full reporting of outcomes |
| <input type="checkbox"/> | <input checked="" type="checkbox"/> Estimates of effect sizes (e.g. Cohen's d , Pearson's r), indicating how they were calculated |

Our web collection on [statistics for biologists](#) contains articles on many of the points above.

Software and code

Policy information about [availability of computer code](#)

- | | |
|-----------------|---|
| Data collection | Software for the control of the wide-field epifluorescence microscopy is micro-manager 1.4. Software for the image acquisition using confocal fluorescence microscopy are Nikon NIS Element AR (Advanced Research) and Zeiss Zen system (Blue for LSM9 confocal microscopy). Software for the acquisition and analysis of western blot assays is Image Lab software (Bio-Rad, ver 6.1.0), Software for the acquisition and analysis of RT-PCR is Applied Biosystems StepOnePlus Real-Time PCR system. The code for co-localization analysis is available online at https://github.com/kmsouthard/JunctionAnalysis |
| Data analysis | Software for image processing and analyses is ImageJ2 (ver 2.3.0) and Fiji (https://imagej.net/software/fiji/). Data analysis and statistical testing were performed using GraphPad Prism 9 (ver 9.3.1), Image Lab software (Bio-Rad, ver 6.1.0), and Microsoft Excel (for MAC, ver 16.59). The software used for molecular dynamics simulations is the GROMACS packages and MDAnalysis libraries. A description of the code used for MD simulations is provided in the Methods section. The python codes used for segmentation, thresholding, and junction intensity calculation has been deposited at Github (https://github.com/kmsouthard/JunctionAnalysis). A description of the code is provided in the online methods. All original ImageJ macros and codes used for image post-processing and colocalization analysis have been deposited and available at Github (https://github.com/sukgi333/yonsei-notch-activation). |

For manuscripts utilizing custom algorithms or software that are central to the research but not yet described in published literature, software must be made available to editors and reviewers. We strongly encourage code deposition in a community repository (e.g. GitHub). See the Nature Research [guidelines for submitting code & software](#) for further information.

Data

Policy information about [availability of data](#)

All manuscripts must include a [data availability statement](#). This statement should provide the following information, where applicable:

- Accession codes, unique identifiers, or web links for publicly available datasets
- A list of figures that have associated raw data
- A description of any restrictions on data availability

Previously published genomic sequence data that were re-analysed here are available from Ensembl for E-cadherin (CDH1) and N-cadherin (CDH2) protein from homo sapiens (gene ID: ENSG0000039068 and ENSG00000170558). Source data are provided with this study. All statistical source data have been provided as Source Data. All raw unprocessed gel images have been provided as Source Data. All raw images acquired using confocal, epifluorescence, and time-lapse microscopy, and additional data that support the findings of this study are available from the corresponding authors upon reasonable request. All other data supporting the findings of this study are available from the corresponding author on reasonable request.

Field-specific reporting

Please select the one below that is the best fit for your research. If you are not sure, read the appropriate sections before making your selection.

- Life sciences Behavioural & social sciences Ecological, evolutionary & environmental sciences

For a reference copy of the document with all sections, see [nature.com/documents/nr-reporting-summary-flat.pdf](https://www.nature.com/documents/nr-reporting-summary-flat.pdf)

Life sciences study design

All studies must disclose on these points even when the disclosure is negative.

Sample size	No statistical method was used to predetermine sample size. Sample sizes was chosen on the basis of previous published studies in the field to enable statistical analyses and ensure reproducibility (e.g. PMID: 27180907, 26051539, 29398116, 30628888)
Data exclusions	No data were excluded from this study.
Replication	To ensure reproducibility, all experiments were repeated at least two times with independent biological replicates and deemed valid in both rendered similar results. To ensure reproducibility, all mechanogenetic experiments were repeated at least three times with independent biological replicates. All repeated experiments were successful and yielded similar results. All statistical analysis were based on at least three replicates.
Randomization	Randomization was not necessary for this basic science study. All samples used in each set of experiments were equal, except the experimental condition being tested. All experiments were performed with appropriate control.
Blinding	Investigators were not blinded during data collection and analysis. Blinding was not possible since the main researcher was responsible for both data acquisition and analysis.

Reporting for specific materials, systems and methods

We require information from authors about some types of materials, experimental systems and methods used in many studies. Here, indicate whether each material, system or method listed is relevant to your study. If you are not sure if a list item applies to your research, read the appropriate section before selecting a response.

Materials & experimental systems

n/a	Involved in the study
<input type="checkbox"/>	<input checked="" type="checkbox"/> Antibodies
<input type="checkbox"/>	<input checked="" type="checkbox"/> Eukaryotic cell lines
<input checked="" type="checkbox"/>	<input type="checkbox"/> Palaeontology and archaeology
<input type="checkbox"/>	<input checked="" type="checkbox"/> Animals and other organisms
<input checked="" type="checkbox"/>	<input type="checkbox"/> Human research participants
<input checked="" type="checkbox"/>	<input type="checkbox"/> Clinical data
<input checked="" type="checkbox"/>	<input type="checkbox"/> Dual use research of concern

Methods

n/a	Involved in the study
<input checked="" type="checkbox"/>	<input type="checkbox"/> ChIP-seq
<input checked="" type="checkbox"/>	<input type="checkbox"/> Flow cytometry
<input checked="" type="checkbox"/>	<input type="checkbox"/> MRI-based neuroimaging

Antibodies

Antibodies used	All antibodies are listed in Methods under "Immunofluorescence staining" and "Western Blot analysis" with species, company/catalog#, clone, dilution used per application, and published references, if applicable.
-----------------	---

The following primary antibodies were used:

mouse monoclonal anti-ADAM10 (Santa Cruz Biotechnology, sc-28358, Clone # B-3, 1:100 for IF)
 mouse monoclonal anti-ADAM17 (R&D Systems, MAB9301, Clone # 111633, 1:200 for IF)
 rabbit polyclonal anti-Presenilin-1 (Nikolaos Robakis, 1:50 for IF)
 rabbit monoclonal anti-nicastrin (Cell Signaling Technology, D4F6N, Clone #30239, 1:200 for IF)
 mouse polyclonal anti-Paxillin (BD Bioscience, 610051, 1:500 for IF)
 mouse monoclonal anti-VE-cadherin (BD Bioscience, 610251, Clone 75, 1:400 for IF)
 mouse monoclonal anti-E-cadherin (Santa Cruz Biotechnology, sc-8426, Clone G-10, 1:100 for WB)
 mouse polyclonal anti-mCherry (Abcam, 167453, 1:500 for WB)
 Alexa Fluor 488 Phalloidin (Invitrogen, A12379, 1:40 of 200 units/mL stock for IF)
 rabbit monoclonal anti-cleaved Notch1 (1744) (Cell Signaling Technology, 4147S, Clone D3B8, 1:1000 for WB)
 rabbit polyclonal anti-SNAP-tag (New England Biolab, P9310S, 1:1000 for WB)
 rabbit monoclonal anti-Notch1 (Cell Signaling Technology, 4380S, Clone D6F11, 1:1000 for WB)
 rabbit monoclonal anti- β -Actin (Cell Signaling Technology, 4970S, Clone 13E5, 1:10000 for WB)

The following secondary antibodies were used:

Alexa Fluor 405 Goat anti-rabbit IgG (H+L) cross-adsorbed antibody (Invitrogen, A31556, 1:400 for IF)
 Alexa Fluor 488 Goat anti-mouse IgG (H+L) cross-adsorbed antibody (Invitrogen, A32723, 1:400 for IF)
 Alexa Fluor 568 Goat anti-mouse IgG (H+L) cross-adsorbed antibody (Invitrogen, A11004, 1:400 for IF)
 Alexa Fluor 647 Goat anti-mouse IgG (H+L) cross-adsorbed antibody (Invitrogen, A32728, 1:500 for IF)
 Alexa Fluor 647 Goat anti-rabbit IgG (H+L) cross-adsorbed antibody (Invitrogen, A27040, 1:500 for IF)
 Anti-rabbit IgG, HRP-linked antibody (Cell Signaling Technology, 7074S, 1:2000 - 1:10000 for WB)

Validation

All antibodies used in this study were commercially available and validated by the manufacturers (links below), except rabbit polyclonal anti-Presenilin-1, which was validated in previous literatures (Kouchi et al. J Biol Chem (2009), doi: 10.1074/jbc.M806250200, Georgakopoulos et al. Mol Cell (1999), doi: 10.1016/s1097-2765(00)80219-1). All antibodies used were further validated using routine experimental procedures by detecting proteins at the expected sizes in SDS-PAGE gels or detecting immunofluorescence of positive and negative control samples, confirming specific binding to the target proteins. Additionally, our use of RNAi and signaling inhibitors further validated some antibodies.

mouse monoclonal anti-ADAM10 (Santa Cruz Biotechnology, sc-28358, Clone # B-3, 1:100 for IF)
 Validation Refs. from the manufacturer's datasheet: <https://datasheets.scbt.com/sc-28358.pdf>

mouse monoclonal anti-ADAM17 (R&D Systems, MAB9301, Clone # 111633, 1:200 for IF)

Validation Refs. from the manufacturer's datasheet: https://www.rndsystems.com/products/human-tace-adam17-ectodomain-antibody-111633_mab9301

rabbit polyclonal anti-Presenilin-1 (Nikolaos Robakis, 1:50 for IF)

rabbit monoclonal anti-nicastrin (Cell Signaling Technology, D4F6N, Clone #30239, 1:200 for IF)

Validation Refs. from the manufacturer's datasheet: <https://www.cellsignal.com/datasheet.jsp?productId=30239&images=1&size=A4>

mouse polyclonal anti-Paxillin (BD Bioscience, 610051, 1:500 for IF)

Validation Refs. from the manufacturer's datasheet: <https://www.bdbiosciences.com/content/bdb/paths/generate-tds-document.au.610051.pdf>

mouse monoclonal anti-VE-cadherin (BD Bioscience, 610251, Clone 75, 1:400 for IF)

Validation Refs. from the manufacturer's datasheet: <https://www.bdbiosciences.com/content/bdb/paths/generate-tds-document.kr.610251.pdf>

mouse monoclonal anti-E-cadherin (Santa Cruz Biotechnology, sc-8426, Clone G-10, 1:100 for WB)

Validated by over-expression and knock-out in this study.

Validation Refs. from the manufacturer's datasheet: <https://datasheets.scbt.com/sc-8426.pdf>

mouse polyclonal anti-mCherry (Abcam, 167453, 1:500 for WB)

Validated by over-expression in this study

Validation Refs. from the manufacturer's datasheet: <https://www.abcam.com/mcherry-antibody-ab167453.html>

Alexa Fluor 488 Phalloidin (Invitrogen, A12379, 1:40 of 200 units/mL stock for IF)

Validation Refs. from the manufacturer's datasheet: <https://www.thermofisher.com/order/catalog/product/A12379>

rabbit monoclonal anti-cleaved Notch1 (1744) (Cell Signaling Technology, 4147S, Clone D3B8, 1:1000 for WB)

Validated by over-expression of Notch variants and Notch inhibition in this study.

Validation Refs. from the manufacturer's datasheet: <https://www.cellsignal.com/datasheet.jsp?productId=4147&images=1&size=A4>

rabbit polyclonal anti-SNAP-tag (New England Biolab, P9310S, 1:1000 for WB)

Validated by overexpression experiments of SNAP-Notch variants in this study

Validation Refs. from the manufacturer's datasheet: <https://international.neb.com/products/p9310-anti-snap-tag-antibody-polyclonal#Product%20Information>

rabbit monoclonal anti-Notch1 (Cell Signaling Technology, 4380S, Clone D6F11, 1:1000 for WB) Validated by overexpression and knock-down experiments in this study

Validation Refs. from the manufacturer's datasheet: <https://www.cellsignal.com/products/primary-antibodies/notch1-d6f11-xp-rabbit-mab/4380>

rabbit monoclonal anti- β -Actin (Cell Signaling Technology, 4970S, Clone 13E5, 1:10000 for WB)

Eukaryotic cell lines

Policy information about [cell lines](#)

Cell line source(s)	The cell lines used are described in Supplementary Table 1 and the materials and methods under "Tissue culture" as follows: Human bone osteosarcoma epithelial (U2OS) cells were purchased from ATCC (ATCC HTB-96). Human Flp-In T-Rex U2OS cells were established as previously described (Malecki et al., Molecular and Cellular Biology, 2006) and were gifts from S. Blacklow (Harvard University). Human umbilical vein (HUVEC) cells were purchased from ATCC (ATCC PCS-100-013). Madin Darby Canine Kidney (MDCK) cells were purchased from UCSF's Cell and Genome Engineering Core (CCLZR291). Human primary epidermal keratinocytes (HECAT) cells were purchased from ATCC (ATCC PCS-200-011).
Authentication	All cell lines were authenticated based on their morphology, growth condition, and immunostaining with specific markers. The Plain U2OS and Flp-In T-Rex U2OS cell lines were previously authenticated in Seo et al. Cell (2016) and Kim et al. Nature Protocols (2017) based on their morphology and proliferation rate (for Plain U2OS) and immunofluorescence staining as well as immunoblotting against SNAP-Notch variants to confirm the function of the Flp-In T-Rex system (for Flp-In T-Rex U2OS).
Mycoplasma contamination	All cell lines were tested with Mycoalert mycoplasma detection kit (Lonza), and no mycoplasma contamination was found.
Commonly misidentified lines (See ICLAC register)	No commonly misidentified cell lines were used.

Animals and other organisms

Policy information about [studies involving animals](#); [ARRIVE guidelines](#) recommended for reporting animal research

Laboratory animals	We used CD-1 embryonic day 13.5 (E13.5) and postnatal day three (P3) newly born mice for in vivo experiments. P3 pups (4 males, 4 females) were obtained by purchased of an untimed pregnant female mouse (E13-15) from Charles River Laboratories (Wilmington, MA) and waited for birth. All mice were bred and maintained under specific-pathogen-free conditions individually ventilated cages. All animals were placed under a 12hr light-dark cycle and maintained at 22 °C ± 1 °C with 30-70% humidity. None of the mice were involved in any previous procedures before the study.
Wild animals	No wild animals were used in the study.
Field-collected samples	No field-collected samples were used in the study.
Ethics oversight	Experiments were approved by the University of California San Francisco Institutional Animal Care and Use Committee (IACUC, AN180609-02B).

Note that full information on the approval of the study protocol must also be provided in the manuscript.